

**Chemical reactions controlled through
compartmentalization:
Applications to bottom-up design of synthetic life**

Dissertation

zur Erlangung des akademischen Grades

Doctor rerum naturalium

vorgelegt

der Fakultät Physik

Bereich Mathematik und Naturwissenschaften
der Technischen Universität Dresden

von

Sudarshana Laha

geboren am 11.08.1994 in Kolkata, Indien



Technische Universität Dresden
Max-Planck-Institut für Physik komplexer Systeme
Zentrum für Systembiologie Dresden

Dresden, 2023

Betreuer:

Prof. Dr. Frank Jülicher

Prof. Dr. Christoph A. Weber

Gutachter:

Prof. Dr. Frank Jülicher (co-signed by Prof. Dr. Benjamin Friedrich)

Prof. Dr. Christoph A. Weber

Dedicated

to my loving grandparents and parents
for their steadfast support for me

to the memory of Prof. Amit Dutta
*we remember you warmly for being the Polaris in our lives
helping us navigate our ways to find fulfillment in success
we will forever strive to be your worthy students*

Every soul that touches yours -
Be it the slightest contact -
Get there from some good;
Some little grace; one kindly thought;
One aspiration yet unfelt;
One bit of courage
For the darkening sky;
One gleam of faith
To brave the thickening ills of life;
One glimpse of brighter skies -
To make this life worthwhile
And heaven a surer heritage.
-Making Life Worthwhile, George Eliot

ABSTRACT

Liquid-liquid phase separation (LLPS) has been proposed as the underlying physical principle leading to the formation of membrane-less organelles in eukaryotic cells, following advancements, in the last two decades, in experimental observations owing to progress in confocal microscopy. These organelles can act as compartments in sequestering molecules and tuning rates of biochemical reactions, among a repertoire of functions they serve. Biochemical reactions are constantly in progress in living cells and are driven out of equilibrium due to fuel consumption in the form of ATP or GTP molecules. Free diffusion of reactive molecules through these compartments leads to their spatiotemporal sequestration and automatically implies an interplay between phase separation and chemical reactions. In this work, we are specifically interested to understand how the two processes closely affect each other and applying the understanding to tune better bottom-up design principles for synthetic life, which involves coupling compartmentalization and chemical reactions.

The first part of this work is devoted to studying the interplay between phase separation and chemical reactions. To this end, we developed the theory of mass action kinetics of equilibrium and out-of-equilibrium processes occurring at phase equilibrium in a multi-component mixture. Phase equilibrium is imposed at all times, thus restricting the chemical kinetics to the binodal manifold. We learn more about circumstances in which reaction rates can differ in coexisting phases. Next, we decouple the phase-forming components (scaffolds) and the dilute reactive components (clients), which means that the reactive dilute components respond to the heterogeneous profile in the system set by the scaffold but do not affect it. This allows us to investigate to what extent compartments can affect chemical reactions in terms of their yield at steady state for a bimolecular reaction or initial reaction rate for a nucleation process compared to the absence of compartments. We use the effective droplet model and mass reaction kinetics at phase equilibrium to address the above questions. We can understand better how the properties of reactions can be optimally tuned by compartment size.

Following the theoretical developments in the first part of this work, we proceed to use the theoretical model of mass action kinetics at phase equilibrium to study emergent properties of parasitic behavior in a system composed of multiple fuel-driven reaction cycles, which lead to the formation of so-called "building blocks" which can phase separate. This study also helps us probe the buffering capacity of phase separation. It further provides

insights into how the lifetime of reactive "building blocks" can be tuned via phase separation.

Synthetic cells are generally realized by localizing minimalistic reactions in micron-scale water-filled environments, thus mimicking compartmentalization. Here we apply our model to understand how the localization of an autocatalytic process (PEN-DNA reaction) inside proteinosomes affect the reaction rates compared to the reactions in a homogeneous buffer solution.

To summarize, we developed theoretical approaches to study the interplay of chemical reactions with compartmentalization and apply such approaches to systems chemistry and synthetic biology experimental studies to unravel how reactions can be controlled through compartmentalization.

ACKNOWLEDGEMENTS

I wish to express my sincere gratitude to my supervisors Christoph A. Weber and Frank Jülicher. Christoph has been an unwavering support for me with his reservoir of enthusiasm and commitment to discussing science (from the nitty gritty technical details to the philosophy of a research problem). He has taught and allowed me to be creative in my scientific approaches. Frank has always pushed me to think beyond the apparent result of a problem with his constructive feedback during seminars. That has taught me, besides scientific rigor, a persistence to navigate the crevices of the research problems I have addressed in this dissertation. A special mention to Simon Alberti for his invaluable feedback during the thesis advisory committee meetings.

I have been truly fortunate to be surrounded by brilliant colleagues, which have led to some lifelong friendships during my stay at the PKS. The list is sorted in causal order of getting acquainted with them: Omar (my first Deutsch teacher), Joris (Bohemian Rhapsody sing-along partner), Giacomo (provider of melodies), Jacqueline (a fellow human behavioral studies analyst), Lars (my baking instructor), Martin (my coffee partner), Rao (my ping-pong opponent), Jonathan (one of the best book recommender), Xueping (a patient listener of my woes), Aida (my travel partner) and Kafa (my emergency snacks supplier at the institute). I would also thank (in no particular order) Argo, Adolfo, Charlie, Stefano, Tyler, Felix, Christian, Matteo, Patrick, Boyi, Ahan, Kathrin, Tarun, Suganthan, Kartik, and Ali for gifting me some memorable moments at the institute.

I have had the opportunity to collaborate with some exceptional scientists over the last few years: Patrick Schwarz and Job Boekhoven (TUM), Mengfei Gao, Archisman Ghosh, and Dora Tang (MPICBG). I am thankful to them for sharing their specialized research data and for lucid scientific exchanges during meetings. A special mention to Thomas Michaels (ETH Zürich) for being so forthcoming during our scientific sessions. I would also like to thank all my group members in Augsburg for the great discussions during group meetings and for being gracious hosts during my visits to Augsburg.

I sincerely appreciate all the help I received in the institute from Ulrike, Hubert, Thomas, Rita, Elise, Christina, and members of the visitors' program. That a thriving environment is offered at the institute for researchers is their credit.

Lastly, I would proudly mention my parents, Souren and Srabani. They are my biggest cheerleaders, my most trusted confidants, and my source of willpower. I would wish for their happiness and good health.

Contents

1	Introduction	1
1.1	Phase Separation - A brief overview of the development of the field	1
1.2	Thermodynamics of phase separation in a multi-component mixture	4
1.2.1	Mean field free energy	4
1.2.2	Other possible free energy considerations: Beyond mean-field	7
1.2.3	Exchange chemical potential, chemical activity and osmotic pressure	8
1.2.4	Thermodynamic instability leads to phase separation	9
1.2.5	Phase equilibrium conditions	10
1.2.6	Relaxation dynamics to phase equilibrium	13
1.3	Thermodynamics of chemical reactions in homogeneous mixtures	14
1.3.1	Chemical equilibrium conditions	14
1.3.2	Relaxation to chemical equilibrium	16
1.4	Thermodynamic equilibrium	17
1.5	Scope of the thesis	19
2	Chemical reaction kinetics at phase equilibrium	21
2.1	Kinetics of chemical reactions relaxing to thermodynamic equilibrium	21
2.1.1	Volume fraction field and phase volume kinetics	22
2.1.2	Diffusive exchange rates between phases	22
2.1.3	Reaction rates at phase equilibrium	23
2.1.4	Properties of chemical reactions at phase equilibrium	24
2.2	Unimolecular chemical reactions in coexisting phases	25
2.3	Bimolecular chemical reactions in coexisting phases	27
2.4	Chemical reactions maintained away from chemical equilibrium	28
2.4.1	Tie-line selecting curve	31
2.5	Summary and Discussion	32
3	Chemical reactions of dilute clients in phase-separated compartments	33

3.1	Thermodynamics of a multicomponent mixture of scaffold and clients	34
3.1.1	Phase equilibrium conditions: Dilute client limit	35
3.1.2	Relaxation dynamics to phase equilibrium: Dilute client limit	38
3.1.3	Chemical equilibrium conditions: Dilute client limit	40
3.1.4	Relaxation dynamics to chemical equilibrium: Dilute client limit	41
3.2	Applications	42
3.2.1	Two-state transitions controlled by a drop	43
3.2.2	Bimolecular reaction controlled by a drop	45
3.2.3	Nucleation reaction controlled by a drop	47
3.3	Summary	49
4	Fuel-driven chemical reactions in the dilute phase at phase equilibrium	50
4.1	Chemical reaction network and its properties	51
4.1.1	Observations from individual reaction cycles	52
4.1.2	Observations from combined reaction cycles	53
4.2	Kinetic equations at phase equilibrium	55
4.3	Construction of the ternary phase diagram	57
4.4	Mechanism of co-phase separation	58
4.4.1	Composition of droplets	60
4.5	Co-phase separation with periodic fueling	61
4.6	Effects of activation rate constants on host-parasite identity	63
4.7	Summary	64
5	Study of enzymatic kinetics in compartmentalized systems	65
5.1	Autocatalytic reactions and their properties	66
5.2	PEN DNA mass action kinetics	67
5.3	Proteinosomes affect the PEN DNA reactions	70
5.4	Summary	71
6	Conclusion and Outlook	72
A	Free energy calculations for block charged polymers using RPA	76
B	Numerical Methods	79
C	Linear first order corrections to scaffold equilibrium volume fractions	83

D	Dynamic equations in dilute limit	86
E	Spatial solutions	88
F	Fitting routine and extracted rate coefficients	90
G	Experimental methods	95
H	Calibration constants and reaction rate coefficients of PEN DNA study	98
	List of figures	101
	References	106

Chapter 1

Introduction

"Wonder is the heaviest element on the periodic table. Even a tiny fleck of it stops time."

– Diane Ackerman, *The Rarest of the Rare*

1.1 Phase Separation - A brief overview of the development of the field

Phase separation is essentially the creation of distinct phases from a single homogeneous mixture. It has been well studied in the context of colloidal chemistry and polymer physics. In colloidal chemistry, W.B. Hardy and E.B. Wilson were among the pioneers, back at the end of the 19th century, who proposed the cytoplasm (then referred to as 'protoplasm') as a colloid [1, 2]. W.B. Hardy further linked the formation of biological colloids with phase separation in his study of globulins, stating that: *"The globulin is dispersed in the solvent as particles which are the colloid particles and which are so large as to form an internal phase"*, and additionally attributed to the basic physical description of oil-water phase separation. Around the same time, the French biologist, Stephane Leduc, wrote in his book "The Mechanism of Life (1911) [3]": *"The liquids are the most important constituents of a living organism since they are the seat of all the chemical and physical phenomena of life. The junction of two liquids of different concentration is the arena in which takes place both the chemical transformation of matter and the correlative transformation of energy."*

Meanwhile, in polymer physics, strides were made by M.L. Huggins and P.J. Flory to study the thermodynamics of polymer solutions taking into account the dissimilarity in the molecular sizes using a lattice model [4, 5, 6]. The concepts underlying the physics of phase separation were strongly established, and later P.G. de Gennes was awarded the Nobel prize in 1991 *"for discovering that methods developed for studying order phenomena in simple systems can be generalized to more complex forms of matter, in particular to liquid crystals and polymers"*. His article in Nature highlighted that despite displaying similar phase separation attributes, polymers should be distinguished from other types of colloids [7]. This has been reflected in the reduced usage of the term colloid to describe the higher-order association behavior of biopolymers in modern cell biology and molecular self-assembly. In other disciplines, around the 1970s, scientists had developed the colloidal phase separation model for milk casein micelles [8]. In the following decades, the phase-separation behavior of gamma-crystallin proteins from lens epithelial cells and cataracts

in solution [9] was identified, followed by the characterization of phase separation of starch granules from the cytoplasm of plant cells [10].

Recent advancements and open questions

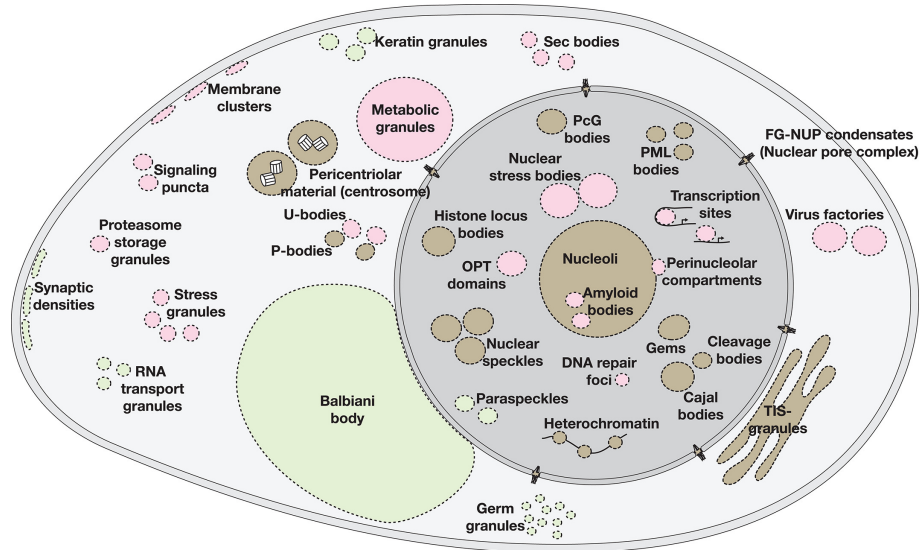


Fig. 1.1: Illustrative examples of biomolecular condensates in eukaryotic cells. These condensates are ubiquitous (brown hues), cell-type specific (green hues), or condition-dependent (red hues). Source [11]

At the end of the 20th century, breakthroughs made in confocal microscopy led to the identification of various proteins, RNA, and carbohydrates clustering inside the cell cytoplasm and nucleus to form membrane-less compartments (Fig. 1.1), which were then referred to by a plethora of names, some being "punctas", "granules", "assemblies", "aggregates" and "paraspeckles". The need to revisit the concepts of phase separation was strongly felt and was thus reborrowed from colloidal chemistry, and polymer physics [12]. Since 2009, multiple studies have provided further evidence of the existence of such compartments formed via intracellular phase separation of biomacromolecules [13, 14, 15]. One of the most prominent studies was the observation of localizing germline P granules in *C. elegans* germ cells which exhibited all liquid-like attributes, viz., fusion, dripping, and wetting [13]. Besides *in vivo* studies, several reconstituted *in vitro* studies [16, 17, 18] strengthened the evidence.

These compartments are also referred to as biomolecular condensates [19], which can be misleading given condensation in physics solely refers to liquid-gas phase transition. However, the analogy holds due to the process of undergoing self-assembly, thus locally leading to an increase in the concentration of assembling components. Once the existence of membrane-less compartments was established, the immediate questions that arose among many were the functional purpose they serve. They are incredibly complex compartments with hundreds to thousands of identified components per condensate [20, 21]. Therefore it is natural that they mediate diverse tasks, and some of the functions stem from their abil-

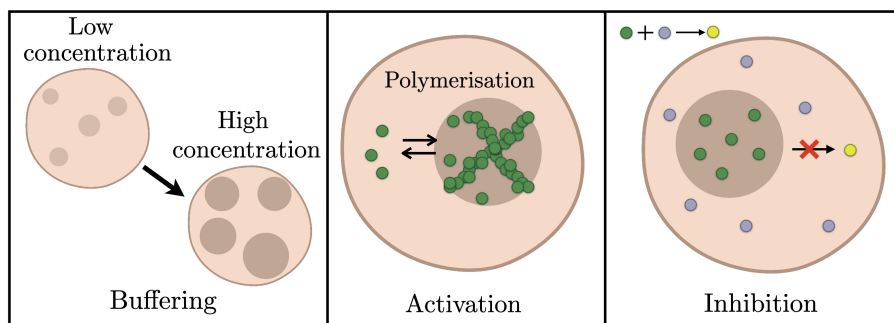


Fig. 1.2: Schematic representation of the functional repertoire of biomolecular condensates. Buffering capacity of concentrations, activation, and inhibition of chemical reactions via localization are some of the important functions of condensates that we study in detail in this work.

ity to concentrate or exclude molecules at specific locations. One important consequence of concentrating molecules is affecting biochemical reaction kinetics (Fig. 1.2).

Some examples include condensates of actin-signaling proteins LAT or nephrin concentrate actin [22, 23], and pericentriolar material condensates of SPD-5, ZYG-9, and TPXL-1 localizing tubulin [24], enhancing actin or tubulin polymerization, respectively. Super-enhancers enhance transcriptional output by concentrating transcription factors and RNA polymerase II [25]. Conversely, condensates can inhibit reactions or organelle activity. The phase separation of yeast translation termination factor Sup35 into reversible gels corresponds to translation inhibition and protection against pH-induced stress [26]. Similarly, condensates of the RNA transport granule protein FMRP concentrate translational inhibitors and suppress translation *in vitro* [27]. Membrane-bound organelles such as mitochondria are sequestered in an inactive state in dormant oocytes by rigid Balbiani bodies [28] (green hue in Fig. 1.1).

In addition to controlling reaction kinetics, condensates also modulate reaction specificity (e.g., by excluding inhibitory molecules). LAT signaling clusters exclude phosphatases that suppress actin polymerization [22]. Different patterns of Caprin1 and FMRP phosphorylation control their co-phase separation and sub-compartmentalization, modulating the rate of mRNA deadenylation or translation [27]. Moreover, condensates control where reactions occur by clustering molecules in specific locations. For example, the clustering of synaptic vesicles and neurotransmitter receptors at presynaptic and postsynaptic regions is mediated by the phase separation of proteins such as Synapsin in the presynapse and SynGAP and PSD-95 in the postsynapse [29].

As listed above, there have been extensive experimental studies conducted to observe how, in multiple ways, biochemical reactions are affected in phase-separated compartments. A thorough theoretical understanding of how such reactions can be controlled and thus affected using such compartments had been missing. Through this work, we wish to address the two-way effects of these otherwise orthogonal mechanisms, viz., chemical reaction kinetics and phase separation. This understanding is important in the field's development because it helps decipher how cells' biochemical reactions are localized and what key properties of the compartments modify their kinetics. Additionally, it also provides key insights

into an important aspect of engineering synthetic life, which includes coupling compartmentalization and out-of-equilibrium chemical reaction networks.

The cell, despite being the smallest unit of life, is, in fact, the absolute example of complexity. Isolating any intricately connected processes ongoing in a cell is very challenging, showcasing the importance of a reconstituted "life-in-a-test tube" approach to finely distinguish the mechanisms leading to the formation of phase-separated compartments and their downstream effects on chemical reactions. A major challenge in bottom-up synthetic biology is designing and building synthetic cell-like entities with lifelike properties. To generate such cell-like compartments, semipermeable protein-polymer microcapsules (proteinosomes) [30, 31, 32] and membrane-less coacervate microdroplets [33, 34] are a few of the candidates used. Multi-compartmentalization is one property in living systems in which distinct subcompartments have specialized microenvironments which allow for selective partitioning of biomolecules [35]. Spatiotemporal control of the formation of different subcompartments, such as membrane-less organelles, plays a key role in regulating the localization of functional biomolecules, which can be used to control biochemical reactions [19]. The programmable spatial organization of different sub-microcompartments was realized upon the regulation of external environmental changes, which was used to control the reaction rates of biochemical reactions or signaling processes in synthetic cells [36, 32]. In this work, we advance in this direction from a theoretical perspective expecting to provide insights into new approaches for the hierarchical spatial organization of various biomacromolecules and organelles inside synthetic cells. This would also contribute to developing novel microreactors with the tunable release of various bio-macromolecular cargoes and spatiotemporal regulation of biochemical reactions.

We now proceed to discuss the foundational concepts from statistical physics to lay the groundwork for understanding the interplay between phase separation and chemical reactions.

1.2 Thermodynamics of phase separation in a multi-component mixture

1.2.1 Mean field free energy

It is well established that the cell is inherently multi-component in nature, and our objects of interest, the membrane-less organelles are too [20, 21]. To study the thermodynamics of phase separation of a multi-component mixture, we proceed to define the Gibbs free energy (in an $(\{N_i\}, p, T)$ ensemble) for $(L + 1)$ components as follows,

$$G(\{N_i\}, p, T) = k_B T \left[\sum_{i=0}^L N_i \log \left(\frac{\nu_i N_i}{V} \right) + V \sum_{i,j=0}^L \frac{\chi_{ij}}{2\nu_0} N_i N_j \right] + \sum_{i=0}^L \omega_i N_i + pV, \quad (1.1)$$

where $\{N_i\}$ represents the set of particle numbers (we will use this notation for a set throughout this work) of all components indexed by i with $(i = 0)$ index used explicitly for the solvent in this work (unless stated otherwise), p is the pressure, T is the temperature, and k_B is the Boltzmann constant. The free energy is modeled following

the mean-field Flory-Huggins lattice model [4, 5, 6], with the first term representing the mixing entropy of all components with individual molecular volume ν_i , the second term accounting for short-range interactions between components i and j parametrized by a non-dimensional symmetric interaction parameter, χ_{ij} ¹ (in general, they can originate from various physical interactions that may include dipolar, van der Waals interactions, screened electrostatic interactions between charged molecular groups, or entropy-driven hydrophobic interactions [37]) and the third term corresponding to the internal energy, ω_i of component i originating from its internal degrees of freedom.

The system volume is, $V = \partial G / \partial p |_{\{N_i\}, T}$, the entropy is $S = -\partial G / \partial T |_{\{N_i\}, p}$ and the chemical potential of component i is $\mu_i = \partial G / \partial N_i |_{\{N_{j \neq i}\}, p, T}$.

An incompressible system satisfies the condition $-(1/V)\partial V / \partial p |_{\{N_i\}, T} = 0$, implying that the volume of the system is independent of pressure. The volume of the incompressible mixture can therefore be written as $V = \sum_{i=0}^L \nu_i N_i$, where the molecular volume, $\nu_i = \partial V / \partial N_i |_{\{N_{j \neq i}\}, T}$ is constant.

For the scope of this work, we restrict ourselves to incompressible systems. Thus we can define the corresponding Helmholtz free energy, $F = G - pV$, in a canonical ensemble. Given the system volume is independent of pressure and only depends on the number of particles, we can eliminate one of the particle numbers while performing the corresponding Legendre transformation, which changes the description from the $(\{N_i\}, p, T)$ isothermal-isobaric ensemble to the $(\{N_i\}, V, T)$ canonical ensemble. A common choice, and one that we also use throughout this work (except chapter 2), is to eliminate the solvent particle number N_0 and express it as a function of the volume and the rest of the particle numbers as,

$$N_0 = (V - \sum_{i=1}^L \nu_i N_i) / \nu_0. \quad (1.2)$$

An immediate consequence of eliminating the solvent component is the appearance of new thermodynamic conjugate variables in the canonical ensemble. To understand this better, we look at the differential of the Gibbs free energy, $dG = -SdT + Vdp + \sum_{i=0}^L \mu_i dN_i$ [38, 39] and use it to read out the differential of the Helmholtz free energy $dF = d(G - pV)$ as,

$$\begin{aligned} dF(\{N_i\}, V, T) &= -SdT - pdV + \mu_0 dN_0 + \sum_{i=1}^L \mu_i dN_i \\ &= -SdT - pdV + \mu_0 \left(\frac{dV}{\nu_0} - \sum_{i=1}^L \frac{\nu_i}{\nu_0} dN_i \right) + \sum_{i=1}^L \mu_i dN_i \\ &= -SdT - \left(p - \frac{\mu_0}{\nu_0} \right) dV + \sum_{i=1}^L \left(\mu_i - \mu_0 \frac{\nu_i}{\nu_0} \right) dN_i. \end{aligned} \quad (1.3)$$

We can identify the new thermodynamic conjugate variables to volume and particle number, from above, as the osmotic pressure, Π and exchange chemical potential, $\bar{\mu}_i$, respec-

¹ $\chi_{ij} \equiv \frac{z}{2} \frac{2e_{ij} - e_{ii} - e_{jj}}{k_B T}$, where z is the lattice coordination constant, e_{ij} is the cross contact energy and e_{ii}, e_{jj} are the self contact energies, also known as the Flory-Huggins interaction parameter [5, 4].

tively,

$$\Pi = p - \frac{\mu_0}{\nu_0}, \quad (1.4a)$$

$$\bar{\mu}_i = \mu_i - \mu_0 \frac{\nu_i}{\nu_0}. \quad (1.4b)$$

The osmotic pressure, Π is essentially the pressure that is required to be applied to the mixture to prevent the solvent from flowing through the semi-permeable membrane [40, 41]. The exchange chemical potential of component i , $\bar{\mu}_i$ defines the free energy cost of exchanging one particle of component i for a number of solvent particles occupying the same volume.

For the purpose of this work, we choose to use a variable that can interchangeably be used with concentrations $n_i = N_i/V$, which is the volume fraction. It is defined as,

$$\phi_i = \nu_i n_i. \quad (1.5)$$

We can therefore write the bulk free energy density of a homogeneous system in the fixed volume ensemble $f_0(\{\phi_i\}, T) = F(\{N_i\}, V, T)/V$ as,

$$\begin{aligned} f_0 = & \frac{k_B T}{\nu_0} \left[\sum_{i=1}^L \frac{\phi_i}{r_i} \log \phi_i + \left(1 - \sum_{i=1}^L \phi_i\right) \log \left(1 - \sum_{i=1}^L \phi_i\right) \right. \\ & \left. + \sum_{i,j=1}^L \frac{\chi_{ij}}{2} \phi_i \phi_j + \sum_{i=1}^L \frac{\chi_{0i}}{2} \phi_i \left(1 - \sum_{j=1}^L \phi_j\right) \right] + \sum_{i=1}^L \omega_i \phi_i + \omega_0 \left(1 - \sum_{j=1}^L \phi_j\right), \end{aligned} \quad (1.6)$$

having used the relation in Eq. (1.2) but with volume fractions as $\phi_0 = (1 - \sum_{i=1}^L \phi_i)$, which is a consequence of incompressibility of the system. Here we use $r_i = \nu_i/\nu_0$ as a multiplicative factor to express the molecular volume of all components, ν_i , in terms of the solvent molecular volume, ν_0 . The interaction parameter matrix, χ_{ij} , is symmetric with no self-interaction terms, i.e., $\chi_{ii} = 0$, as a choice we use throughout this work.¹ So far, we have discussed the homogeneous bulk free energy density Eq. (1.6), which neglects the contribution of interfacial free energy density. However, for a generalized treatment, we define a total free energy density, including the interface contributions as,

$$f = f_0(\{\phi_i\}, T) + \sum_{i,j=1}^L \frac{\kappa_{ij}}{2} (\nabla \phi_i)^2. \quad (1.7)$$

We can approximate the free energy density as an expansion in terms of the volume fraction gradient $\nabla \phi_i$, a vector. Since the free energy density is a scalar and we are probing near its minima, the term proportional to $\nabla \phi_i$ is negligible. The most general lowest-order term is the quadratic expression $\kappa_{ij} \nabla \phi_i \cdot \nabla \phi_j$, a scalar [42]. Here κ_{ij} is a parameter that controls the free energy cost of variations in volume fraction, ϕ_i . For the purpose of this work, we consider $\kappa_{ij} = 0$ for $i \neq j$ and κ_{ii} , simply used as κ_i (as in Eq. (1.7)), when we

¹Note that the interaction parameter and internal energy in Eq. (1.1) have to be rescaled to $\chi_{ij} \frac{V^2}{\nu_i \nu_j}$ and $\frac{\omega_i}{\nu_i}$, respectively when used in Eq. (1.6), such that the interaction parameter remains dimensionless and internal energy has dimensions $[ML^2T^{-2}]$.

take into consideration interfacial contributions.

1.2.2 Other possible free energy considerations: Beyond mean-field

It is important to note that in the biological context, it is usually intrinsically disordered proteins (IDPs) and RNAs that constitute the membrane-less organelles [43, 44], and these biomacromolecules are multivalent in nature.

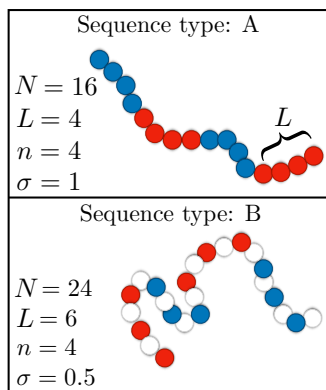


Fig. 1.3: Schematic of charged sequence of polymers. Two samples of polymers with charged sequence, characterized by the total number of monomers N (chain length), length of an individual block L , the number of charged blocks n , and the fraction of monomers that are charged, σ . The unit or neutral charges are represented by +1 (blue), -1 (red), and 0 (white), respectively.

Multivalency gives rise to interactions that are usually sequence-dependent to drive phase separation [14, 45]. The application of mean-field theory, like the Flory-Huggins lattice model, which was developed originally to study chemically synthesized homopolymers for which all monomers are identical, does not consider effects on phase separation due to charge sequence along the polymer. Therefore, as far as interactions are concerned, the monomers are treated as independent particles, and the quadratic in volume fraction (ϕ^2) formulation is appropriate only for contact-like interactions within a short spatial range. Since the inter-monomer interactions are solvent-mediated, χ contains enthalpic as well as entropic contributions in general and is expected to be sensitive to salt, pH [46], and other environmental conditions. As such, fitted χ parameters can be used to rationalize experimental data on biomolecular condensates [47].

To demonstrate the effects of charge sequence on phase diagrams, we also study in this work the random phase approximation (RPA) formulation for interaction energy by considering the spatial correlation of local variations in polymer density [48, 37]. By treating a part of this correlation that arises from chain connectivity, RPA accounts approximately for the sequence dependence of liquid-liquid phase separation. In technical terms, the interaction free energy in RPA, which involves a statistical mechanical integration over polymer density variations, is a sequence-sensitive function of polymer volume fraction ϕ [49, 50]. The free energy density is,

$$f_{\text{RPA}} = \frac{k_B T}{\nu_0} \left[\sum_{i=1}^L \frac{\phi_i}{r_i} \log(\phi_i) \right] + f_{\text{int}}, \quad (1.8a)$$

where the entropic contribution is similar as in Eq.(1.6), and the interaction enthalpy contribution $f_{\text{int}} = f_{\text{el}}$ originates due to Coulombic interaction potential with a physical short-range cutoff at monomer size, b , given by,

$$U(r) = \frac{l_B(1 - \exp(-r/b))}{r}, \quad (1.8b)$$

where $l_B = e^2/4\pi\epsilon_0\epsilon_r k_B T$ is the Bjerrum length, e is the electronic charge, r is the spatial distance between electric charges, ϵ_0 is the vacuum permittivity and ϵ is the dielectric constant. Using the RPA approximation, after the elimination of the electrostatic self-energy (for details, see Appendix.A),

$$f_{el} = \frac{1}{2} \int \frac{d^3k(\nu_0)^3}{(2\pi)^3} \left[\log [\det(1 + \hat{G}_k \hat{U}_k)] - \text{Tr}(\hat{\rho} \hat{U}_k) \right], \quad (1.8c)$$

where $\hat{\rho}$ is a diagonal matrix that contains the densities of the charged components,

$$\hat{\rho} = \begin{pmatrix} (\rho_m/N) \hat{I}_N & 0 \\ 0 & \hat{\rho}_I \end{pmatrix}, \quad (1.8d)$$

with ρ_m being monomer density, \hat{I}_N is an N dimensional identity, $\hat{\rho}_I$ is a 2×2 diagonal matrix for the charge of the positive and negative monovalent ions (salt or counterion to account for electro-neutrality) and \hat{U}_k is the k -space representation of Eq. (1.8b),

$$\hat{U}_k = \frac{4\pi l_B}{k^2 [1 + (kb)^2]} |q\rangle \langle q| \equiv \lambda(k) q \langle q|, \quad (1.8e)$$

where $|q\rangle$ is the column vector for the charges of the monomers and the monovalent ions. The bare correlation matrix \hat{G}_k combines the monomer-monomer correlation for a Gaussian chain, and the density matrix for the small monovalent ions is,

$$\hat{G}_k = \begin{pmatrix} (\rho_m/N) \hat{G}_M(k) & 0 \\ 0 & \hat{\rho}_I \end{pmatrix}, \quad (1.8f)$$

where $\hat{G}_M(k)$ is a matrix of size $(N \times N)$, where N is the number of monomers in the polymer, which is treated as a Gaussian chain with the elements as $\hat{G}_M(k)_{ij} = \exp(-(kb)^2 |i - j|/6)$ [48]. For regular block polymers with repeated units as in Fig. 1.3, we can proceed to study the sequence properties dependent phase diagrams using a reduced temperature, T^* as a thermodynamic variable, defined by rescaling temperature with electrostatic energy. It is defined as follows,

$$T^* \equiv \frac{b}{l_B}. \quad (1.9)$$

1.2.3 Exchange chemical potential, chemical activity and osmotic pressure

The exchange chemical potential, $\bar{\mu}_i$ emerges as the conjugate thermodynamic variable to particle numbers N_i , as identified in Eq. (1.4b). It is defined as $\bar{\mu}_i = (r_i \nu_0) \frac{\delta f}{\delta \phi_i}$ and following from the free energy density definition in Eq. (1.7), we can calculate the exchange chemical potential as,

$$\bar{\mu}_i = k_B T \log(\bar{\gamma}_i \phi_i) + \bar{\mu}_i^0 - \kappa_i \nabla^2 \phi_i, \quad (1.10)$$

where $(\bar{\gamma}_i \phi_i)$ is the exchange chemical activity [51, 52, 53, 54], $\bar{\gamma}_i$ is the exchange chemical activity coefficient [55, 56] which is constant in the absence of interactions (all $\chi_{ij} = 0$),

$$\bar{\gamma}_i = \frac{1}{(1 - \sum_{j=1}^L \phi_j)^{r_i}} \exp \left[\sum_{j=1}^L r_i (\chi_{ij} - \chi_{0i} - \chi_{0j}) \phi_j \right], \quad (1.11)$$

and $\bar{\mu}_i^0$ is the exchange reference chemical potential,

$$\bar{\mu}_i^0 = k_B T [1 - r_i + r_i \chi_{0i}] + r_i \nu_0 (\omega_i - \omega_0). \quad (1.12)$$

The osmotic pressure is calculated as,

$$\Pi = - \left. \frac{\partial F}{\partial V} \right|_{\{N_i\}, T} = -f + \phi_i \frac{\partial f}{\partial \phi_i}. \quad (1.13)$$

Corresponding to the free energy density calculated using RPA, in Eq. (1.8a), there is no closed-form expression of the exchange chemical potential and osmotic pressure. However, it can be computed numerically for the purpose of visualization and further analysis.

1.2.4 Thermodynamic instability leads to phase separation

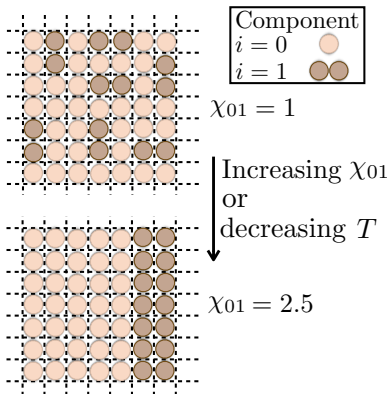


Fig. 1.4: Onset of phase separation in Flory Huggins lattice model. Increasing enthalpic contribution by increasing χ_{01} or reducing entropic contribution by lowering T can lead to phase separation. Here, we change χ_{01} to observe the same in a two-component system.

The onset of phase separation can be understood by studying the nature of the free energy densities, be it mean field Eq. (1.6) or beyond mean field Eq. (1.8). Due to interactions among the components, the system tends to separate into two homogeneous liquid phases with different compositions¹ if the sum of the free energies of both phases is lower than that of the well-mixed homogeneous phase. The previous statement can be expressed in terms of the free energy density as,

$$\frac{V^I}{V} f(\{\phi_i\}^I, T) + \frac{V^{II}}{V} f(\{\phi_i\}^{II}, T) < f(\{\bar{\phi}_i\}, T), \quad (1.14)$$

where $\{\bar{\phi}_i\}$ is the average volume fraction of all components in the system. In Eq. (1.14), we study the inequality in the thermodynamic limit where interfacial contributions are negligible in comparison to the bulk free energy density, or in other words when

system size $V^{1/3}$ becomes large compared to the lengthscales over which gradients occur in the system.

For specific interaction parameters, χ_{ij} or temperature T (Fig. 1.4), the free energy density

¹For the purpose of this work, we assume the presence of a maximum of two coexisting phases, which is ensured by a specific choice of interaction parameters χ_{ij} among the components. The solvent poor phase is labeled as phase I and the solvent-rich "dilute" phase is labeled as phase II.

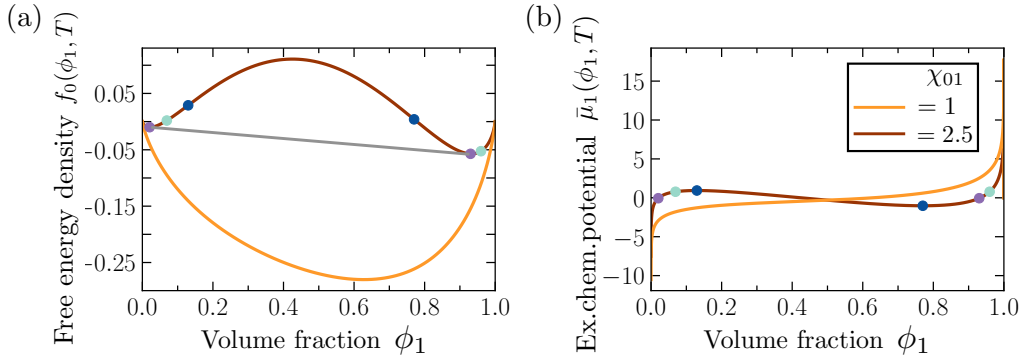


Fig. 1.5: Phase separation in a binary mixture. (a) Free energy density is concave between the spinodal points (blue dots) for $\chi_{01} = 2.5$ (brown), unlike for $\chi_{01} = 1$ (orange), which is convex in the whole domain. The binodal volume fractions (purple dots) can be connected by the common tangent (solid gray), and Laplace pressure effects shift the binodal volume fractions (light green dots). Asymmetry in free energy density can stem from the difference in molecular volumes or internal energies. (b) The exchange chemical potential at the binodal volume fractions for both the thermodynamic limit (purple dots) and finite system (light green dots) are equal at phase equilibrium. Parameters are listed in the L.O.F section.

can exhibit two local minima (binodal points) and two other points in composition space (spinodes or inflexion points) corresponding to which,

$$\det \hat{\mathcal{F}} = 0, \quad \mathcal{F}_{ij} = \frac{\partial^2 f}{\partial \phi_i \partial \phi_j}, \quad (1.15)$$

where $\hat{\mathcal{F}}$ is the Hessian matrix of the free energy density. The concavity of the free energy density ($\det \hat{\mathcal{F}} < 0$) condition defines the spinodal phase separation region in which the demixed state is globally more favorable. It is because the determinant of a matrix is equal to the product of all its eigenvalues, and this instability condition indicates that one, but not both (since binary mixture), of the eigenvalues of $\hat{\mathcal{F}}$ is negative. This means that second-order perturbations of free energy density with respect to ϕ_i 's along the direction of the corresponding eigenvector diverge, signaling that the system cannot maintain a homogeneous phase. For volume fractions within the spinodal region, a homogeneous solution is unstable against infinitesimal fluctuations in density or composition. There is no thermodynamic barrier to the growth of a new phase. Thus, the spinodal represents the limit of physical and chemical stability. To reach the spinodal region of the phase diagram, a transition must take the mixture through the binodal region or the critical point. Often phase separation will occur via nucleation during this transition, and spinodal decomposition will not be observed. To observe spinodal decomposition, a very fast quench in the control parameters χ_{01} or T is required to move from the stable to the spinodal unstable region of the phase diagram.

1.2.5 Phase equilibrium conditions

As is conventional, the phase boundaries are coexistence curves satisfying the binodal condition, which corresponds to the equality of exchange chemical potentials and osmotic

pressure across phase boundaries. They, therefore, may be determined graphically by constructing a common tangent (also referred to as Maxwell's tangent construction or construction of the convex hull) [57]. In an $(L + 1)$ - component mixture at phase equilibrium, the number of unknown variables is $(2L + 2)$, being the equilibrium volume fractions of all components in the two coexisting phases.¹ The minimum of the free energy density defines the phase equilibrium for finite systems with system size V . This minimization is subject to $(L + 1)$ constraints, namely conservation of material ($V\bar{\phi}_i = V^I\phi_i^I + V^{II}\phi_i^{II}$) for $i = 1, \dots, L$ and incompressibility ($V^I + V^{II} = V$).

Imposing the constraints reduces the unknown variables to $(L + 1)$, and we, therefore, require an equal number of conditions to determine the equilibrium volume fractions. The conditions are as follows,

$$\bar{\mu}_i(\{\phi_i^I\}) = \bar{\mu}_i(\{\phi_i^{II}\}), \quad (L \text{ conditions}) \quad (1.17a)$$

$$\Pi^I = \Pi^{II} + \frac{2\xi}{R}, \quad (1 \text{ condition}) \quad (1.17b)$$

where $(2\xi/R)$ is the additional correction to the pressure balance condition due to Laplace pressure which is proportional to the interface curvature R^{-1} and thus disappears in the thermodynamic limit ($R \rightarrow \infty$). ξ is the measure of surface tension in the system (for details, see [59, 57]).

The equilibrium volume fractions, $\{\phi_i^I\}$ and $\{\phi_i^{II}\}$, obtained on solving Eq. (1.17) make up the binodal manifold in the phase diagram. Equivalently, $(L + 1)$ conditions using chemical potentials, $\mu_i(\{\phi_k\}) = \mu_i(\{\phi_k\})$ can be simultaneously solved. For instance, Fig. 1.6 depicts the phase diagram of a binary and ternary mixture. Equation (1.17a) can be equivalently expressed as equality of exchange chemical activities in both phases [56],

$$\bar{\gamma}_i^I\phi_i^I = \bar{\gamma}_i^{II}\phi_i^{II}. \quad (1.18)$$

The components can partition unequally in the two phases, which is described by its partition coefficient, defined as

$$P_i \equiv \frac{\phi_i^I}{\phi_i^{II}}. \quad (1.19)$$

At phase equilibrium Eq. (1.17), the partition coefficients can be expressed in terms of the exchange activity coefficients in both phases, $\bar{\gamma}_i^{I/II}$, by using Eq. (1.18) as

$$P_i = \frac{\bar{\gamma}_i^{II}}{\bar{\gamma}_i^I}. \quad (1.20)$$

This expression reveals that partitioning is governed by the composition dependence of exchange activity coefficients $\bar{\gamma}_i^{I/II}$ in phase separating systems (Eq. (1.11)).

¹The maximum number of possible coexisting phases can be determined by the Gibbs phase rule for an incompressible non-reacting multicomponent mixture [58, 40],

$$n_d = n_c - n_p + 1. \quad (1.16)$$

For $n_c = (L + 1)$ component mixture, the maximum number of possible phases, corresponding to $n_d = 0$ degrees of freedom, is $n_p^{\max} = (L + 2)$.

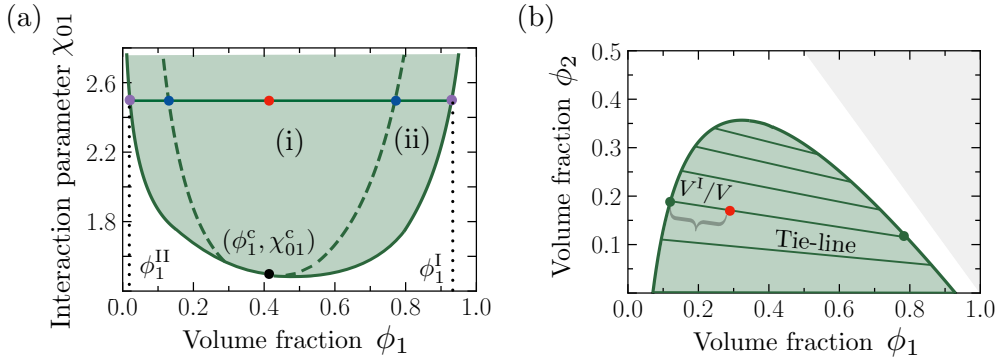


Fig. 1.6: Phase diagrams for mean field models. Phase diagrams corresponding to (a) binary ($L = 1$) and (b) ternary ($L = 2$) mixtures. In the shaded domain, the demixed state is preferred. An average volume fraction $\{\bar{\phi}_i\}$ (red dot) decomposes to equilibrium volume fractions $\{\phi_i^I\}$ and $\{\phi_i^{II}\}$ on the binodal manifold (purple dots for binary and dark green dots for ternary). The phase volume V^I/V is set by the lever rule originating due to material conservation. For binary mixture, we can also identify the critical point (black dot). Parameters are listed in the L.O.F section.

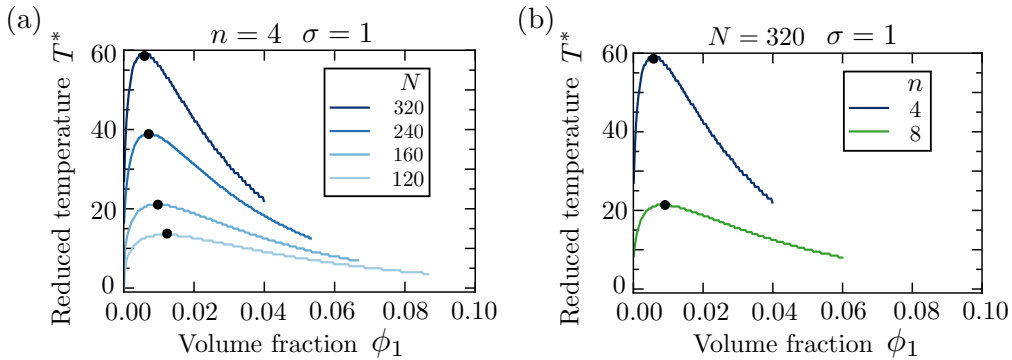


Fig. 1.7: Phase diagrams for beyond mean-field models. Phase diagrams corresponding to binary mixtures of charged sequence polymers and solvent, with free energy density calculated as in Eq. (1.8a). We see that the sequence parameters affect the binodal manifold and also the critical points (black dots). (a) Longer charged sequences (larger N) with (b) fewer blocks (smaller n) have stronger tendencies to phase separate.

Interpretation of a phase diagram

Both from a theoretical and experimental perspective, the construction and understanding of phase diagrams are crucial [47, 60]. In a binary mixture, one axis is for the volume fraction, and the other axis can correspond to the concentration of salt, pH [46], interaction strength, or temperature [47]. In Fig. 1.6(a), we use the interaction parameter χ_{01} . On the contrary, a ternary phase diagram (Fig. 1.6(b)) is spanned by the volume fractions of two components for a fixed temperature or interaction parameter. It, therefore, provides the information that, given all other conditions are fixed, how we can locate the demixed region in the volume fraction space.

The common aspects for both cases are as follows: Corresponding to any unstable average volume fraction (red dots in Fig. 1.6) in the green shaded domain; one can read out the equilibrium volume fractions and also the phase volumes of the coexisting phases. Each pair of equilibrium volume fractions, $\{\phi_i^I\}$ and $\{\phi_i^{II}\}$, are connected by a tie-line (solid

green in Fig. 1.6). In the binary phase diagram, we also depict the spinodal (dashed green line) and the spinodes (dark blue dots).

For completion, we also study phase diagrams of charged sequence polymers in binary mixtures using RPA (Fig. 1.7). The free energy density is simplified and analytically tractable for periodic block-charged sequences. However, it is not possible to derive the analytic form of the exchange chemical potential and osmotic pressure. We, therefore, proceed to calculate these quantities numerically. As a downstream consequence, calculating the equilibrium volume fractions is numerically expensive.

1.2.6 Relaxation dynamics to phase equilibrium

To study the relaxation of the system to its phase equilibrium state, we proceed to write down the conservation equation given by,

$$\frac{\partial \phi_i}{\partial t} = -\nabla \cdot \mathbf{j}_i, \quad (1.21)$$

where \mathbf{j}_i is the linear response diffusive flux of component i and is defined as,

$$\mathbf{j}_i = -\sum_k M_{ik} \nabla \bar{\mu}_k. \quad (1.22)$$

Here, M_{ik} is the volume fraction dependent non-diagonal mobility matrix, with the following form [61]:

$$M_{ii} = m_{0i} \phi_i \left(1 - \phi_1 - \sum_{i=2}^{L+1} \phi_i\right) + \sum_{\substack{k \neq i, \\ k=1}}^{L+1} m_{ik} \phi_i \phi_k, \\ M_{ik} = -m_{ik} \phi_i \phi_k, \quad \forall i \neq k, \quad (1.23)$$

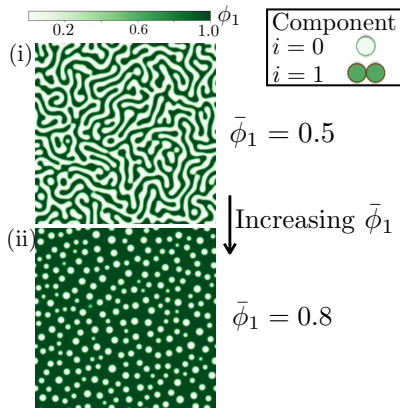


Fig. 1.8: Spinodal decomposition and nucleation. Transient snapshots of (i) spinodal decomposition and (ii) nucleation in a binary mixture. In the latter case, the solvent is less abundant in the system and therefore forms the spherical solvent-rich "dilute" phase. These regions are highlighted in Fig. 1.6(a) in the phase diagram for a binary mixture with the interaction parameter choice $\chi_{01} = 2.5$. Parameters are listed in the L.O.F section.

with m_{ik} being constant diffusion coefficients. Using the exchange chemical potential as obtained in Eq. (1.10) and substituting in Eq. (1.21), we obtain a modified Cahn-Hilliard equation tailored for the Flory-Huggins free energy density. When one phase is significantly more abundant, this equation can show the phenomenon known as Ostwald ripening, where the minority phase forms spherical droplets (as in Fig. 1.8(ii)), and the smaller droplets are absorbed through diffusion into the larger ones. It is important to note here the well-known Cahn-Hilliard equation [42] is specifically obtained in a binary mixture with the Ginzburg-Landau bi-quadratic free energy density of the form

$$f = \frac{1}{4}(\phi^2 - 1)^2 + \frac{\kappa}{2}(\nabla\phi)^2.$$

1.3 Thermodynamics of chemical reactions in homogeneous mixtures

In an $(L + 1)$ homogenous mixture, we consider chemical reactions $\alpha = 1, \dots, R$,

$$\sum_{i=1}^L \sigma_{i\alpha}^+ C_i \rightleftharpoons \sum_{i=1}^L \sigma_{i\alpha}^- C_i, \quad (1.24)$$

of chemical species C_i , where $\sigma_{i\alpha}^\pm$ are stoichiometric matrices. In Eq. (1.24), reactants are on the left side (+), while reaction products are on the right side (-). Given $(L - 1)$ chemical species undergoing R linearly independent reactions, there exist $(L - R)$ conserved quantities ψ_i , where $i = 1, \dots, L - R$. The reaction free energies corresponding to reaction α are

$$\Delta\mu_\alpha \equiv \sum_{i=1}^L \sigma_{i\alpha} \bar{\mu}_i, \quad (1.25)$$

where we abbreviate $\sigma_{i\alpha} = \sigma_{i\alpha}^- - \sigma_{i\alpha}^+$. The basis vectors spanning the nullspace of the matrix $\nu_i \sigma_{i\alpha}$ define linearly independent conserved quantities ψ_i [62].

1.3.1 Chemical equilibrium conditions

The condition for chemical equilibrium reads [40]

$$\Delta\mu_\alpha = 0. \quad (1.26)$$

Together with maximal R conditions as Eq. (1.26) and $(L - R)$ conserved quantities, a simultaneous solution provides L chemical equilibrium volume fractions.

At chemical equilibrium, the volume fractions reach equilibrium values that can be used to define the equilibrium reaction coefficients as

$$K_\alpha \equiv \prod_{i=1}^L (\phi_i)^{\sigma_{i\alpha}}, \quad (1.27)$$

which are distinct from the equilibrium reaction constants that include the chemical activities instead of concentrations or volume fractions [55].

At chemical equilibrium Eq. (1.26), the equilibrium reaction coefficients K_α can be expressed in terms of the stoichiometric coefficients, ex-

¹For the purpose of this work, we assume that the solvent ($i = 0$) is a non-reactive component. A general treatment is performed in Ref. [56]. We also assume that the reactions conserve volume, $\sum_{i=1}^L \sigma_{i\alpha} \nu_i = 0$.

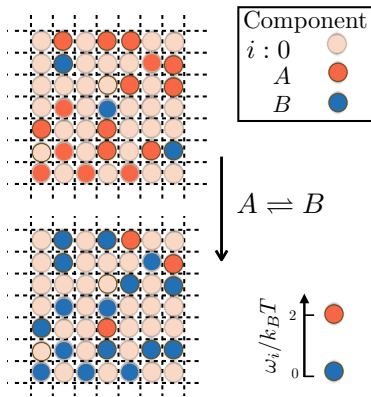


Fig. 1.9: Conversion between chemical species allows the onset of chemical equilibrium. Chemical reactions minimize free energy by proceeding toward the conversion to species with less internal enthalpies, thus satisfying the conditions governed by Eq. (1.26).

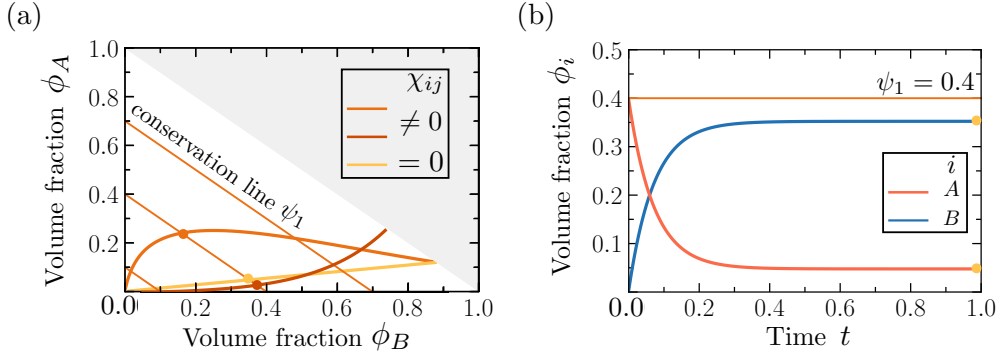


Fig. 1.10: Chemical equilibrium and conserved quantities. For a unimolecular reaction $A \rightleftharpoons B$, we depict the conserved quantity ψ_1 . The intersection of mono-nodal along which condition $\bar{\mu}_A = \bar{\mu}_B$ is satisfied with $\psi_1 = 0.4$, allows determination of volume fractions at chemical equilibrium as seen on the (a) phase diagram (both finite and zero interactions) and at the (b) steady state of reaction kinetics, in the case for $\chi_{ij} = 0$. Parameters are listed in the L.O.F section.

change activity coefficients, and exchange reference chemical potentials as,

$$K_\alpha = \prod_{i=1}^L \bar{\gamma}_i^{-\sigma_{i\alpha}} \exp\left(-\frac{\sigma_{i\alpha} \bar{\mu}_i^0}{k_B T}\right). \quad (1.28)$$

The equilibrium reaction coefficients thus describe relationships between volume fractions at chemical equilibrium. These coefficients depend on composition via the exchange activity coefficients $\bar{\gamma}_i$ [53, 54].

In general, for given conserved quantities ψ_i , there exist a unique set of volume fractions ϕ_i that satisfy Eq. (1.27) and therefore correspond to chemical equilibrium. Figure 1.10(a) shows the example of a ternary mixture ($L = 2$) with a unimolecular reaction (Fig. 1.9), where the conserved quantity $\psi_1 = (\phi_A + \phi_B)$ is constant along the thin straight lines (light orange). The volume fractions at chemical equilibrium lie on the intersection of a line with constant ψ_1 with the line on which chemical equilibrium holds and Eq. (1.26) is satisfied (thick orange lines) in Fig. 1.10(a). We refer to this line as mono-nodal since it describes a single set of equilibrated volume fractions, as opposed to the binodal of phase separation, which characterizes pairs of equilibrated volume fractions.

It is interesting to note that in Fig. 1.10(a), the effect of finite interactions among the components. Strong repulsive interactions (any one $\chi_{ij} > 2$) impart a concavity to the mono-nodal (thick orange line), implying that the system also phase separates (thick light orange), unlike when interactions are attractive (all $\chi_{ij} < 0$) which implies a mixed state but the mono-nodal is convex (thick dark orange (Fig. 1.10)). In the absence of interactions, the mono-nodal is a straight line passing through the origin (thick yellow line). We demonstrate that for a ternary mixture with a unimolecular reaction, the components approach chemical equilibrium (yellow dots in Fig. 1.10(b)).

1.3.2 Relaxation to chemical equilibrium

As we studied in Sec. 1.2.6 for phase equilibrium, similarly, we can also study the dynamical equations that dictate the approach to chemical equilibrium. It is often referred to as mass-action kinetics. The conserved quantities ψ_i do not change as a function of time, unlike the quantities called reaction extents, ξ_α , which measure the cumulative number density of reaction events [63],

$$\frac{d}{dt}\xi_\alpha = s_\alpha, \quad (1.29)$$

where s_α is the net reaction rate defined as,

$$s_\alpha = s_\alpha^+ - s_\alpha^-. \quad (1.30)$$

It is, however, important to realize that the forward and backward reaction rates, s_α^\pm would satisfy the detailed balance of reaction rates,

$$\frac{s_\alpha^+}{s_\alpha^-} = \exp\left(-\frac{\Delta\mu_\alpha}{k_B T}\right), \quad (1.31)$$

where we can make a symmetric choice and write,

$$s_\alpha^\pm = k_\alpha(\{\bar{\phi}_i\}, p, T) \exp\left(\frac{\mu_\alpha^\pm}{k_B T}\right), \quad (1.32)$$

where μ_α^\pm are introduced as the forward (+) and backward (-) reaction free energies defined as,

$$\mu_\alpha^\pm = \sum_{i=1}^L \sigma_{i\alpha}^\pm \bar{\mu}_i. \quad (1.33)$$

This also provides the relation $\Delta\mu_\alpha = \mu_\alpha^- - \mu_\alpha^+$. Here we also introduce the reaction rate coefficients k_α (referred to as rate constants in literature) in a similar spirit as the diffusion coefficients m_{ik} Eq. (1.23) in Sec. 1.3.2. These reaction rate coefficients are not of thermodynamic origin as they may depend on pressure, temperature, or they can be phase dependent in the presence of coexisting phases due to differences in the physicochemical environment between the two phases. This property we use in subsequent chapters 4 and 5 to see how reactions can be suppressed in one phase or the other, thus localizing them to a specific physicochemical environment. Given the composition dependence of the phases, we can assume they make for different environments (discussed in detail in chapter 2).

It is therefore implied at chemical equilibrium, following Eq. (1.26), $s_\alpha^+ = s_\alpha^-$. The kinetic equation, therefore, for a chemically reacting component i can now be written as $\dot{\phi}_i = \sum_{\alpha=1}^R \nu_i \sigma_{i\alpha} s_\alpha$ explicitly as,

$$\frac{d}{dt}\phi_i = \sum_{\alpha=1}^R \nu_i \sigma_{i\alpha} k_\alpha \left[\exp\left(\frac{\mu_\alpha^+}{k_B T}\right) - \exp\left(\frac{\mu_\alpha^-}{k_B T}\right) \right]. \quad (1.34)$$

For the unimolecular reaction example where phase separation doesn't occur (no interactions, $\chi_{ij} = 0$), it can be straightforwardly shown following Eq. (1.34) that the rate is

linear in the volume fractions as exchange activity coefficient is a constant,

$$\begin{aligned} \frac{d}{dt}\phi_B(t) &= -\frac{d}{dt}\phi_A(t) \\ &= k \left[\exp\left(\frac{\bar{\mu}_A}{k_B T}\right) - \exp\left(\frac{\bar{\mu}_B}{k_B T}\right) \right]. \end{aligned} \quad (1.35)$$

For this simplified case, we have chosen, $\bar{\mu}_i = k_B T [\log(\phi_i/(1 - \phi_A - \phi_B))] + (\omega_i - \omega_0)$.

1.4 Thermodynamic equilibrium

"It may be noted that the condition.. (as in Eq. (1.26)) ..retains its form even when the reacting substances are distributed in the form of solutes in two different phases in contact. This follows from the fact that in equilibrium the chemical potentials of each substance in either phase must be equal, in accordance with the conditions for phase equilibrium." - Pg.306, Chp.X- Chemical Reactions, Statistical Physics, Part I, Vol.5; L.D. Landau and E.M. Lifshitz [40]

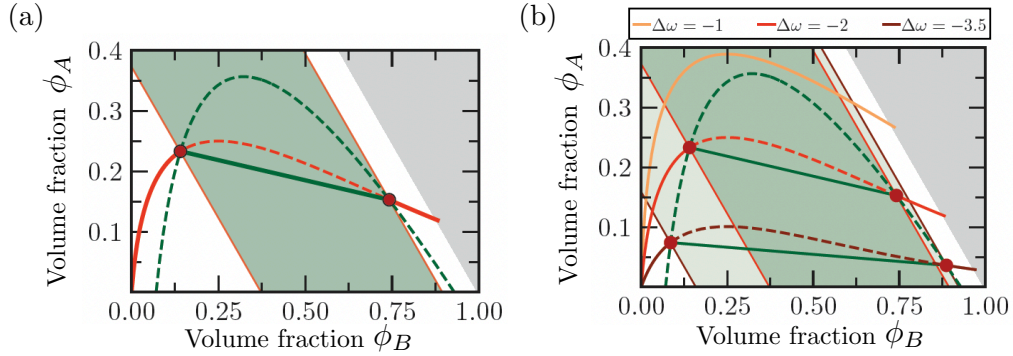


Fig. 1.11: Thermodynamic equilibrium. In a ternary mixture with a unimolecular reaction, the thermodynamic equilibrium for this system is depicted on a phase diagram. (a) In the white domain, the system remains mixed as it approaches its chemical equilibrium, dictated by the intersection of the conservation line with the mono-nodal (orange). In the green domain, the equilibrium is dictated by the green tie line on which lies the average volume fractions $\{\bar{\phi}_i\}$ and the thermodynamic equilibrium volume fractions (orange dots) in the coexisting phases, obtained by the intersections of the binodal (dashed green) and the chemical equilibrium mono-nodal, (b) Different thermodynamic equilibria can be reached for three parameter choices of internal energies ($\Delta\omega = \omega_B - \omega_A$). While the binodal remains affected under these parameter changes, the mono-nodal gets shifted. Parameters are listed in the L.O.F section.

If a system is at thermodynamic equilibrium and two phases coexist, both chemical reactions and phases are equilibrated. In this case Eq. (1.26) and Eq. (1.17) are obeyed simultaneously. As a consequence, thermodynamic equilibrium imposes a relation between equilibrium reaction coefficients and partition coefficients. In fact, equilibrium reaction coefficients, K_α^I and K_α^{II} , differ in the two coexisting phases, I and II. At thermodynamic equilibrium, their ratio obeys

$$\frac{K_\alpha^I}{K_\alpha^{II}} = \prod_{i=1}^L (P_i)^{\sigma_{i\alpha}}. \quad (1.36)$$

Equation (1.36) can select a subset of coexisting volume fractions on the binodal man-

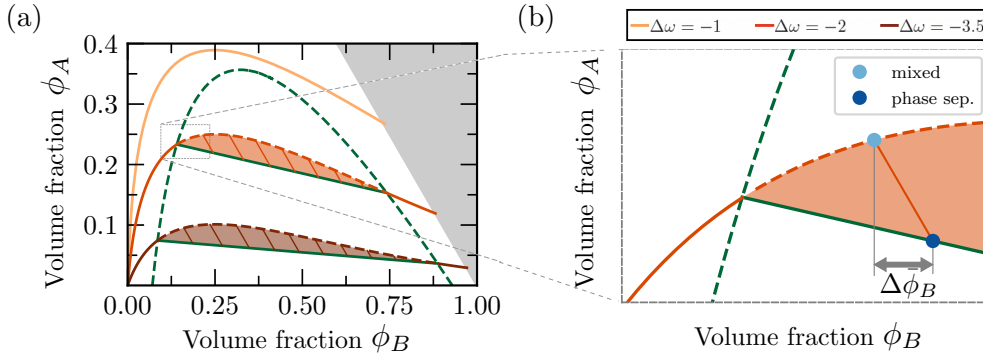


Fig. 1.12: Phase separation tunes chemical equilibrium. (a) Varying the difference of internal energies (ω_i , in turn reference chemical potential) between components B and A , $\Delta\omega$, leads to different chemical equilibrium lines (shades of orange mono-nodals) in the phase diagram. The orange lines in the shaded domains (b) characterize the difference between the phase-separated system at thermodynamic equilibrium and the corresponding mixed system (gray arrow), indicating that phase separation can control chemical equilibrium and hence the volume fractions at equilibrium. Parameters are listed in the L.O.F section.

ifold if both equilibria are compatible. Combining the binodal and mono-nodal within one phase diagram represents a new concept that allows us to discuss how phase separation affects chemical reactions at equilibrium. The case of compatible equilibria is illustrated in the example of a ternary mixture shown in Fig. 1.11(a), where a unique pair of volume fractions coexist at thermodynamic equilibrium for a large range of conserved quantities (orange circles). Chemical and phase equilibria can also be incompatible. In this case, thermodynamic equilibrium corresponds to a homogeneous state that satisfies only chemical equilibrium Eq. (1.26); top orange solid lines in Fig. 1.11(a).

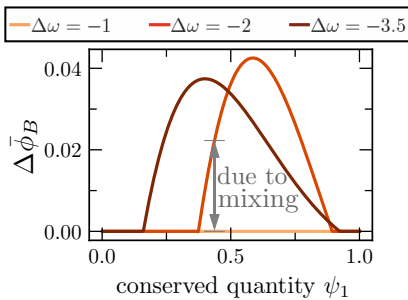


Fig. 1.13: Difference in average volume fractions due to mixing. $\Delta\{\bar{\phi}_i\}$ varies with the value of the conserved quantity ψ_1 , which is depicted by the compositional change of the B -component, $\Delta\bar{\phi}_B$, due to mixing. Parameters are listed in the L.O.F section.

with the value of the conserved quantity ψ_1 (Fig. 1.13). This dependence on ψ_1 solely

An important implication of our concept to combine the binodal together with the mono-nodal in one phase diagram is that phase coexistence leads to different equilibrium states compared to the corresponding mixed system. To illustrate this effect, we compare the average composition $\bar{\phi}_i$ of a system at phase coexistence to the same mixed system but at chemical equilibrium. Mixing can be realized by stirring, for example.

In the phase diagram, this comparison amounts to the deviation between the line of chemical equilibrium (dashed orange line in Fig. 1.12(a) and the tie-line (solid green line in Fig. 1.12(a), which is depicted by the orange domains in Fig. 1.12(b)).

Since the mixed case is only partially equilibrated, its composition is different from the composition at thermodynamic equilibrium. This difference varies

stems from mixing since for the considered ternary mixture with one chemical reaction at thermodynamic equilibrium, changing ψ_1 only affects the phase volumes and not composition in each phase. The difference between the homogeneous, partially equilibrated state and the phase-separated, thermodynamic state reflects the influence of phase coexistence on chemical reactions.

1.5 Scope of the thesis

In this work, we will proceed to study how compartmentalization, primarily driven by phase separation, affects chemical reactions, both equilibrium and out-of-equilibrium. To this end, we have laid down the thermodynamic framework required to tackle the subsequent questions in this introduction. With this knowledge, we proceed with organizing the remaining chapters of this work as follows.

Broadly, we divide this work into two parts. The first part, including chapters 2 and 3, proposes comprehensive theoretical formulations to study chemical reactions and phase separation. Specifically, in chapter 2, we will study the mass action kinetics at phase equilibrium. This assumes that the diffusion of all components is instantaneous and chemical reactions are rate-limiting, establishing phase equilibrium at all time points. Therefore, the kinetic trajectory of the components lies on the binodal manifold. This separation of time scales implies that the size of each phase is smaller than the reaction-diffusion length scales, which are set by the reaction rate coefficients and the diffusion coefficients. It is easy to follow that, given the system is always at phase equilibrium, the coexisting phases are homogeneous, and the whole formulation is based on solving ordinary differential equations of mass action kinetics at phase equilibrium. We also introduce out-of-equilibrium chemical processes and how we theoretically introduce implicit external energy sources to drive the system to non-equilibrium steady states (NESS) and further analyze these states. This chapter effectively incorporates studies when components react and phase separate simultaneously in the infinite diffusion limit.

In chapter 3, we decouple the dominant phase separating components (scaffold and solvent) from the reactive components (clients) on the basis of their composition, meaning the clients are much dilute compared to the scaffold and solvent. We then try to quantify observables like yield, initial rates, and throughput of three types of chemical reactions and ask the question: How are these observables controlled due to phase separation, specifically, the compartment volume, partition coefficients, phase-dependant external energy sources, reaction rate coefficients, and diffusion coefficients. For the last scenario, this effectively implies we study the clients' dynamics in a spatial system (finite diffusivities) and also at phase equilibrium (infinite limit of diffusivities). Given the diluteness of the clients, the spatial system reduces to solving coupled reaction-diffusion equations in the coexisting phases. We use these formulations then to quantify to what extent the aforementioned observables are affected by the presence of phase-separated compartments.

The second part includes chapters 4 and 5. It focuses on the applications of the theoretical frameworks developed in the first part to experimental problems addressing bottom-up approaches to design synthetic life-like systems.

Chapter 4 specifically deals with a systems chemistry experimental study involving a chemical reaction network (CRN) that consumes chemical fuel and forms phase-separating building blocks which are usually short-lived and sustained only in the presence of the chemical fuel. We apply the mass action kinetics theory at phase equilibrium for this study, subject to specific assumptions tailored to the system at hand. We unravel interesting emergent properties leading to control of the lifetime of the building blocks in the system, reminiscent of a "host-parasite" like behavior, and additionally draw conclusions related to the buffering capacity of phase separation in the system. Specific to this chapter, we refer to multicomponent phase separation (ternary) as co-phase separation.

In chapter 5, we investigate a systems biology experimental study wherein proteinosomes (micron-sized membrane-bound compartments formed from covalently linked protein-polymer conjugates) serve as reactors to localize the PEN DNA toolkit (out-of-equilibrium autocatalytic process). In this study, encapsulation of the DNA template sequence imparts a unique biochemical identity on the compartment. We compare the initial reaction rates for the CRN localized in the proteinosomes to that in the buffer solution and conclude that, indeed, the different physicochemical environment affects the kinetic reaction coefficients, which can lead to, therefore, increased efficiency of proteinosomes to act as reactors for autocatalytic processes. We finally conclude by summarizing the key results of this work and highlighting the outlooks in this area of research in chapter 6.

Chapter 2

Chemical reaction kinetics at phase equilibrium

"Everything should be made as simple as possible, but not simpler."

– Unverified

The motivation for this chapter relies on understanding the physicochemical principles that could shed light on how reaction rates can increase or decrease inside condensed phases as observed in recent experimental studies [64, 65, 66]

The objective of this chapter is to develop the theoretical model to study chemical reaction kinetics at phase equilibrium. This implies that we restrict ourselves here to the case where the reaction rate coefficients are smaller compared to the diffusion coefficients. Infinitely fast diffusion and slow reactions lead to suppression of gradients at relevant system size length scales, meaning the volume fractions are homogeneous in the coexisting phases at all time points, and their dynamics can be solved numerically by obtaining solutions of coupled non-linear ordinary differential equations. First, we introduce the kinetic equations and do case studies on a unimolecular reaction in a ternary mixture and a bimolecular reaction in a quaternary mixture. We follow this up with the introduction of out-of-equilibrium chemical reactions and the investigation of non-equilibrium steady states. This study was performed in collaboration with Jonathan Bauermann and Patrick McCall. The exact figures and results discussed in this chapter were developed and verified independently by Jonathan Bauermann and myself as co-authors and can be found in Ref.[56]. The plotting routine for Fig. 2.4 was provided by Jonathan Bauermann. This framework will be adapted for later implementation in chapter 4.

2.1 Kinetics of chemical reactions relaxing to thermodynamic equilibrium

We have discussed the thermodynamic equilibrium state and its properties in detail in the introduction (Sec.1.4). We proceed to study the kinetics of chemical reactions for systems composed of two homogeneous coexisting phases that are maintained at phase equilibrium but are not at chemical equilibrium. This condition of partial equilibrium holds when chemical reactions are slow compared to phase separation and corresponds to the case of reaction-limited chemical kinetics [67, 68]. We will discuss the implications of our theory for systems that can relax toward chemical equilibrium and systems that are maintained away from equilibrium. In this chapter, we assume solvent is non-reactive, but we do not replace the solvent volume fraction in the formalism, and it is only replaced

during numerical implementation (Appendix. B) using $\phi_0 = (1 - \sum_{i \neq 0} \phi_i)$.

2.1.1 Volume fraction field and phase volume kinetics

The rate of change of particle number N_i of all components ($i = 0, \dots, L$) in each phase due to chemical reactions occurring with the rate $S_i^{I/\text{II}}$ and the exchange rate $J_i^{I/\text{II}}$ between the phases is given by ($S_0^{I/\text{II}} = 0$ due to non-reactivity),

$$\frac{d}{dt} N_i^{I/\text{II}} = S_i^{I/\text{II}} - J_i^{I/\text{II}}. \quad (2.1)$$

Due to the conservation of the number of particles of individual components during the exchange between phases, $J_i^I = -J_i^{\text{II}}$.

Each phase volume is defined as the total volume occupied by all the components in each phase, $V^{I/\text{II}} = \sum_{i=0}^L \nu_i N_i^{I/\text{II}}$. Therefore, the dynamic equation for the phase volume is,

$$\frac{d}{dt} V^{I/\text{II}} = \sum_{i=0}^L \nu_i^{I/\text{II}} (S_i^{I/\text{II}} - J_i^{I/\text{II}}) + \sum_{i=0}^L N_i^{I/\text{II}} \frac{d}{dt} \nu_i^{I/\text{II}}. \quad (2.2)$$

We assume that the molecular volumes $\nu_i = \nu_i(p, T)$ are only functions of pressure p and temperature T and are not dependent on composition. In that case, they are constant and equal in both phases at isobaric and isothermal conditions and therefore $d\nu_i^{I/\text{II}}/dt = 0$. Now, dividing both sides of Eq. (2.1) with the respective phase volumes, multiplying with the molecular volume, and using the definition of volume fraction Eq. (1.5), we obtain Eq. (2.3a). In each phase, the kinetics of the respective volume fraction of component i , $\phi_i^{I/\text{II}}$ for $i = 0, \dots, L$ is governed by,

$$\frac{d}{dt} \phi_i^{I/\text{II}} = s_i^{I/\text{II}} - j_i^{I/\text{II}} - \frac{\phi_i^{I/\text{II}}}{V^{I/\text{II}}} \frac{d}{dt} V^{I/\text{II}}, \quad (2.3a)$$

where $s_i^{I/\text{II}} = \sum_{\alpha=1}^R \nu_i \sigma_{i\alpha} s_\alpha^{I/\text{II}}$ and s_α is as defined in Eq. (1.30), each with the units of particle number per time. Reaction rates are also defined with the extensive rate, $S_i^{I/\text{II}}$ as, $s_i^{I/\text{II}} = (\nu_i S_i^{I/\text{II}})/V^{I/\text{II}}$ in the phases with phase volume $V^{I/\text{II}}$ and $j_i^{I/\text{II}} = (\nu_i J_i^{I/\text{II}})/V^{I/\text{II}}$ are the diffusive exchange rates between phases. These rates maintain phase equilibrium at all times. Note that in this work, rates have units per time.

The last term of Eq. (2.3a) accounts for changes in volume fractions due to the changes of the respective phase volumes $V^{I/\text{II}}$. The kinetics of these phase volumes follow,

$$\frac{1}{V^{I/\text{II}}} \frac{d}{dt} V^{I/\text{II}} = \sum_{i=0}^L (s_i^{I/\text{II}} - j_i^{I/\text{II}}). \quad (2.3b)$$

For volume conserving reactions with $\sum_{i=0}^L \sigma_{i\alpha} \nu_i = 0$.

2.1.2 Diffusive exchange rates between phases

To maintain phase equilibrium while chemical reactions occur, components need to be exchanged between the phases. This exchange conserves the total number of components

in the system, which implies for the diffusive exchange rates $j_i^{I/II}$:

$$V^I j_i^I = -V^{II} j_i^{II}. \quad (2.4)$$

As a result, for systems with composition independent molecular volumes and volume conserving reactions, the total system volume $V = V^I + V^{II}$ is constant in time (see Eq. (2.3b)). The condition of phase equilibrium (Eq. (1.18)) at all times during the reaction kinetics implies that

$$\frac{d}{dt}(\gamma_i^I \phi_i^I) = \frac{d}{dt}(\gamma_i^{II} \phi_i^{II}). \quad (2.5)$$

Using Eq. (2.3) in Eq. (2.5) together with Eq. (2.4), gives a set of $(2L + 2)$ equations that are linear in the diffusive exchange rates $j_i^{I/II}$. Therefore, the diffusive exchange rates can be written in closed-form expressions $j_i^{I/II}(\{s_k^I, s_k^{II}\}, V^I, V^{II})$, which depend only on the chemical rates $s_k^{I/II}$ and the phase volumes $V^{I/II}$ (Appendix. B).

2.1.3 Reaction rates at phase equilibrium

Note that thermodynamics does not determine the value of the reaction rate coefficient as discussed in Sec.1.3.2. Rather, it only constrains the coefficient to be positive and thereby guarantees that the entropy of the system increases.

Using Eq. (1.32), the chemical reaction rate of component i can be written as,

$$s_i^{I/II} = \sum_{\alpha=1}^R \nu_i \sigma_{i\alpha} k_{\alpha}^{I/II} H_{\alpha}, \quad (2.6)$$

where we introduce the chemical reaction force,

$$H_{\alpha} = \exp\left(\frac{\mu_{\alpha}^+}{k_B T}\right) - \exp\left(\frac{\mu_{\alpha}^-}{k_B T}\right). \quad (2.7)$$

Here, we have also introduced the forward and backward chemical reaction free energies μ_{α}^{\pm} via $\Delta\mu_{\alpha} = \mu_{\alpha}^- - \mu_{\alpha}^+$. The chemical reaction force, H_{α} is by definition phase independent, and reaction rates $s_i^{I/II}$ can only owe their phase dependence to the reaction rate coefficients. Eqs. (2.3) together with the phase equilibrium conditions (Eq. (1.17)) and the chemical rates described by Eqs. (2.6) and (2.7), govern the kinetics of chemical reactions at phase equilibrium. These kinetic equations represent a key result of our work since they extend the chemical laws for dilute (as will be discussed in the following chapter 3) and homogeneous systems with reactions [69, 51, 53] to non-dilute and phase-separated systems. For systems that can relax to thermodynamic equilibrium, the chemical reaction force can thus be expressed in terms of the chemical activities as,

$$H_{\alpha} = \prod_{m=1}^L \left(e^{\frac{\bar{\mu}_m^0}{k_B T}} \bar{\gamma}_m \phi_m \right)^{\sigma_{m\alpha}^+} - \prod_{m=1}^L \left(e^{\frac{\bar{\mu}_m^0}{k_B T}} \bar{\gamma}_m \phi_m \right)^{\sigma_{m\alpha}^-}. \quad (2.8)$$

This form of the chemical reaction force is specific to systems that can relax to thermo-

dynamic equilibrium and imply various properties for chemical reactions at phase equilibrium. It is interesting to note that the reaction force, H_α , even for a linear reaction (unimolecular), is highly non-linear owing to the interactions in the free energy density from where the non-linear activity coefficients originate.

2.1.4 Properties of chemical reactions at phase equilibrium

First, at phase equilibrium, the chemical activities $\bar{\gamma}_i\phi_i$ are equal in both phases. For chemical reactions that can relax to thermodynamic equilibrium, equal chemical activities between the phases imply that the chemical reaction forces H_α (Eq. (2.7)) are equal in both phases as well. Note that the reaction forces are equal despite the composition difference between the phases. This key result emerges because chemical activities (or equivalently, chemical potentials) govern both the chemical kinetics of the components in the phases and their diffusion between the phases. Equal reaction forces H_α between phases imply that the component reaction rate $s_i^{I/II}$ shown in Eq. (2.6) is different between the phases only due to the composition dependent reaction rate coefficients $k_\alpha^{I/II}$.

Second, due to phase equilibrium, the rate of change of the volume fraction of a reactive molecule in one of the phases, $d\phi_i^{I/II}/dt$, is not equal to the chemical reaction rate $s_i^{I/II}$ of the component. The reason is that, in addition, the exchange of reactive components between the phases $j_i^{I/II}$ and changes in phase volumes $dV^{I/II}/dt$ contribute to volume fraction changes in each phase; see Eq. (2.3a). Both contributions are crucial since they maintain phase equilibrium during the chemical kinetics, i.e., the volume fractions $\phi_i^{I/II}$ remain on the binodal manifold, which is defined by the condition for phase equilibrium (Eq. (1.17)). Thus, determining reaction rates in each phase requires the knowledge of both the diffusive exchange rates between the phases and how the phase volume changes with time.

Third, the chemical kinetics at phase equilibrium differs from the kinetics of the corresponding mixed system. We already discussed in Figs. (1.12-1.13) that the thermodynamic state is distinct from the corresponding well-mixed system. In contrast to such well-mixed systems where the composition of the mixture governs the chemical kinetics, the chemical kinetics at phase equilibrium is determined by the chemical activities (or chemical potentials) along the binodal manifold together with the phase-dependent reaction rate coefficients. This difference can be illustrated when, for example, considering the kinetics of the average volume fractions, $\bar{\phi}_i = (V^I\phi_i^I + V^{II}\phi_i^{II})/V$. Using Eqs. (2.3), the corresponding kinetics is given by,

$$\frac{d\bar{\phi}_i}{dt} = \sum_{\alpha=1}^R \nu_i \left(\frac{V^I}{V} k_\alpha^I + \frac{V^{II}}{V} k_\alpha^{II} \right) \sigma_{i\alpha} H_\alpha, \quad (2.9)$$

for volume-conserving reactions. We find that in systems with coexisting phases I and II, the time evolution of the average composition is determined by the kinetics of the phase volumes $V^{I/II}$, the phase-dependent reaction rate coefficients $k_\alpha^{I/II}$ and a phase-independent reaction force H_α .

2.2 Unimolecular chemical reactions in coexisting phases

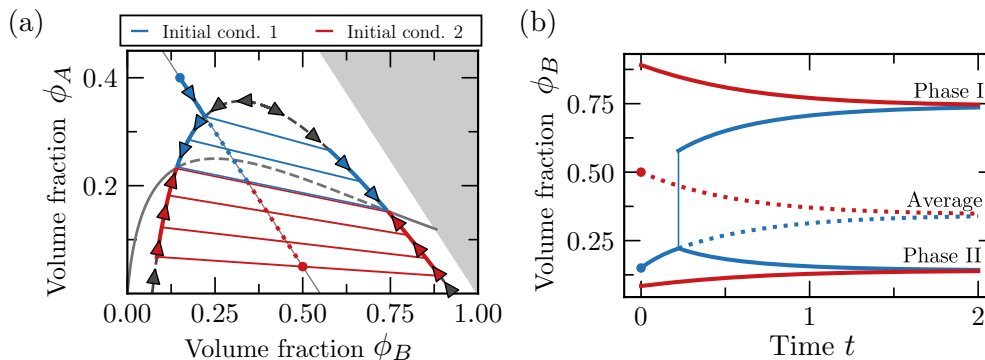


Fig. 2.1: Mass action kinetics of a unimolecular reaction at phase equilibrium. In a ternary mixture with a unimolecular reaction, for two choices of initial conditions, originating in the mixed phase (blue dot) and in the demixed phase (red dot), respectively, the kinetic trajectory evolves along the binodal manifold to approach thermodynamic equilibrium (Fig. 1.11(a)). (b) The kinetic trajectories of the average volume fraction $\bar{\phi}_B$, and phase volume fractions $\phi_B^{I/II}$. Parameters are listed in the L.O.F section.

In this section, we discuss an example of a ternary mixture with chemically reactive components A, B and a non-reactive solvent (0). For simplicity, we assume identical molecular volume $\nu_0 (r_{A/B} = 1)$ for all components. We consider a transition-like reaction whereby solute A can spontaneously convert to the product B and vice versa without the participation of any additional components. We refer to this reaction as a unimolecular chemical reaction,



Note that for systems that chemically react via unimolecular reactions and that can phase-separate, component reaction rates Eq. (2.6) are generally non-linear in the solute volume fractions. For such a unimolecular reaction in a ternary mixture, we can define one conserved quantity, $\psi_1 = (\phi_A + \phi_B)$. We numerically solve the governing kinetic equations of the unimolecular chemical reaction Eq. (2.10) at phase equilibrium; for details, see Appendix B.

The kinetics of a unimolecular chemical reaction at phase equilibrium can be illustrated as a chemical trajectory in a simple phase diagram spanned by two reactive components A and B (Fig. 2.1(a)). For an initial composition within the binodal (red dot in Fig. 2.1(a)), the volume fractions in each phase follow a flow field along the binodal lines (solid red lines in Fig. 2.1(a)). The corresponding average composition moves along the conserved quantity ψ_1 while crossing different tie lines (dotted red line in Fig. 2.1(a)). Changes in tie line as the chemical reaction proceeds imply corresponding compositional changes in the coexisting phases. For an initial composition outside the binodal (blue dot in Fig. 2.1(a)), the initially well-mixed system moves along ψ_1 , and phase separates into coexisting phases when the composition hits the binodal line (solid blue lines in Fig. 2.1(a)). The onset of phase separation leads to a discontinuity of the volume fractions, which otherwise evolve smoothly in time (Fig. 2.1(b)). Then, similar to the previous initial condition, the phase

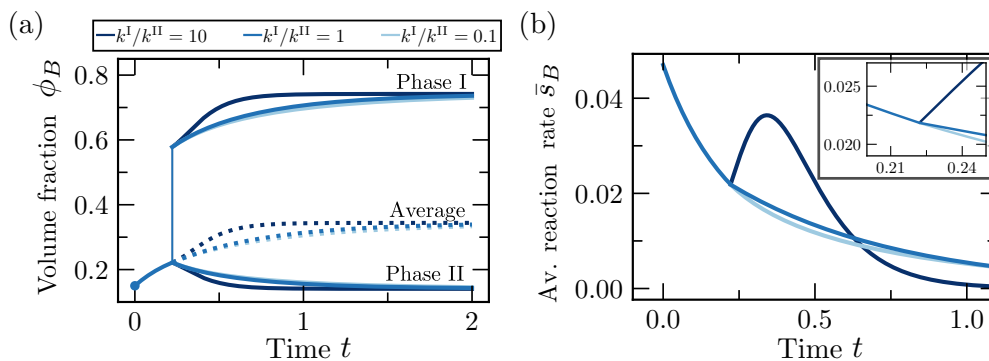


Fig. 2.2: Effects of dissimilar reaction rate coefficients between phases - I. Difference in reaction rate coefficients between phases affects (a) reaction rates (in both phases and average) but not the thermodynamic equilibrium state. The average volume fraction of product B changes continuously at the onset of phase separation for initial condition 1. (b) The average reaction rate of product B , \bar{s}_B has a kink at the onset of phase separation. Parameters are listed in the L.O.F section.

composition follows the flow along the binodal lines. Since both cases are identical except for their initial conditions, both relax to the same thermodynamic equilibrium state.

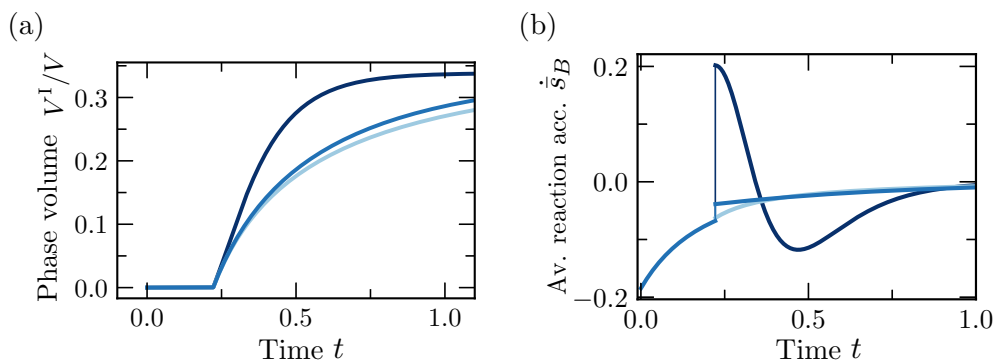


Fig. 2.3: Effects of dissimilar reaction rate coefficients between phases - II. Difference in reaction rate coefficients between phases affects (a) the phase fraction (V^I/V), \bar{s}_B has a kink at the onset of phase separation, implying that (b) average reaction acceleration of product B , $\dot{\bar{s}}_B$, jumps at the onset of phase separation. Please note that the kink and the jump require that phase equilibrium is established quasi-instantaneously on the time scales of chemical reactions. Parameters are listed in the L.O.F section.

Varying the reaction rate coefficients $k_\alpha^{I/II}$ in the phases can strongly alter the chemical kinetics (Fig. 2.2(a)). When the reaction rate coefficient is increased in the B product-rich phase ($k_\alpha^I/k_\alpha^{II} = 10$), the product B relaxes more quickly towards thermodynamic equilibrium. The same holds true for the average volume fraction of product B . Interestingly, at the onset of phase separation, the average reaction rate $\bar{s}_i = (V^I s_i^I + V^{II} s_i^{II})/V$ (rhs. of Eq. (2.9)) is continuous but can kink for reaction rate coefficients that are unequal between the phases ($k_\alpha^I \neq k_\alpha^{II}$); see Fig. 2.2(b) and inset for average reaction rate of product B , \bar{s}_B . Average reaction rate \bar{s}_B can even initially increase before relaxing to thermodynamic equilibrium ($\bar{s}_B = 0$). This increase is a result of an initial very fast growth of phase I, which increases due to the fast formation of product B in phase I (Fig. 2.3(a)). The low internal energy of product B and a higher value of reaction rate coefficient facilitate its

higher production in phase I.

The kink of the average reaction rate \bar{s}_B at the onset of phase separation implies a jump in the acceleration of the chemical reaction, $\dot{\bar{s}}_B$ (Fig. 2.3(b)). In other words, as coexisting phases form, there is a drastic change in the average reaction rate of the system. This change reflects the effect of phase separation on the kinetics of chemical reactions.

2.3 Bimolecular chemical reactions in coexisting phases

As a further example of a chemically reactive system at phase equilibrium, we study a four-component system that contains three reactive solutes $i = A, B, C$ and a non-reactive solvent (0). In this example, the solutes undergo a bimolecular chemical reaction,



which conserves volume (molecular volumes, $(-\nu_A - \nu_B + \nu_C = 0)$, such that $r_{A/B} = 1$ and $r_C = 2$). For such a bimolecular chemical reaction in a four-component incompressible mixture, there exist two conserved quantities ($L = 3, R = 1$) (as explained in Sec. 1.3). Each conserved quantity is represented by a plane in a three-dimensional phase diagram spanned by the volume fractions of the reactive solute components A, B, C . The three conserved quantities are $\psi_1 = (\phi_A + \phi_B + \phi_C)$ and $\psi_2 = (\phi_A - \phi_B)$ and the intersection of the planes corresponding to conserved quantities ψ_1 and ψ_2 yields a line in the phase diagram.

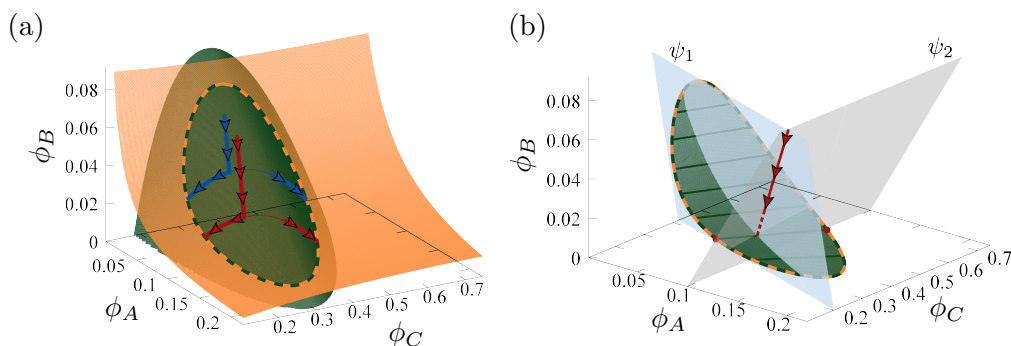


Fig. 2.4: Mass action kinetics of a bimolecular reaction at phase equilibrium.

(a) Phase equilibrium and chemical equilibrium are represented by two surfaces (green and orange, respectively). The closed line given by the intersection of these two surfaces depicts the thermodynamic equilibria states (dashed green line). The solid blue and red lines correspond to the trajectories of two systems with different values of conserved quantities (see (b)). We have chosen $\psi_1 = 0.42$ with $\psi_2 = 0.05$ for the blue trajectory and $\psi_2 = 0.1$ for the red trajectory. (b) Two planes of conserved quantities defined by ψ_1 (light blue plane) and ψ_2 (gray plane) intersect to uniquely define a line (solid red as in (a)) along which the trajectory of the average volume fractions progresses during kinetics. At the intersection of this unique line with the manifold of thermodynamic equilibrium, the compositions in each phase (red dots) are also uniquely selected. Parameters are listed in the L.O.F section.

The chemical kinetics of a bimolecular reaction at phase equilibrium can be depicted as a chemical trajectory in the three-dimensional phase diagram. Figure 2.4(a) shows two

chemical trajectories corresponding to systems with two different values of conserved quantities. For both cases, the kinetics of the average composition follows the intersection of the respective conserved planes, ψ_1 and ψ_2 , which is illustrated for one initial condition in Fig. 2.4(b). As phase separation occurs, the volume fractions in each phase move along the binodal surface (green). The chemical kinetics stop when the volume fractions in the coexisting phases reach the thermodynamic equilibrium (green-orange dashed line in Fig. 2.4(a-b)). The thermodynamic equilibria lie on a closed line is given by the intersection between the binodal surface and the chemical equilibrium surface with the condition, $\bar{\mu}_A + \bar{\mu}_B = \bar{\mu}_C$. The steady state values of the product can differ since the thermodynamic equilibrium state depends on the conserved quantities (shown by the tie lines in Fig. 2.4(b)).

2.4 Chemical reactions maintained away from chemical equilibrium

Chemical reactions can also be maintained away from thermodynamic equilibrium. This is common in living cells, where the consumption of biochemical fuel like ATP or GTP chemically drives biochemical reactions. Maintaining reactions away from chemical equilibrium can lead to non-equilibrium steady states (NESS) with non-vanishing diffusive exchange rates between the phases.

Here we consider systems at phase equilibrium that are maintained away from chemical equilibrium by fuel components which provide an external reaction free energy for the chemical reaction α , $\Delta\tilde{\mu}_\alpha = \tilde{\mu}_\alpha^- - \tilde{\mu}_\alpha^+$, which stems from differences in the external reaction free energies in the respective phases, $\tilde{\mu}_\alpha^{+/-}$. The reaction free energy in Eq. (1.25) thus reads

$$\Delta\mu_\alpha = \sum_{i=1}^L \sigma_{i\alpha} \bar{\mu}_i + \Delta\tilde{\mu}_\alpha, \quad (2.12)$$

which can again be written as the difference between forward (+) and backward (-) reaction free energies

$$\mu_\alpha^\pm = \sum_{i=1}^L \sigma_{i\alpha}^\pm \bar{\mu}_i + \tilde{\mu}_\alpha^\pm. \quad (2.13)$$

In certain cases, these systems reach an effective equilibrium state even if $\Delta\tilde{\mu}_\alpha \neq 0$ and Eq. (2.12) can be recast in the form of Eq. (1.25): (i) $\Delta\tilde{\mu}_\alpha = \sum_{i=1}^L \sigma_{i\alpha} c_i$, where c_i are constants and the system can phase-separate; (ii) the chemical potential shifts $c_i(\phi_i)$ corresponding to $\Delta\tilde{\mu}_\alpha$ depend on composition but the system is spatially homogeneous (no phase separation). Case (i) maintains thermodynamic consistency of phase and effective chemical equilibria by defining effective reference chemical potentials $\bar{\mu}_i^0$ in Eq.(1.12), which do not affect phase equilibrium.

In contrast, case (ii) does not have phase equilibrium but maintains reaction networks, driving just one reaction and approaching effective chemical equilibrium [70, 71]. If these conditions are not satisfied, the system cannot reach a thermodynamic equilibrium.

Here, we focus on systems with phase/composition dependent $\Delta\tilde{\mu}_\alpha$ in the presence of coexisting phases. Thus, neither case (i) nor case (ii) applies, and it is truly out-of-equilibrium.

Under these circumstances, the intersections between the binodal manifold with the effective chemical equilibrium manifold, $\Delta\tilde{\mu}_\alpha = 0$ (e.g., yellow and red lines in Fig. 2.5(a)), will not be connected by a tie line. Therefore, there can be non-equilibrium steady states, where $d\phi_i^{I/II}/dt = 0$ and $dV^{I/II}/dt = 0$ with non-zero reaction rates $s_i^{I/II}$ and diffusive exchange rates $j_i^{I/II}$ between the coexisting phases.

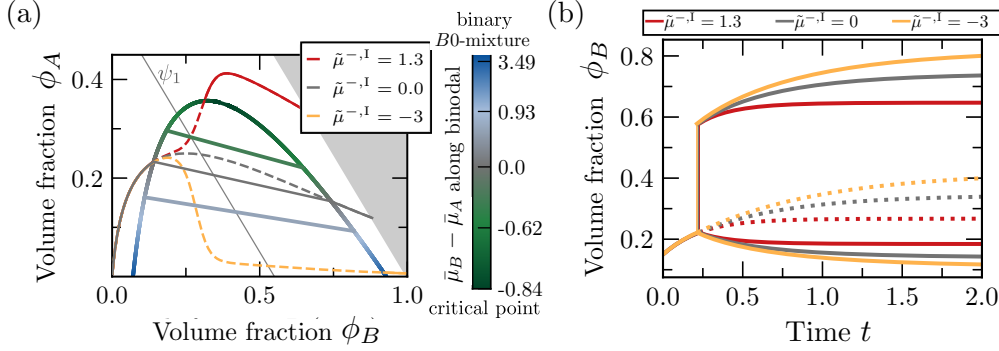


Fig. 2.5: Unimolecular chemical reaction maintained away from chemical equilibrium.(a) Depending on the value of the chemostat potential $\tilde{\mu}^{-,I}$, different coexisting phases are selected (green tie line for $\tilde{\mu}^{-,I} = 1.3$ and light blue-gray line for $\tilde{\mu}^{-,I} = -3$). The color bar represents the chemical potential difference between the components B and A along the binodal line, where the lower/upper bound corresponds to the critical point/binary $B0$ mixture. (b) Chemical trajectories for product B , where solid and dotted lines correspond to volume fractions in phase I/II and averages, respectively. Chemical kinetics and non-equilibrium steady states vary with the value of the chemostat potential, $\tilde{\mu}^{-,I}$. Parameters are listed in the L.O.F section.

A measure of the deviation of the chemical reaction α from thermodynamic equilibrium is the reaction free energy in the non-equilibrium steady state,

$$\Delta\mu_\alpha^{\text{NESS}} \equiv \sum_{i=0}^M \sigma_{i\alpha} \mu_i^{\text{NESS}}, \quad (2.14)$$

where μ_i^{NESS} are steady state chemical potentials. Since $\bar{\mu}_i$ are identical in the two phases due to phase equilibrium, the non-equilibrium reaction free energy,

$$\Delta\mu_\alpha^{\text{NESS}}/k_B T = \log \left(\frac{k_\alpha^I V^I \exp\left(\frac{\tilde{\mu}_\alpha^{+,I}}{k_B T}\right) + k_\alpha^{\text{II}} V^{\text{II}} \exp\left(\frac{\tilde{\mu}_\alpha^{+,II}}{k_B T}\right)}{k_\alpha^I V^I \exp\left(\frac{\tilde{\mu}_\alpha^{-,I}}{k_B T}\right) + k_\alpha^{\text{II}} V^{\text{II}} \exp\left(\frac{\tilde{\mu}_\alpha^{-,II}}{k_B T}\right)} \right), \quad (2.15)$$

is phase-independent. Equation (2.15) results from the balance of reaction and diffusive exchange rates $s_i^{I/II} = j_i^{I/II}$, which corresponds to the steady state condition of Eq. (2.3a) together with $dV^{I/II}/dt = 0$. The non-equilibrium reaction free energies, $\Delta\mu_\alpha^{\text{NESS}}$ can be interpreted as susceptibilities of the system to external reaction free energies $\tilde{\mu}_\alpha^{\pm,I/II}$. The values of the non-equilibrium reaction free energies are dependent on the reaction rate coefficients $k_\alpha^{I/II}$ and the phase volumes at steady state, $V^{I/II}$. To illustrate the kinetics of chemical reactions and steady states that are maintained away from chemical equilibrium but are at phase equilibrium, we study the same unimolecular reaction in a ternary mixture as in Sec. (2.2). To maintain the reaction away from chemical equilib-

rium, we introduce a non-zero backward external reaction free energy $\tilde{\mu}^{-,I}$. For simplicity, the other reaction free energies $\tilde{\mu}^{\pm,II}$ and $\tilde{\mu}^{+,I}$ are chosen to be zero. Therefore, the effective chemical equilibrium line, $\Delta\mu = 0$, is only affected in phase I (solid red and yellow lines compared to the gray line in Fig. 2.5(a)). For a single reaction, however, a non-equilibrium steady state can only be reached in systems with coexisting phases.

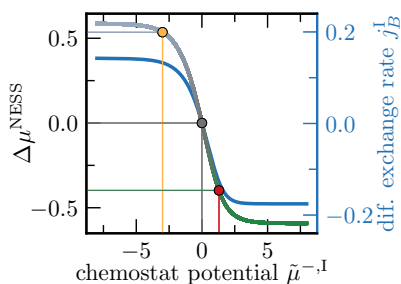


Fig. 2.6: Measure of non-equilibrium free energy. More the chemostat potential, $\tilde{\mu}^{-,I}$, deviates from zero, the more the system is maintained away from thermodynamic equilibrium. The non-equilibrium steady state is characterized by the non-equilibrium reaction free energy, $\Delta\mu^{\text{NESS}}$. The gray dot corresponds to the reference system at thermodynamic equilibrium, while the red and orange dots represent the two non-equilibrium steady states depicted in Fig. 2.5(a,b). Diffusive exchange rate j_B^I at the NESS (blue curve with the corresponding axis at the r.h.s.) is nonzero as the system is maintained away from thermodynamic equilibrium via the chemostat potential $\tilde{\mu}^{\text{flai},I}$. Results here and in Figs. 2.5(a,b) are obtained for $\psi_1 = 0.55$. Parameters are listed in the L.O.F section.

I. This trend is opposed by a decrease in the volume of phase I, therefore leading to the plateau for $\tilde{\mu}^{-,I}$. Consistent with this, the value of the plateau of $\Delta\mu^{\text{NESS}}$ is determined by the volume of phase I, which is in turn set by the conserved quantity ψ_1 . Specifically, the plateau value corresponds to the intersection of the line of conserved quantity ψ_1 (thin gray line) and the binodal line; see Fig. 2.5(a). In contrast, small and negative values of $\tilde{\mu}^{-,I}$ favor the conversion from component A to B in phase I. The full conversion is not possible since chemical reactions are only maintained away from chemical equilibrium in phase I, and thus the volume of phase I limits the selection of coexisting, non-equilibrium steady states.

For such systems, an important finding is that by choosing different values of the external reaction free energy $\tilde{\mu}^{-,I}$, the chemical kinetics changes, and the system relaxes to different non-equilibrium steady states. For each value of $\tilde{\mu}^{-,I}$, such steady states have specific compositions in the coexisting phases indicating that the chemical driving can select distinct states of the chemically reactive system. (solid green and light blue, respectively, in Fig. 2.5(a-b)). Moreover, the chemical trajectories of the volume fractions in each phase (solid lines) and the average volume fractions (dotted lines) change when varying the external reaction free energy $\tilde{\mu}^{-,I}$; see Fig. 2.5(b). In particular, the jump of the average acceleration \dot{s}_i is also affected by the external reaction free energy (not shown).

The reaction free energy in the non-equilibrium steady state $\Delta\mu^{\text{NESS}}$ is used to characterise how much the considered system deviates from thermodynamic equilibrium for a given value of the backward external reaction free energy $\tilde{\mu}^{-,I}$. Around thermodynamic equilibrium, $\Delta\mu^{\text{NESS}}(\tilde{\mu}^{-,I})$ varies linearly, while for large deviations, $\Delta\mu^{\text{NESS}}$ saturates at two plateaus depending on the sign of the backward external reaction free energy $\tilde{\mu}^{-,I}$ (Fig. 2.6). In particular, large and positive $\tilde{\mu}^{-,I}$ favor the conversion from component B to A in phase

For chemically driven systems, the phase volumes are strongly influenced by an external supply of reaction free energy. This property is distinct to chemically driven systems since, at thermodynamic equilibrium, the phase volumes are solely determined by the conserved quantity. In particular, a ternary mixture with one chemical reaction at thermodynamic equilibrium becomes an effective binary mixture of two conserved quantities. As a result, varying these conserved quantities solely changes the phase volumes (Fig. 1.11(a)). In contrast, for a chemically driven system, changing the conserved quantities also affects phase composition.

2.4.1 Tie-line selecting curve

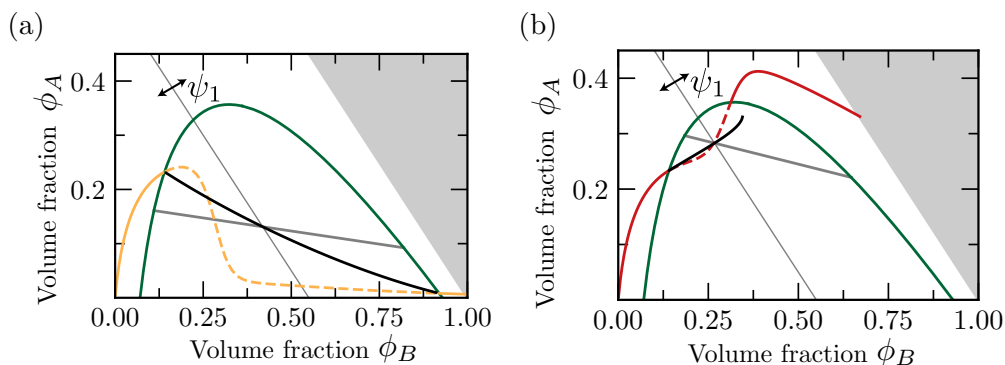


Fig. 2.7: Selection of tie line for varying conserved quantity. In (a) and (b), we show the two cases of the mono-nodal considered, where the yellow mono-nodal in (a) corresponds to $\tilde{\mu}^{-I} = -3$, while the red mono-nodal in (b) corresponds to $\tilde{\mu}^{-I} = 1.3$. For each value of the conserved quantity ψ_1 , a specific tie-line is selected, which is the tie-line that contains the intersection point between the conservation line ψ_1 (thin grey) and the line of average volume fractions described by the steady state condition, $d\phi^{I/II}/dt = 0$ and $dV^{I/II}/dt = 0$ (thick black). Here the conservation line is shown for $\psi_1 = 0.55$. The average volume fractions at steady state (thick black line) are drawn for all values of ψ_1 for which a demixed NESS exists. For those, the range of ψ_1 is constrained between the points at which the mono-nodal crosses the binodal. Parameters are listed in the L.O.F section.

For systems maintained away from equilibrium, the composition at NESS depends on the volumes of the coexisting phases $V^{I/II}$, unlike the case of thermodynamic equilibrium (see Eq. (2.15)). Therefore, in our considered example of a ternary system with a non-equilibrium chemical reaction, the composition at the non-equilibrium steady state depends on the conserved quantity ψ_1 . Thus, the tie-line corresponding to the NESS also varies with ψ_1 (Fig. 2.7) and the tie-line selecting curve for a choice of $\tilde{\mu}^{-I}$ allows selection of the tie-line at NESS where it intersects the choice of conserved quantity ψ_1 . It is obtained by simultaneously solving phase equilibrium conditions, material conservation, and Eq. (2.15). As a measure of the deviation to thermodynamic equilibrium, we determined the non-equilibrium reaction free energy (r.f.e) $\Delta\mu^{\text{NESS}}$ as a function of the conserved quantity ψ_1 (Fig. 2.8). Due to the external supply of free energy via the chemostat potential in phase I, $\tilde{\mu}^{-I}$, the absolute value of the non-equilibrium reaction free energy $\Delta\mu^{\text{NESS}}$ increases for larger values of the conserved quantity. Increasing ψ_1 , the volume of phase I, V^I grows. $\Delta\mu^{\text{NESS}}$ is positive when A is favored over B ($\tilde{\mu}^{-I} > 0$) by the non-equilibrium

reaction, and vice versa.

2.5 Summary and Discussion

In this chapter, we developed a theory of the chemical kinetics in phase-separated mixtures at phase equilibrium. For simplicity, we considered homogeneous phases, applying to cases where chemical reactions are slow compared to the phase separation kinetics and including systems where chemical reactions are rate limiting, which is typical of biological enzymes [67].

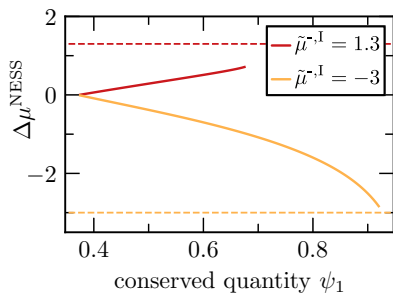


Fig. 2.8: Measure of non-equilibrium free energy. We show the non-equilibrium reaction free energy $\Delta\mu^{\text{NESS}}$ as a function of the conserved quantity ψ_1 for two values of the chemostat potential $\tilde{\mu}^{-,I}$ considered in Fig. 2.7. The chemostat potential values (dashed lines) are limiting $\Delta\mu^{\text{NESS}}$, correspondingly. Parameters are listed in the L.O.F section.

Furthermore, the kinetics of reactions approaching chemical equilibrium also differs between phase-separated and the corresponding well-mixed system. We showed that conservation laws play an important role in phase-separated systems. Quantities conserved by the reactions define manifolds in composition space to which average compositions are confined, while the volume fractions in the phases remain confined to the binodal manifold. We clarified that the increased concentration of reactants in a condensed phase does not by itself lead to increased reaction rates. Rather, if the coexisting phases are at phase equilibrium, the reaction rates $s_i^{I/II}$ of component i in each phase can only differ due to different reaction rate coefficients $k_\alpha^{I/II}$. The speed-up or slow-down of reactions is solely determined by the reaction rate coefficients in each phase, which can also decrease upon condensation. These insights might be relevant to explain recent observations in coacervate emulsions with enzymatic reactions [66, 33, 72, 73]. Another important insight of our work to determine the reaction rates $s_i^{I/II}$ of component i , the diffusive exchange rate between the phases and the changes in phase volumes must be considered. To highlight this point, we note that the effect of phase separation on chemical reactions in two coexisting phases cannot be inferred from studying reactions in the two phases when they are isolated. We also discussed chemical reactions at phase equilibrium but maintained away from chemical equilibrium via an external supply of free energy via a chemical fuel. We showed that the steady state volume fractions in the two phases depend on the external reaction free energy. Thus, controlling the external reaction free energy supply can be used to select distinct compositions of coexisting phases. For systems maintained away from chemical equilibrium, the reaction rates $s_i^{I/II}$ can be phase-dependent due to the supply of external free energy, which can differ between the phases, in addition to phase-dependent reaction rate coefficients $k_\alpha^{I/II}$. Thus, for such driven systems, reaction rates in the two phases can be controlled externally, even allowing opposite net directions of chemical reactions between the phases.

Chapter 3

Chemical reactions of dilute clients in phase-separated compartments

"Optimality is the study of superlatives. Nowadays, optimality plays two distinct but interrelated roles in science: (1) in pure science, its impact is primarily analytic or explanatory; we use it to characterize the way in which a natural process does occur, out of all the ways it could occur; and (2) in applied science (technology or engineering in the broadest sense), we use it to decide how we should do something, out of all the possible ways in which we could do it (here the emphasis is primarily on design or synthesis)."

– Robert Rosen, *Essays on Life Itself*

It is known that phase separation is organized by multivalent interactions among disordered proteins and RNA (also known as scaffolds) [19] that build up these compartments, also referred to as the condensed phase as opposed to the dilute phase. These compartments provide different physicochemical environments for the occurrence of various chemical reactions, which carry out particular functions for the smooth functioning of the cell. Some examples include ribosome biogenesis in nucleoli [74] and mRNA splicing in nuclear speckles [75, 76]. It cannot be claimed with certainty that all such processes are optimized in the cell. However, when one reconstitutes such compartmentalized reactions *in vitro*, there is more control on parameters while designing the system that can be tuned to optimality. In the cell, the scaffold component is expected to be present at a more significant concentration than the reactants (clients) [19, 77] that participate in the chemical reactions. So to a reasonable extent, one can safely assume that the clients are dilute. They usually do not affect the phase-separated compartment formed in the cell in terms of modifying the compartment phase volume or the scaffold concentration in the respective phases. They merely read out the concentration profile of the scaffold in the system and, depending on their interaction strength with the scaffold and solvent, partition inside or outside the condensed phase composed of the scaffold.

The objective of this chapter involves decoding the physicochemical parameters that can control (bio)chemical reactions in phase-separated compartments (drops), understanding the extent to which such reactions can be controlled as compared to a system where the reaction proceeds in the absence of compartments, and defining observables for such reactions which can then be optimized by tuning these parameters. The reason for calling the reactions (bio)chemical, is because we assume that any true biochemical reaction in a cell

can be decomposed into simpler steps involving either two-state transition, bimolecular reaction, or nucleation that can consume fuel (Fig. 3.1(b)) (however, throughout the chapter we skip the use of (bio)). This framework will be adapted for later implementation in chapter 5. This study was performed in collaboration with Jonathan Bauermann, Tyler Harmon, and Thomas Michaels.

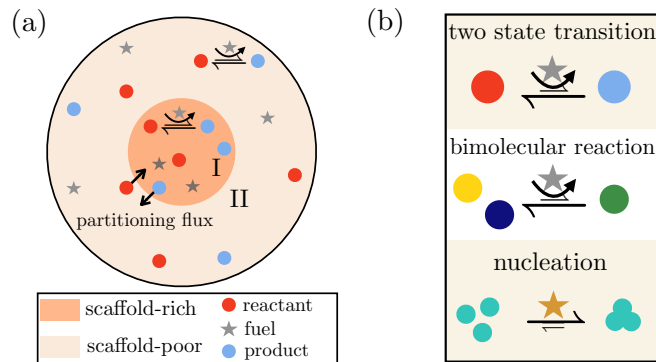


Fig. 3.1: Schematic representation of a system with dilute reactive clients in presence of a drop. (a) The non-dilute scaffold component for a specific volume fraction forms a spherical drop. The dilute chemical clients can partition into the drop and can undergo chemical reactions in both phases, I and II. In addition, clients are exchanged between two domains via diffusion to maintain partition equilibrium Eq. (3.5). (b) Overview of the different (bio)chemical reactions studied in this chapter both in the presence and absence of a drop. These reactions are driven out of equilibrium due to the continuous consumption of energy via fuel-driven pathways (star markers).

3.1 Thermodynamics of a multicomponent mixture of scaffold and clients

We consider here an $(L + 2)$ component incompressible mixture composed of the non-reactive solvent (0), non-reactive scaffold (1) (only one scaffold, for simplicity but can be easily generalized for $(i : i > 1)$ number of scaffold components), and L reactive dilute clients. The non-dilute theory of multicomponent mixtures is described in Sec. (1.2). The non-approximated equilibrium volume fractions of all components are obtained by simultaneously solving Eqs. (1.17), and the phase fractions are additionally calculated by including the conservation of all components $i = 1, \dots, (L + 1)$,

$$\frac{V^I}{V} = \frac{\bar{\phi}_i - \phi_i^{\text{II}}}{\phi_i^{\text{I}} - \phi_i^{\text{II}}}, \quad (3.1)$$

where $\bar{\phi}_i$ is the average volume fraction of i -th component.

Component	Diluteness	Reactivity
Solvent (0)	No	No
Scaffold (1)	No	No
Clients ($i = 2, \dots, (L + 1)$)	Yes	Yes

Table 3.1 Classification of components based on composition and role.

3.1.1 Phase equilibrium conditions: Dilute client limit

The dilute limit is defined as the zeroth order of the expansion of certain thermodynamic variables like exchange activity coefficients, equilibrium volume fractions ($\bar{\gamma}_i, \{\phi_i^{I/II}\}$) and phase fraction (V^I/V) in the average volume fraction of the clients $\{\bar{\phi}_i\}$. Therefore, the small parameter to expand around is the variable $\{\bar{\phi}_i\} = 0; i = 2, \dots, (L + 1)$. Its validity is studied in detail in Appendix. C.

Firstly, the exchange activity coefficient of all components can be expanded as,

$$\bar{\gamma}_i = \bar{\gamma}_i(\bar{\phi}_1, \{\bar{\phi}_i\} = 0) + \mathcal{O}(\bar{\phi}_i) + .. \quad (3.2)$$

following which truncating after zeroth order, we obtain in the dilute limit,

$$\bar{\gamma}_i = \frac{1}{(1 - \bar{\phi}_1)^{r_i}} \exp \left[r_i (\chi_{1i} - \chi_{0i} - \chi_{01}) \bar{\phi}_1 \right]. \quad (3.3)$$

For the scaffold, the above expression reduces to,

$$\bar{\gamma}_1 = \frac{1}{(1 - \bar{\phi}_1)^{r_1}} \exp \left[-2r_1 \chi_{01} \bar{\phi}_1 \right]. \quad (3.4)$$

This thermodynamic quantity for the scaffold is independent of the client volume fractions, whereas, for the dilute clients, following Eq. (3.3), the exchange activity coefficient, $\bar{\gamma}_i$ is a constant depending on the scaffold volume fraction $\bar{\phi}_1$ alone. Following from the definition of the partition coefficient as in Eq. (1.20), it follows that in the dilute limit, it is a constant for the clients (Fig. 3.2),

$$P_i = \left(\frac{1 - \phi_1^{0,I}}{1 - \phi_1^{0,II}} \right)^{r_i} \exp [r_i (\phi_1^{0,I} - \phi_1^{0,II}) (\chi_{01} + \chi_{0i} - \chi_{1i})], \quad (3.5)$$

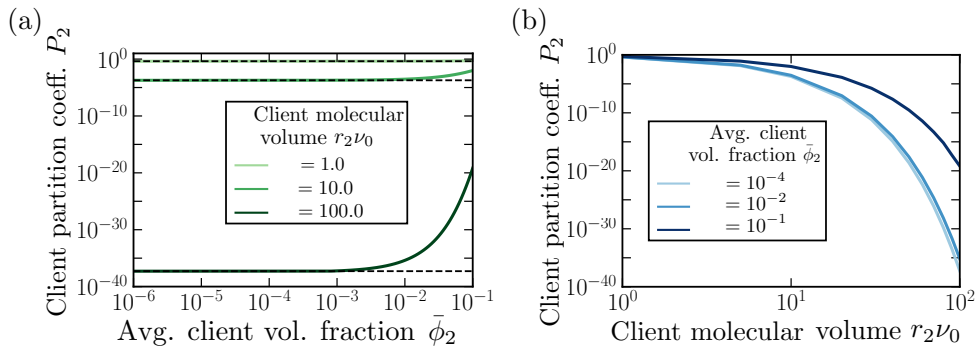


Fig. 3.2: Partition coefficient of clients: Dilute limit. In a ternary mixture with one client ($i = 2$) component, we study how client partition coefficient P_2 (a) varies with $\bar{\phi}_2$ with the exact solution (solid green shade lines for varying client molecular volume $r_2\nu_0$) along with constant dilute approximation (black dashed using Eq. (3.5)), (b) varies with its $r_2\nu_0$ for different $\bar{\phi}_i$. Parameters are listed in the L.O.F section.

where we see an exponential dependence on the relative molecular volume parameter of

the client r_i . Similarly, for the scaffold, the partition coefficient is,

$$P_1 = \left(\frac{1 - \phi_1^{0,I}}{1 - \phi_1^{0,II}} \right)^{r_1} \exp[2r_1 \chi_{01} (\phi_1^{0,I} - \phi_1^{0,II})], \quad (3.6)$$

where $\phi_1^{0,I/II}$ are the equilibrium volume fractions of the scaffold at the dilute limit of clients (in an effective binary mixture; derivation shown below). The partition coefficient $P_i > 1$ implies that the i -th component partitions preferentially in the drop phase (I) and vice versa.

We express the equilibrium volume fractions in the phases and phase fractions as functions of the average volume fractions of all components as,

$$\begin{aligned} \phi_i^{I/II} &= h_i^{I/II}(\bar{\phi}_1, \bar{\phi}_2, \dots, \bar{\phi}_{L+1}), \\ \frac{V^I}{V} &= g(\bar{\phi}_1, \bar{\phi}_2, \dots, \bar{\phi}_{L+1}). \end{aligned} \quad (3.7)$$

The approximations to the scaffold ($i = 1$) equilibrium volume fractions can be written as,

$$\phi_1^{I/II} = \phi_1^{0,I/II} + \sum_{i=2}^{L+1} \left. \frac{\partial h_1^{I/II}}{\partial \bar{\phi}_i} \right|_{\{\bar{\phi}_i\}=0} \bar{\phi}_i + \mathcal{O}(\bar{\phi}_i)^2 + \dots \quad (3.8a)$$

where the linear coefficients of the first order corrections are obtained using the partition coefficient (Eq. (3.5)) and phase fraction (calculated subsequently Eq. (3.8h)),

$$\begin{aligned} \left. \frac{\partial h_1^I}{\partial \bar{\phi}_i} \right|_{\{\bar{\phi}_i\}=0} &= a_i^I P_i \zeta_i, \\ \left. \frac{\partial h_1^{II}}{\partial \bar{\phi}_i} \right|_{\{\bar{\phi}_i\}=0} &= a_i^{II} \zeta_i, \end{aligned} \quad (3.8b)$$

where ζ_i is introduced as the partitioning degree,

$$\zeta_i = \frac{1}{1 + (P_i - 1)V^I/V}, \quad (3.8c)$$

and $a_i^{I/II}$ are expressed as (detailed calculation in Appendix. C),

$$a_i^I = -\phi_1^{0,I} \frac{1 + \left(\chi_{1i} - \chi_{0i} - \chi_{01} + \frac{1-1/P_i}{r_i(\phi_1^{0,I} - \phi_1^{0,II})} \right) (1 - \phi_1^{0,I})}{\frac{1-\phi_1^{0,I}}{r_1} + \phi_1^{0,I} - 2\chi_{01}\phi_1^{0,I}(1 - \phi_1^{0,I})}, \quad (3.8d)$$

$$a_i^{II} = -\phi_1^{0,II} \frac{1 + \left(\chi_{1i} - \chi_{0i} - \chi_{01} + \frac{P_i-1}{r_i(\phi_1^{0,I} - \phi_1^{0,II})} \right) (1 - \phi_1^{0,II})}{\frac{1-\phi_1^{0,II}}{r_1} + \phi_1^{0,II} - 2\chi_{01}\phi_1^{0,II}(1 - \phi_1^{0,II})}. \quad (3.8e)$$

According to the definition of dilute limit above, we neglect first-order corrections and obtain,

$$\phi_1^{I/II} = \phi_1^{0,I/II}. \quad (3.8f)$$

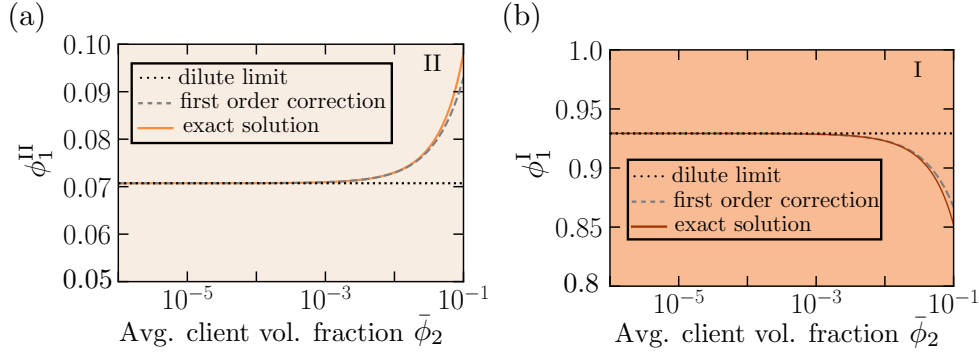


Fig. 3.3: Scaffold equilibrium volume fraction: Dilute limit. In a ternary mixture with one client ($i = 2$), we study how the scaffold eq. volume fractions $\phi_1^{I/II}$ are affected in the respective phases (solid lines in shades of orange represent the exact solution, gray dashed lines represent the linear corrections using Eq.(3.8)(a-d), and gray dotted lines using Eq.(3.8f)). Parameters are listed in the L.O.F section.

Similarly, the approximation to the phase fraction is expressed as,

$$\frac{V^I}{V} = g(\bar{\phi}_1^0, \{\bar{\phi}_i\} = 0) + \sum_{i=2}^{L+1} \left. \frac{\partial g}{\partial \bar{\phi}_i} \right|_{\{\bar{\phi}_i\}=0} \bar{\phi}_i + \mathcal{O}(\bar{\phi}_i)^2 + \dots, \quad (3.8g)$$

where applying the definition of the dilute limit and using Eq.(3.8f), we obtain,

$$\frac{V^I}{V} = \frac{\bar{\phi}_1 - \phi_1^{II}}{\phi_1^I - \phi_1^{II}}. \quad (3.8h)$$

The approximation to the client equilibrium volume fractions is expressed as (no zeroth order contribution because the solution is known when clients are absent in the system ($\{\bar{\phi}_i\} = 0$), i.e., binary system),

$$\phi_i^{I/II} = \sum_{j=2}^{L+1} \left. \frac{\partial h_i^{I/II}}{\partial \bar{\phi}_j} \right|_{\{\bar{\phi}_i\}=0} \bar{\phi}_j + \frac{1}{2} \sum_{j,k=2}^{L+1} \left. \frac{\partial^2 h_i^{I/II}}{\partial \bar{\phi}_j \partial \bar{\phi}_k} \right|_{\substack{\bar{\phi}_j=0 \\ j \neq i}} \bar{\phi}_j \bar{\phi}_k + \mathcal{O}(\bar{\phi}_i)^3 + \dots \quad (3.8i)$$

Only client variables of the form (0/0) are well defined. Hence we re-arrange Eq.(3.8i) as,

$$\frac{\phi_i^{I/II}}{\bar{\phi}_i} = \frac{\partial h_i^{I/II}}{\partial \bar{\phi}_i} + \frac{1}{2} \sum_{j=2}^{L+1} \left. \frac{\partial^2 h_i^{I/II}}{\partial \bar{\phi}_i \partial \bar{\phi}_j} \right|_{\{\bar{\phi}_i\}=0} \bar{\phi}_j + \mathcal{O}(\bar{\phi}_i)^2 + \dots \quad (3.8j)$$

Similar to above, we neglect beyond zeroth order and obtain,

$$\frac{\phi_i^{I/II}}{\bar{\phi}_i} = \frac{\phi_i^{0,I/II}}{\bar{\phi}_i}, \quad (3.8k)$$

where we can obtain the client volume fractions in the respective phases using the conditions from Eqs. (3.1) and (3.5), which lead to the use of partitioning degree (Eq. (3.8c)) as,

$$\phi_i^I = P_i \zeta_i \bar{\phi}_i, \quad (3.9a)$$

$$\phi_i^{\text{II}} = \zeta_i \bar{\phi}_i. \quad (3.9b)$$

As the drop volume set by scaffold (Eq. (3.8h)) vanishes (i.e., $V^I/V \rightarrow 0$), $\zeta_i \rightarrow 1$ and $\phi_i^{\text{II}} \rightarrow \bar{\phi}_i$. The other limit of $V^I/V \rightarrow 1$ can be similarly calculated.

3.1.2 Relaxation dynamics to phase equilibrium: Dilute client limit

Continuum model

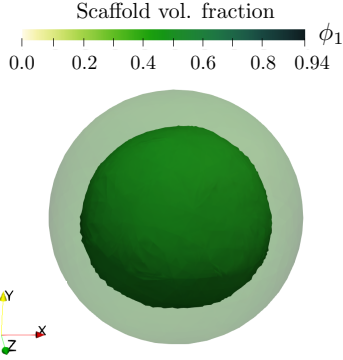


Fig. 3.4: Stationary profile for scaffold in spherical geometry. Solution of Eq. (3.11) modified Cahn-Hilliard equation in a binary system for interaction parameter $\chi_{01} = 3$. The numerical implementation is discussed in Appendix. B. Parameters are listed in the L.O.F section.

We recall the conservation equations discussed in subsection.(1.2.6). Firstly in the dilute limit of clients, the mobility matrix elements are as follows,

$$\begin{aligned} M_{11} &= m_{01}\phi_1(1 - \phi_1 - \sum_{i=2}^{L+1} \phi_i) + \sum_{\substack{k \neq 1 \\ k=2}}^{L+1} m_{1k}\phi_1\phi_k, \\ M_{1i} &= -m_{1i}\phi_i\phi_1, \\ M_{ii} &= m_{0i}\phi_i(1 - \phi_1) + m_{1i}\phi_i\phi_1, \\ M_{i1} &= -m_{1i}\phi_i\phi_1, \\ M_{ij} &= 0, \end{aligned} \quad (3.10)$$

where we neglected quadratic terms in dilute client volume fractions. We use the definition of diffusive fluxes, as in Eq. (1.22) and the exchange activity coefficient in the dilute limit as Eq. (3.4).

In the continuum model, the evolution of the scaffold volume fraction is given by (full derivation in App. D),

$$\partial_t \phi_1(\mathbf{r}, t) = -\nabla \cdot \left\{ m_{01} \left[(1 + \phi_1(r_1 - 1) - 2r_1 \chi_{01} \phi_1(1 - \phi_1)) \nabla \phi_1 - \kappa_1 \nabla \nabla^2 \phi_1 \right] \right\}. \quad (3.11)$$

We observe that for the scaffold, this is essentially the modified Cahn-Hilliard equation for the free energy density of binary mixture (Eq. (1.7)) and is completely independent of the client volume fractions.

For the clients, it is essentially it is diffusion in a potential $(\nabla \phi_1)$ [61], along with higher-order gradient term that emerges since the scaffold (1) sets the interface width.

$$\begin{aligned} \partial_t \phi_i(\mathbf{r}, t) = \nabla \cdot & \left[\left[m_{0i}(r_i(\chi_{1i} - \chi_{0i} - \chi_{01}) + r_i) - m_{1i} \left(1 + \frac{(r_1 - r_i)\phi_1}{1 - \phi_1} - 2r_1\chi_{01}\phi_1 \right) \right] \phi_i \nabla \phi_1 \right. \\ & \left. + \left[m_{0i}(1 - \phi_1) + m_{1i}\phi_1 \right] \nabla \phi_i + m_{1i}\phi_i\phi_1\kappa_1 \nabla \nabla^2 \phi_1 \right]. \end{aligned} \quad (3.12)$$

Equations (3.11) and (3.12), together account for the approach of this system to phase equilibrium in the continuum model. Refer to Appendix C for the exact expressions for the diffusive fluxes, \mathbf{j}_i . Eq. (3.11) dictates the evolution of the scaffold. However, the dynamical equations for the clients depend on the scaffold.

Thin interface model

In the stationary and thin interface approximation of the scaffold, we neglect the terms proportional to $\nabla \phi_1$ and $\nabla^2 \phi_1$, because the volume fraction profile of the scaffold is homogeneous away from the interface. The scaffold volume fraction profile at equilibrium close to the critical point has a sigmoidal profile at the interface given by,

$$\phi_1^{\text{int}}(\mathbf{r}) = \phi_1 + \tanh \left(\sqrt{\frac{(\chi_{01} - 2)k_B T \nu_0 r_1}{\kappa_1}} \mathbf{r} \right), \quad (3.13)$$

where the interface length scale is $\lambda^{\text{int}} = \sqrt{\kappa_1 / (\chi_{01} - 2)k_B T \nu_0 r_1}$. The thin interface model assumes that $\kappa_1 \rightarrow 0$ and also that the scaffold equilibrates. (allowing the interface length scale, λ^{int} to be negligible in comparison to other relevant length scales like the radius of drop R_d or system radius R). Each of the clients follows a diffusion equation in each of the phases I/II,

$$\partial_t \phi_i(\mathbf{r}, t) = D_i^{\text{I/II}} \nabla^2 \phi_i(\mathbf{r}, t), \quad (3.14a)$$

where index i represents the individual clients in the system, and s_i is the chemical flux for the i -th client, which is, in general, a function of the fuel volume fraction in the respective phase and other client volume fractions.

$$D_i^{\text{I/II}} = \begin{cases} m_{i0}(1 - \phi_1^{\text{I}}) + m_{i1}\phi_1^{\text{I}} & \text{for } \mathbf{r} \text{ in phase I,} \\ m_{i0}(1 - \phi_1^{\text{II}}) + m_{i1}\phi_1^{\text{II}} & \text{for } \mathbf{r} \text{ in phase II,} \end{cases} \quad (3.14b)$$

denotes the diffusion constant of each dilute client in the respective phase. The diffusion constant usually depends on the scaffold volume fraction in the respective phase, as seen from Eqs. (3.12) having applied the stationary condition and thin interface limit.

Phase coexistence leads to specific boundary conditions for the clients right inside and outside of the interface between the phases (Fig. 3.4a). For a single, spherical drop of radius R_d in a radially symmetrical, spherical domain of diameter $2R$ ($\mathbf{r} = (r, \varphi, \theta)$ in spherical coordinates), the boundary conditions for Eq. (3.14a) are as follows:

- The flux across the interface instead of radial flux, $\mathbf{e}_r \cdot \mathbf{j}_i$, right inside ($r = R_{d,-}$)

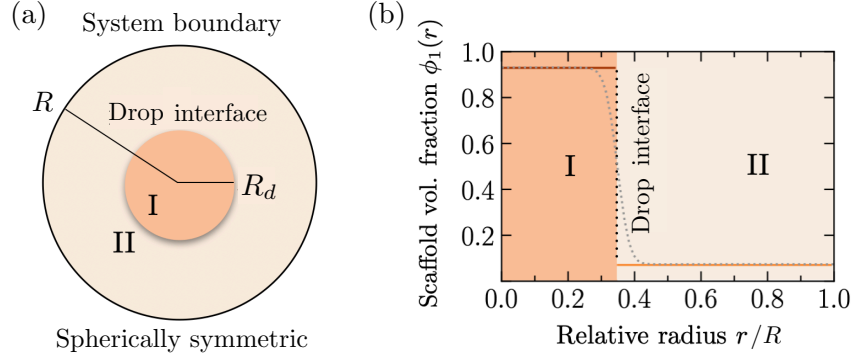


Fig. 3.5: Schematic representation of the model geometry. (a) Spherical drop phase of radius R_d , rich in scaffold components (I) coexists with scaffold-poor phase (II) in a spherical system of radius R . (b) Stationary spatial profile of the scaffold $\phi_1(r)$ in the dilute approximation of clients for the continuum model (grey dotted) and thin interface model (solid orange). Distance from the drop's center is measured using the relative radius r/R . Parameters are listed in the L.O.F section.

and outside ($r = R_{d,+}$) of the interface is equal,

$$\mathbf{e}_r \cdot \mathbf{j}_i|_{r=R_{d,-}} = \mathbf{e}_r \cdot \mathbf{j}_i|_{r=R_{d,+}}, \quad (3.14c)$$

where $\mathbf{j}_i = -\mathbf{e}_r D_i^\alpha \partial_r \phi_i$ is the flux and \mathbf{e}_r denotes the radial unit vector.

- The fraction of the client volume fractions right inside and outside of the interface satisfy the partition coefficient,

$$P_i = \frac{\phi_i|_{r=R_{d,-}}}{\phi_i|_{r=R_{d,+}}}, \quad (3.14d)$$

which is determined by the interaction strength of clients with scaffold and solvent components, as well as the degree of scaffold phase separation.

- All clients obey a no-flux boundary condition at the system boundary,

$$\mathbf{e}_r \cdot \mathbf{j}_i|_{r=R} = 0. \quad (3.14e)$$

- In the center of the spherical drop, the flux vanishes for all clients,

$$\mathbf{e}_r \cdot \mathbf{j}_i|_{r=0} = 0. \quad (3.14f)$$

3.1.3 Chemical equilibrium conditions: Dilute client limit

In subsection. (3.1.1), we obtained the expression for the exchange activity coefficients for clients (Eq. (3.3)). To study chemical equilibrium, we only focus on clients as they are the only reactive components. Assuming the scaffold and solvent are not varying, being non-reactive and stationary, we can use the definition of equilibrium reaction coefficient

in Eq. (1.27) to show that,

$$K_\alpha = \prod_{i=2}^{L+1} \bar{\gamma}_i(\phi_1)^{-\sigma_{i\alpha}} \exp\left(-\frac{\sigma_{i\alpha}\bar{\mu}_i^0}{k_B T}\right). \quad (3.15)$$

K_α is only dependent on scaffold volume fraction, which is fixed and, therefore, in this case, they are referred to as equilibrium reaction constants.

3.1.4 Relaxation dynamics to chemical equilibrium: Dilute client limit

For the reactive dilute clients, the reaction rates s_i , defined in Eq. (2.6), are reminiscent of the dilute mass-action kinetics we are familiar with (Eq. (1.35)), given that higher-order interactions are non-existent between clients. However, the only difference to the case discussed in subsection. (1.3.2) is that s_i depends on the constant scaffold volume fraction ϕ_1 , through exchange activity coefficients obtained in Eq. (3.3). The chemical reaction force H_α defined in Eq. (2.7), used to obtain s_i can be simplified as,

$$H_\alpha = \prod_{i=2}^{L+1} \left(e^{\frac{\bar{\mu}_i^0}{k_B T}} \bar{\gamma}_i(\phi_1) \phi_i \right)^{\sigma_{i\alpha}^+} - \prod_{i=2}^{L+1} \left(e^{\frac{\bar{\mu}_i^0}{k_B T}} \bar{\gamma}_i(\phi_1) \phi_i \right)^{\sigma_{i\alpha}^-}, \quad (3.16)$$

where $\bar{\gamma}_i(\phi_1)$ is the constant exchange activity coefficient of client i as defined in Eq. (3.3). We demonstrate this with the simple unimolecular ($A \rightleftharpoons B$) reaction example,

$$\begin{aligned} \frac{d}{dt}\phi_B(t) &= -\frac{d}{dt}\phi_A(t) \\ &= k \left[\exp\left(\frac{\bar{\mu}_A^0}{k_B T}\right) \frac{\phi_A(t)}{(1-\phi_1)^{r_A}} \exp(r_A\phi_1(\Delta\chi_A - \chi_{01})) \right. \\ &\quad \left. - \exp\left(\frac{\bar{\mu}_B^0}{k_B T}\right) \frac{\phi_B(t)}{(1-\phi_1)^{r_B}} \exp(r_B\phi_1(\Delta\chi_B - \chi_{01})) \right], \end{aligned} \quad (3.17)$$

where $\Delta\chi_i \equiv (\chi_{1i} - \chi_{0i})$ is the relative interaction strength of the client with the non-dilute components ($i = 0, 1$). Given ϕ_1 is a constant in the system, reaction rates $s_{A/B}$ are truly linear in their reactants' volume fractions, unlike the unimolecular reaction discussed in Sec. 2.2 where the reactants were non-dilute.

Putting things together: Reaction-diffusion equations with stationary interface

Using client components' reaction rates s_i in the dilute limit in the respective phases to obtain $s_i^{I/II}$, we use these in the thin interface model to obtain reaction-diffusion reactions in the two phases coupled with the boundary conditions as discussed above (Eq. (3.14)).

$$\partial_t \phi_i(\mathbf{r}, t) = D_i^{I/II} \nabla^2 \phi_i(\mathbf{r}, t) + s_i(\mathbf{r}, t). \quad (3.18)$$

Reactions of dilute clients at phase equilibrium

In this chapter, we also explore the kinetics of reacting dilute clients under the assumption that they can diffuse infinitely fast in the system. The reaction-diffusion length scales are

much greater than both the drop and system size. Using the evolution equation for the average client volume fraction, $\bar{\phi}_i$ as in Eq. (2.9) using average reaction rate, \bar{s}_i discussed in the subsection. 3.1.4,

$$\frac{d}{dt}\bar{\phi}_i(t) = \bar{s}_i(P_i, V^I, \{\bar{\phi}_k(t)\}). \quad (3.19)$$

At each time point, we can simultaneously obtain the client phase equilibrated volume fractions $\phi_i^{I/II}(t)$ using the partitioning degree as explained in Eq. (3.9) and the time evolved average client volume fraction, $\bar{\phi}_i(t)$.

3.2 Applications

We investigate simple chemical pathways when driven by fuel (Fig. 3.1(b)) as well as in the absence of fuel (relaxation to thermodynamic equilibrium). The continuous consumption of fuel drives the respective reactions out of chemical equilibrium, and this is maintained by $\tilde{\mu}_F^{\pm, I/II}$. The (\pm) superscript is to designate if the fuel acts in the forward (+) or backward (-) pathway. Therefore, the reaction rate constants can no longer be determined by mass-action law, given detailed balance is no longer satisfied. These out-of-equilibrium reactions can occur in both phases, I/II. However, in the results discussed below, for simplicity, we specifically choose $\tilde{\mu}_F^{+, I} \neq 0$, and the other possible choices are set to zero. Making this choice uniformly for the studies below, we'll skip the (+) superscript and use $\tilde{\mu}_F^I$, implying that the reaction is driven asymmetrically only in the drop phase (I).

Given we try to address the question of how reaction-specific "observables" are affected in presence of a drop relative to a no-drop system, we can imagine the no-drop (reference system) in four possible ways:

- (i-ii) the cases where the average scaffold volume fraction is $\bar{\phi}_1 = \phi_1^{I/II}$ such that the system is composed of one homogeneous phase with average volume fraction of scaffold either being ϕ_1^{II} ($V^I/V \rightarrow 0$) or ϕ_1^I (where the drop fills up the whole system to have one effective phase ($V^I/V \rightarrow 1$)),
- (iii) the case where scaffold component does not exist $\bar{\phi}_1 = 0$. In this case, the exchange activity coefficient is identically unity for all dilute, reactive components following from Eq. (3.3), unlike the former case, where it is not equal to unity,
- (iv) the case where corresponding to an average scaffold volume fraction $\bar{\phi}_i$ at which phase-separation occurs, the demixed state is suppressed by continuous stirring to have a no-drop reference state.

For the discussion of the applications, we choose case (i) as our preferred reference system, where the scaffold is at, and what can be addressed as the threshold volume fraction where the onset of phase separation has not yet occurred.

We would like to study the behavior of the so-called observables by changing the drop size V^I/V . This can be achieved by gradually changing $\bar{\phi}_1$ from $\phi_1^{II} \rightarrow \phi_1^I$. Varying the average scaffold in the system does not affect the exchange activity coefficients of clients, given those are solely dependent on the equilibrium phase volume fractions, $\phi_1^{I/II}$, which

remain unaffected (refer to the interpretation of binary phase diagram in Fig. 1.6(a)). Additionally, to define the observables, we use the average volume fractions computed by,

$$\bar{\phi}_i(t) = \frac{1}{V} \int_V d^3\mathbf{r} \phi_i(\mathbf{r}, t). \quad (3.20)$$

We can have a generalized reaction scheme where H number of reactants A_i can react in the presence of fuel, F to form product B , which can spontaneously decompose back to the reactants,



The possible variations of this process can be unimolecular (two-state) and bimolecular reactions, with and without the presence of fuel. We discuss the two-state process first.

3.2.1 Two-state transitions controlled by a drop

The framework about to be discussed can be applied to different biologically relevant transitions like protein misfolding between two states, referred to as *activated* B and *deactivated* A_1 .

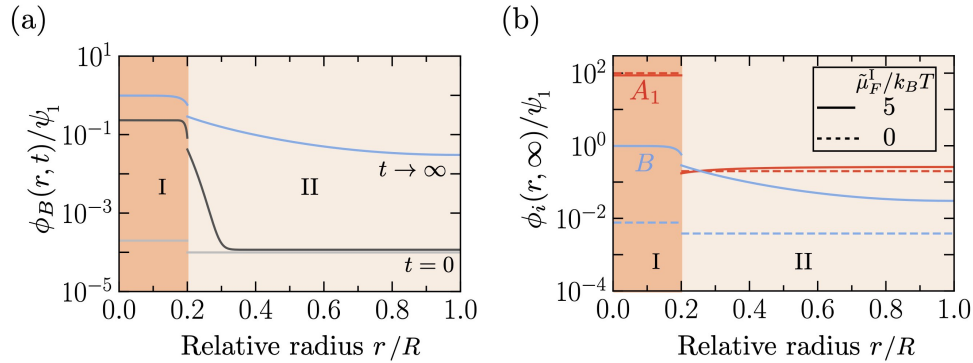


Fig. 3.6: Spatio-temporal and steady state spatial profiles of the clients. (a) In the presence of fuel, the product is initialized at phase eq. (gray) evolves to the NESS (blue) with pronounced gradients set by $\lambda_{\text{rd}}^{\text{I/II}}$ governed by Eq. (3.18), (b) The steady state spatial profiles of the clients, where in the absence of fuel (color dashed) system relaxes to thermodynamic equilibrium (flat profiles). Parameters are listed in the L.O.F section.

In general, for dilute reactive clients, we can write,

$$\exp\left(\frac{\bar{\mu}_i}{k_B T}\right) = \exp\left(\frac{\bar{\mu}_i^0}{k_B T}\right) \bar{\gamma}_i(\phi_1) \phi_i. \quad (3.22)$$

In this study, the observable we define is the relative yield or the relative steady state average volume fraction of the product B ,

$$\mathcal{Y} = \frac{\bar{\phi}_B(\infty)}{\bar{\phi}_B(\infty)|_{V^I=0}}. \quad (3.23)$$

The numerator of the observable is equivalently, $\bar{\phi}_B(\infty)|_{\text{drop}}$ which is a function of drop

volume (in turn varying $\bar{\phi}_1$ (Eq. (3.8h))), and the denominator is similarly $\bar{\phi}_B(\infty)|_{\text{no drop}}$ which is a constant evaluated at scaffold volume fraction, $\bar{\phi}_1 = \phi_1^{\text{II}}$.

The chemical reaction rates for product B and reactant A_1 are as follows,

$$\begin{aligned} s_B^{\text{I/II}} &= -s_{A_1}^{\text{I/II}} \\ &= k^{\text{I/II}} \left[\exp\left(\frac{\bar{\mu}_{A_1}^0 + \tilde{\mu}_F^{\text{I/II}}}{k_B T}\right) \bar{\gamma}_{A_1}^{\text{I/II}} \phi_{A_1}^{\text{I/II}}(t) - \exp\left(\frac{\bar{\mu}_B^0}{k_B T}\right) \bar{\gamma}_B^{\text{I/II}} \phi_B^{\text{I/II}}(t) \right]. \end{aligned} \quad (3.24)$$

To obtain the average steady state volume fraction of the product for the reference state using $\psi_1 = (\bar{\phi}_{A_1} + \bar{\phi}_B)$ as the conserved quantity, we obtain the steady state by solving $\bar{\mu}_{A_1} = \bar{\mu}_B$, since the external energy source of the fuel, $\tilde{\mu}_F^{\text{I}}$ disappears with the drop,

$$\bar{\phi}_B(\infty)|_{V^{\text{I}}=0} = \frac{\exp\left(\frac{\bar{\mu}_{A_1}^0}{k_B T}\right) \bar{\gamma}_{A_1}(\phi_1^{\text{II}})}{\exp\left(\frac{\bar{\mu}_{A_1}^0}{k_B T}\right) \bar{\gamma}_{A_1}(\phi_1^{\text{II}}) + \exp\left(\frac{\bar{\mu}_B^0}{k_B T}\right) \bar{\gamma}_B(\phi_1^{\text{II}})} \psi_1. \quad (3.25)$$

In the thin interface model, one can obtain analytical solutions for the steady state spatial profile of clients (details in Appendix. E).

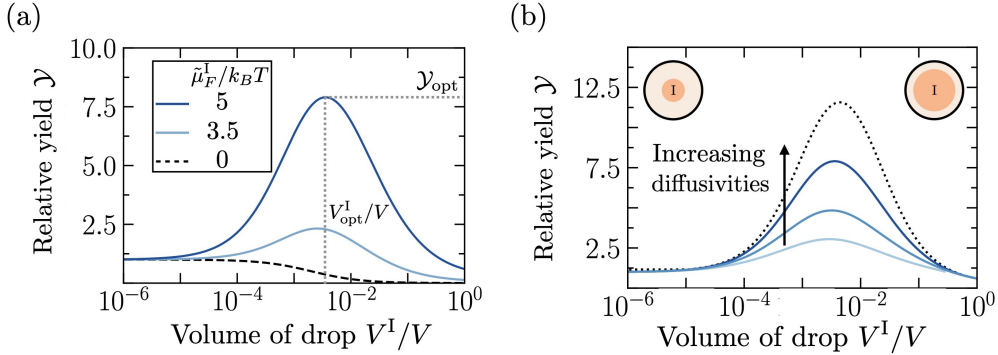


Fig. 3.7: Relative yield is most significant in the presence of fuel and at infinite diffusivity. (a) In the absence of fuel (black dashed), the system loses its optimality in yield, and the yield is most amplified for higher fuel energy, $\tilde{\mu}_F^{\text{I}}$. (b) The yield is the most amplified in the limit of infinite diffusivities of clients (black dotted). Parameters are listed in the L.O.F section.

In the limit of infinite fast diffusion, the volume fraction in the respective phases is homogeneous, and we can obtain the average steady state volume fraction of the product analytically as,

$$\bar{\phi}_B(\infty) = \frac{\exp\left(\frac{\bar{\mu}_{A_1}^0}{k_B T}\right) \bar{\gamma}_{A_1}^{\text{I}} P_{A_1} \zeta_{A_1} \left[\sum_{\Gamma} V^{\Gamma} k^{\Gamma} \exp\left(\frac{\tilde{\mu}_F^{\Gamma}}{k_B T}\right) \right]}{\exp\left(\frac{\bar{\mu}_{A_1}^0}{k_B T}\right) \bar{\gamma}_{A_1}^{\text{I}} P_{A_1} \zeta_{A_1} \left[\sum_{\Gamma} V^{\Gamma} k^{\Gamma} \exp\left(\frac{\tilde{\mu}_F^{\Gamma}}{k_B T}\right) \right] + \exp\left(\frac{\bar{\mu}_B^0}{k_B T}\right) \bar{\gamma}_B^{\text{I}} P_B \zeta_B \left[\sum_{\Gamma} V^{\Gamma} k^{\Gamma} \right]} \psi_1, \quad (3.26)$$

where $\Gamma = \text{I, II}$ is the phase index. To solve for the existence of optimality, we obtain the slope of the Eq. (3.26) and get the conditions at the limits, $V^{\text{I}} \rightarrow 0$ and $V^{\text{I}} \rightarrow 1$, which

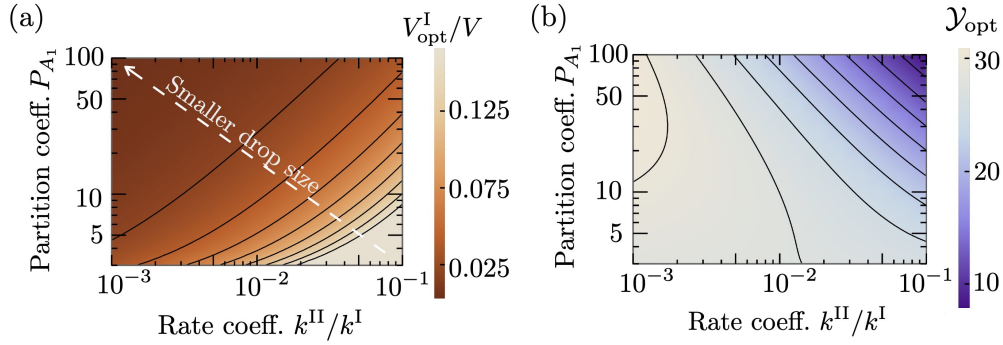


Fig. 3.8: Relative yield optimality for varying parameters. (a) Small drop size best optimizes the relative yield, and not when the drop fills the whole system. (b) High values of the reactant's partition coefficient, P_{A_1} , and slow kinetics in the dilute phase allow for maximum relative yield. Parameters are listed in the L.O.F section.

are respectively,

$$\frac{k^{\text{I}}}{k^{\text{II}}} > \frac{(P_B - P_{A_1})}{\left(1 - \exp\left(\frac{\tilde{\mu}_F^{\text{I}}}{k_B T}\right)\right)}, \quad (3.27a)$$

$$\frac{k^{\text{I}}}{k^{\text{II}}} > \frac{P_{A_1} P_B \left(1 - \exp\left(\frac{\tilde{\mu}_F^{\text{I}}}{k_B T}\right)\right)}{\exp\left(\frac{\tilde{\mu}_F^{\text{I}}}{k_B T}\right) (P_B - P_{A_1})}. \quad (3.27b)$$

If both the above conditions are satisfied, then optimality exists as a function of drop volume. The other parameters that control the optimality conditions in Eq. (3.27), are the partition coefficients P_i , the reaction rate coefficients, $k^{\text{I/II}}$ and external fuel energy $\tilde{\mu}_F^{\text{I}}$. Absence of $\tilde{\mu}_F^{\text{I}}$ leads to loss of optimality as can be verified from the conditions, Eq.(3.27), because the average volume fractions are linear functions in phase volumes and optimality mainly arises from the dependence on the drop volume as a non-linear function.

In this study, we fix $\tilde{\mu}_F^{\text{I}}$, partition coefficient of the product P_B . We analyze the optimal relative yield, \mathcal{Y}_{opt} and the optimal drop volume $V_{\text{opt}}^{\text{I}}/V$ by varying the partition coefficient of the reactant P_{A_1} and the reaction rate coefficient ratio, $k^{\text{II}}/k^{\text{I}}$. The maximum relative yield observed for the studied range of parameters ($\mathcal{Y}_{\text{opt}} \approx 30$), implies that a drop with a localized fuel source can lead to the formation of more product in the system at steady state. We see in Fig. 3.8(b) that low $k^{\text{II}}/k^{\text{I}}$ and high P_{A_1} have the highest optimal value for relative yield. It is because the spontaneous conversion to A_1 of the product B needs to be suppressed, and the reactant A_1 has to be more in the drop where the external fuel can convert it actively to the product.

3.2.2 Bimolecular reaction controlled by a drop

The bimolecular reaction has 2 conserved quantities, $\psi_1 = (\bar{\phi}_{A_1} + \bar{\phi}_{A_2} + \bar{\phi}_B)$ and $\psi_2 = (\bar{\phi}_{A_1} - \bar{\phi}_{A_2})$ as had been discussed earlier in Sec. (2.3). For the most general case of active

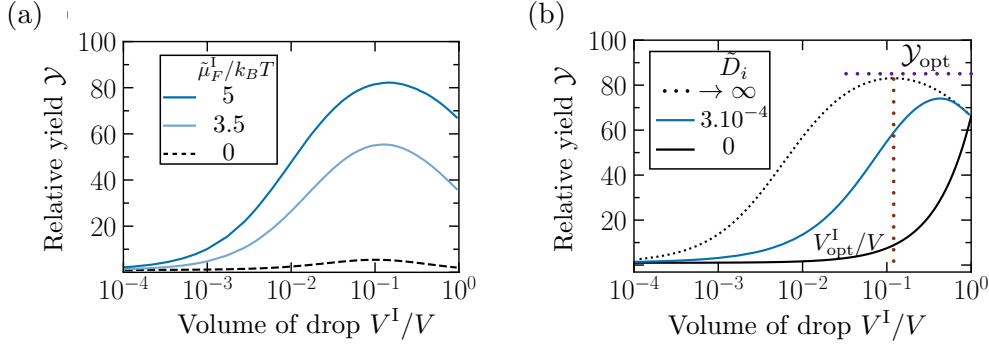


Fig. 3.9: Relative yield optimality is most significant in the presence of fuel and high diffusivities. (a) Due to its bimolecular nature, optimality can exist even in the absence of fuel (black dashed), and yield is more pronounced with more fuel energy (blue shades). (b) Reaction proceeding at phase equilibrium has the highest yield (black dotted) compared to when clients' rescaled diffusivities, \bar{D}_i , are low (blue) and when clients don't diffuse (black solid). The last case implies they locally settle to their effective chemical equilibrium in the respective phases, and therefore there cannot exist optimality in this case. Parameters are listed in the L.O.F section.

bimolecular reaction, the reaction rate is given as,

$$\begin{aligned} \frac{s_B^{I/II}(\mathbf{r}, t)}{2} &= -s_{A_{1/2}}^{I/II}(\mathbf{r}, t) \\ &= k^{I/II} \left[\exp\left(\frac{\bar{\mu}_{A_1} + \bar{\mu}_{A_2} + \bar{\mu}_F^{+, I/II}}{k_B T}\right) - \exp\left(\frac{\bar{\mu}_B}{k_B T}\right) \right]. \end{aligned} \quad (3.28)$$

To solve for the steady state of the product B in the reference system (no drop), we can solve for the physically valid root from the quadratic equation obtained from applying the condition of chemical equilibrium ($\sum_{i=1}^2 \bar{\mu}_{A_i} = \bar{\mu}_B$),

$$\begin{aligned} \bar{\phi}_B(\infty)|_{V^I=0} &= \exp\left(\frac{\bar{\mu}_{A_1}^0 + \bar{\mu}_{A_2}^0 - \bar{\mu}_B^0}{k_B T}\right) \left(\frac{\bar{\gamma}_{A_1}(\phi_1^{\text{II}}) \bar{\gamma}_{A_2}(\phi_1^{\text{II}})}{\bar{\gamma}_B(\phi_1^{\text{II}})}\right) \left(\frac{\psi_1 + \psi_2 - \bar{\phi}_B(\infty)}{2}\right) \\ &\quad \left(\frac{\psi_1 - \psi_2 - \bar{\phi}_B(\infty)}{2}\right). \end{aligned} \quad (3.29)$$

For the system with a drop, in the infinite diffusion limit, we obtain the physically relevant root as,

$$\bar{\phi}_B(\infty) = 2C + \psi_1 - \sqrt{4C^2 + 4C\psi_1 + \psi_2^2}, \quad (3.30)$$

where $C = \exp\left(\frac{\bar{\mu}_{A_1}^0 + \bar{\mu}_{A_2}^0 - \bar{\mu}_B^0}{k_B T}\right) \frac{\bar{\gamma}_B^I P_B \zeta_B}{\prod_{i=1}^2 \bar{\gamma}_{A_i}^I P_{A_i} \zeta_{A_i}} \left[\frac{\sum_{\Gamma} V^{\Gamma} k^{\Gamma}}{\sum_{\Gamma} V^{\Gamma} k^{\Gamma} \exp\left(\frac{\bar{\mu}_F^{\Gamma}}{k_B T}\right)} \right]$. Similar to the two-

state transition (unimolecular), we also here investigate the relative yield (defined in Eq. (3.23)) as in Fig. 3.9, where we conclude that relative yield is the highest corresponding to high external energy supply and when the reactions proceed at phase equilibrium, implying infinite limit of diffusivities for the clients.

As we observe from the expressions for the steady state, they tend to get less tractable analytically with increasing reaction orders. However, in the limit of infinite diffusivities of

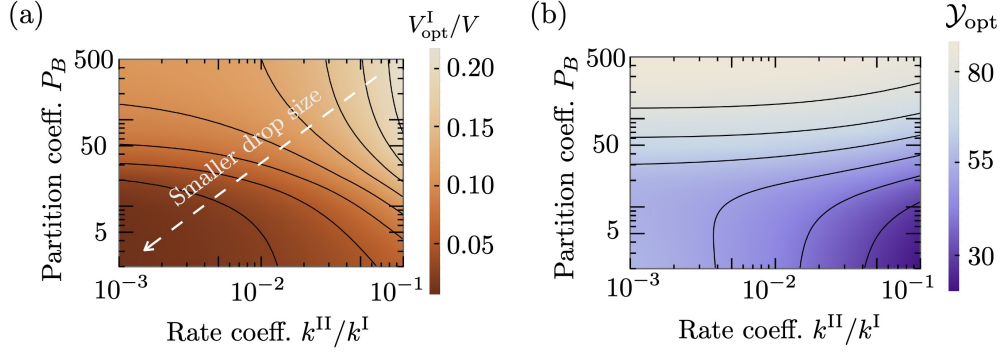


Fig. 3.10: Relative yield optimality for varying parameters. (a) Medium drop size best optimizes the relative yield, (b) $\mathcal{Y}_{\text{opt}} \approx 80$, for a high partition coefficient of the product P_B and not too strongly varying with the reaction rate coefficients. Parameters are listed in the L.O.F section.

clients or reactions at phase equilibrium, there is relatively more control and accessibility with analytical expressions of the observables. For the bimolecular reaction, the steady state spatial profiles as solutions of Eq. (3.18) can be only obtained numerically (scheme discussed in Appendix. B).

3.2.3 Nucleation reaction controlled by a drop

We also apply the framework to study both thermodynamic and fuel-mediated nucleation pathways. In this subsection, we look into the types of reactions that mimic the nucleation of fibrils and filaments. The nucleation processes studied are primarily dictated as,



where n is the nucleation number of monomers A (or order of the process), essential to undergo a nearly irreversible transition to form a dimer/trimer, A_n , depending on the value of n (here we focus on $n = 2, 3$). The conserved quantity here is $\psi_1 = (\bar{\phi}_A + \bar{\phi}_{A_n})$. The phase-dependent chemical reaction rate of this reaction scheme is given as,

$$\begin{aligned} s_{A_n}^{I/II}(\mathbf{r}, t) &= -s_A^{I/II}(\mathbf{r}, t) \\ &= k^{I/II} \left[\exp\left(\frac{n\bar{\mu}_A + \tilde{\mu}_F^{+, I/II}}{k_B T}\right) - \exp\left(\frac{\bar{\mu}_{A_n}}{k_B T}\right) \right]. \end{aligned} \quad (3.32)$$

For this reaction, the observable we wish to study is the relative initial rate of nucleation,

$$\mathcal{R} = \frac{\dot{\bar{\phi}}_A(0)}{\bar{\phi}_A(0)|_{V^I=0}}, \quad (3.33)$$

where the average initial rate at phase equilibrium (can be calculated analytically) is as follows using Eq. (3.32) in Eq. (2.9),

$$\dot{\bar{\phi}}_A(0) = \frac{V^I}{V} s_A^I(0) + \frac{(1 - V^I)}{V} s_A^{II}(0). \quad (3.34)$$

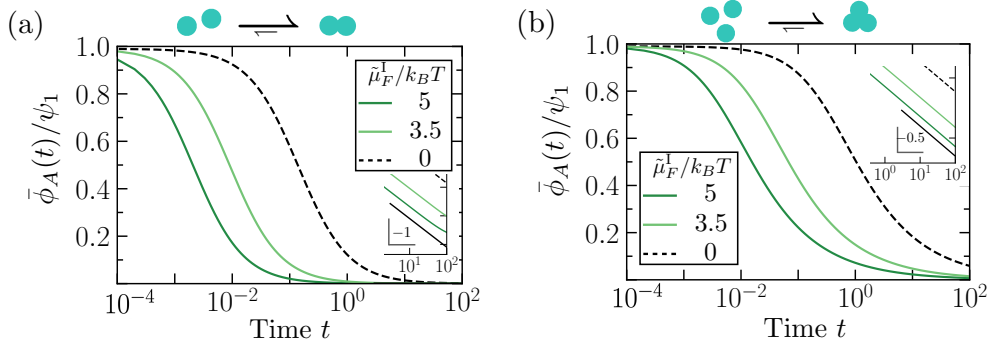


Fig. 3.11: Temporal traces for monomers with varying nucleation numbers. At phase equilibrium, (a) for $n = 2$ and (b) $n = 3$, we study the temporal profiles for varying fuel energy $\tilde{\mu}_F^I$, with the fastest average initial decay rate corresponding to the highest value of $\tilde{\mu}_F^I$. Here we fix a specific drop volume where the temporal profiles are studied. We also recognize the long-time behavior of this process. For the decaying monomers, it scales with the nucleation orders as $\propto t^{-1/(n-1)}$; hence t^{-1} and $t^{-0.5}$ for $n = 2$ and 3 , respectively. Parameters are listed in the L.O.F section.

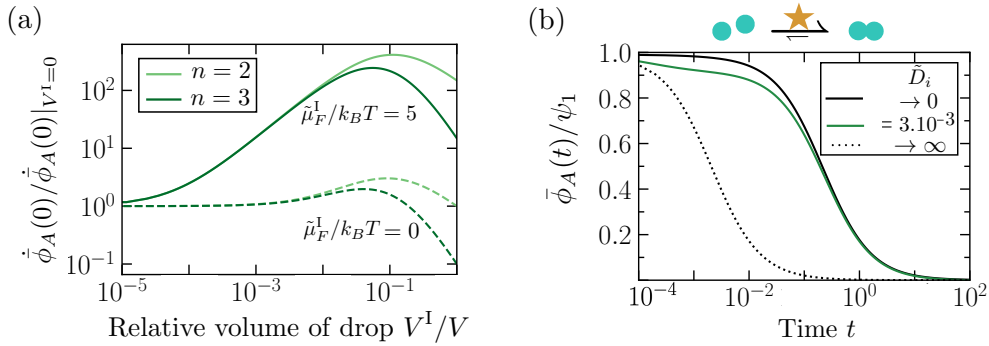


Fig. 3.12: Nucleation number, fuel, and diffusivity affect the relative average initial rate. (a) For the initial parameters chosen here, the observable is higher for the smaller nucleation number ($n = 2$, light green shades) and in the presence of fuel (solid green lines). (b) In a fixed drop volume, infinite diffusivity of monomers \tilde{D}_A (black dotted) have the highest average initial rate followed by low but finite diffusivities (solid green). The average initial rate is the slowest in the limit of no diffusion. However, the long-time scaling behavior remains unaffected, $\propto t^{-1}$ for $n = 2$. Parameters are listed in the L.O.F section.

Like the previous applications, we also study this system using the rates defined above (Eq. (3.32)) in Eq. (3.18) using the numerical scheme discussed in Appendix. B to obtain the average temporal profiles of the monomers for finite diffusivity of the monomers (Fig. 3.12(b)).

The average initial nucleation rate studied here decreases with an increase in nucleation number n because of the chosen parameters, but it usually depends on the initial volume

fraction of monomers. However, in the presence of a drop, this average initial nucleation rate can be sped up depending on the diffusivity of the monomers \tilde{D}_A , their partition coefficient P_A , the reaction rate coefficients, $k^{I/II}$ and the drop volume V^I . However, the long-time scaling of the average volume fraction profiles is robust in the system.

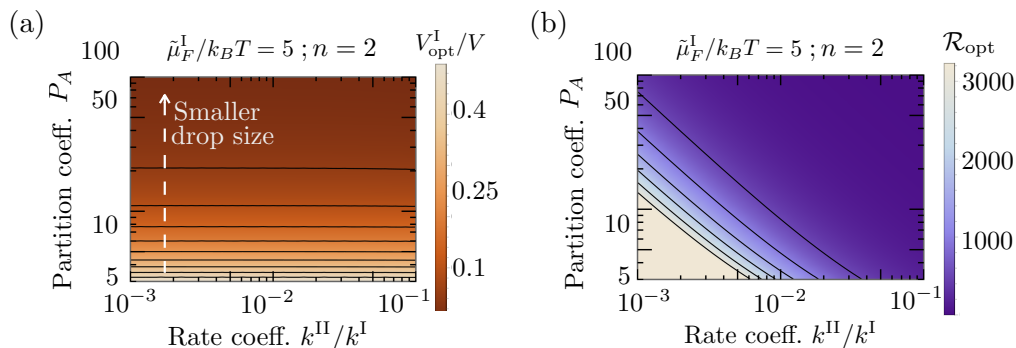


Fig. 3.13: Relative yield optimality for varying parameters. Here, we analyze the optimal behavior as functions of the monomer partition coefficient P_A and reaction rate coefficients. (a) Higher partitioning of monomers is required in smaller drops to obtain optimal relative initial rate, (b) which can be significantly high even for small partition coefficient values of monomers P_A and suppressed reaction rate coefficients outside the drop. Parameters are listed in the L.O.F section.

3.3 Summary

In this chapter, we tried to develop the framework to understand scaffold-client systems, where the scaffold is non-reactive. We defined the dilute limit of the clients, with an estimate for the client volume fraction, discussed in Appendix. C, as a function of all other thermodynamic parameters in the system. Beyond this threshold value of the client volume fraction, the approximation fails to hold.

We are interested in the domain of the composition space of scaffold-solvent-clients, where the approximation is valid. In this domain, we calculated the thermodynamic equilibrium conditions and the kinetic equations originating from conservation laws. We can immediately simplify the kinetics by decoupling the clients' evolution equations from that of the scaffold, which we also assume is stationary and provides a heterogeneous background for the clients and can affect the kinetic coefficients, both for reaction and diffusion ($k^{I/II}$ and $D_i^{I/II}$).

We study the spatiotemporal model as coupled reaction-diffusion equations in the two phases and the temporal model, which is essentially the reaction kinetics at phase equilibrium discussed in chapter 2. We apply these models to three reaction processes to notice a key property of optimizing an observable of the individual reactions by tuning the drop volume V^I . We understand that non-linearity in the reaction scheme, either obtained via higher-order reaction processes (not unimolecular) or coupling phase-dependent external fuel energy sources to linear processes, is the key ingredient to observing optimality with a certain choice of other parameters in the model that can tune the optimality, and also lead to its suppression. This study can be useful to systems biology experimental design to tune parameters in the model to optimize a certain functionality.

Chapter 4

Fuel-driven chemical reactions in the dilute phase at phase equilibrium

"Living matter evades the decay to equilibrium. How does the living organism avoid decay? The obvious answer is: By eating, drinking, breathing and (in case of plants) assimilating. The technical term is metabolism."

– Erwin Schrödinger, *What is Life?*

In recent years, chemical reaction cycles driven by chemical fuel consumption have been introduced that regulate the ability of molecules to assemble or phase-separate, resulting in dynamic structures like colloids [78], fibers [79], supramolecular polymers [80], oil-based droplets [78], coacervate-based droplets [81], and vesicles [82], to name a few. Due to the transient nature of these so-called "building blocks", these assemblies are endowed with properties typically absent at thermodynamic equilibrium. For example, fibrils that spontaneously self-divide. Moreover, the theory on active emulsions suggests that droplets can self-divide [83]. More recently, examples of assemblies were observed that exert feedback over their chemical reaction cycle. The underlying mechanisms can result in exciting behavior, like the spontaneous emergence of switches between the morphologies or the ability of molecules to persist while others decay [78]. All these developments in the field are incremental steps toward the synthesis of life, and a living system essentially represents a complex nonequilibrium assembly of molecules that are regulated by chemical reaction cycles.

The objective of this chapter is, therefore, to theoretically probe such a bottom-up approach in systems chemistry to couple a library of precursors that consume chemical fuel to form hydrophobic oil-like drops in the system. The chemical reaction cycle transiently forms these building blocks, which subsequently die in the system due to hydrolysis. Theoretically, we can approach to understand this system using tools from chapter 2, given the molecules are tiny and have high diffusion coefficients compared to reaction rate coefficients, allowing us to assume that the system remains at phase equilibrium through its kinetic evolution. Here, we use concentrations as variables since the experimental data is available in concentration units, specifically millimolar, in this study.

The experiments in this work were carried out by Patrick Schwarz, Tabea Huss, and Job Boekhoven at the Dept. of Chemistry, TU Munich. The theory was developed in collaboration with Jacqueline Janssen. The results discussed in this chapter can be found in Ref. [60].

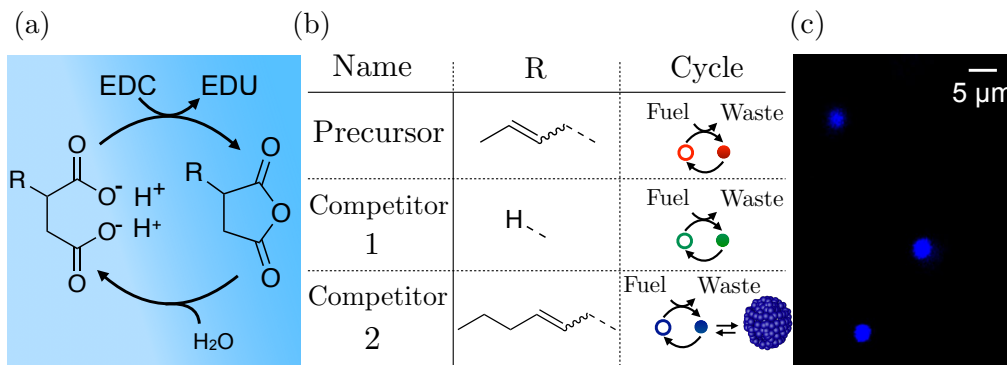


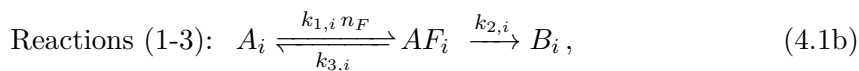
Fig. 4.1: The design of chemically fueled reaction cycles. (a) The chemically fueled reaction cycle used in this work. Succinate derivatives are converted into their corresponding transient anhydrides by consuming the chemical fuel EDC. (b) Molecular structures of the precursor, competitor 1, and competitor 2. The cycle column shows a schematic representation of the cycle with the succinate derivative as an open circle and the anhydride as a closed circle. Competitor 2 can form droplets. (c) Confocal microscopy of 50 mM competitor 2 fueled with 100 mM EDC. The corresponding anhydride product phase separates into micron-sized oil droplets.

4.1 Chemical reaction network and its properties

Similar to the fuel-driven reaction cycles in biological systems, the energy obtained from the hydrolysis of 1-ethyl-3-(3-dimethylaminopropyl)carbodiimide (EDC, labeled F) is used for the transient activation of the succinate derivative (labeled A_i with $i = P, C_1, C_2$). In this study, three succinate derivatives were used: (E/Z)-2-buten-1-ylsuccinate, which we refer to as precursor (A_P), succinate (competitor 1, A_{C_1}), and (E/Z)-2-hexen-1-ylsuccinate (competitor 2, A_{C_2} , Fig. 4.1(a)).

The intermediate molecule, AF_i , comprises fuel and the respective succinate derivative. There are three corresponding anhydrides, abbreviated as B_i , and referred to as product, product of competitor 1, or product of competitor 2. The anhydride products used experimentally are (E/Z)-2-buten-1-ylsuccinic anhydride (product), succinic anhydride (product of competitor 1), and (E/Z)-2-hexen-1-ylsuccinic anhydride (product of competitor 2). In our systems, the solvent is water (0).

The following reaction schemes can summarise all reactions in the cycle:



The fuel F can undergo two chemical reactions: F can get slowly hydrolyzed to waste W with a reaction rate coefficient k_0 (**Reaction (0)**, Eq. (4.1a)), or the fuel F drives the transition from the succinate derivative A_i to the intermediate AF_i with a chemical reaction rate that is proportional to the fuel concentration n_F with a rate constant $k_{1,i}$ (**Reaction (1)**, second order chemical reaction). This intermediate molecule, AF_i can spontaneously hydrolyze back to A_i with a rate constant $k_{3,i}$, or irreversibly turn over

to the anhydride B_i (**Reactions (1-3)**, Eq. (4.1b)). The turn-over to the anhydride (**Reaction (2)**) occurs spontaneously as an intramolecular reaction with a rate constant $k_{2,i}$ (first-order reaction).

In aqueous media, this anhydride hydrolyzes and thereby turns over to the initial succinate derivative A_i with rate coefficient $k_{4,i}$ (**Reaction (4)**) (Eq. (4.1c)), which we shortly refer to as the deactivation step. Considering a constant pH and approximately dilute conditions relative to water, deactivation follows a first-order chemical reaction with a deactivation rate constant $k_{4,i}$. The anhydride population can thus only be maintained when the rate of activation equals the rate of deactivation.

4.1.1 Observations from individual reaction cycles

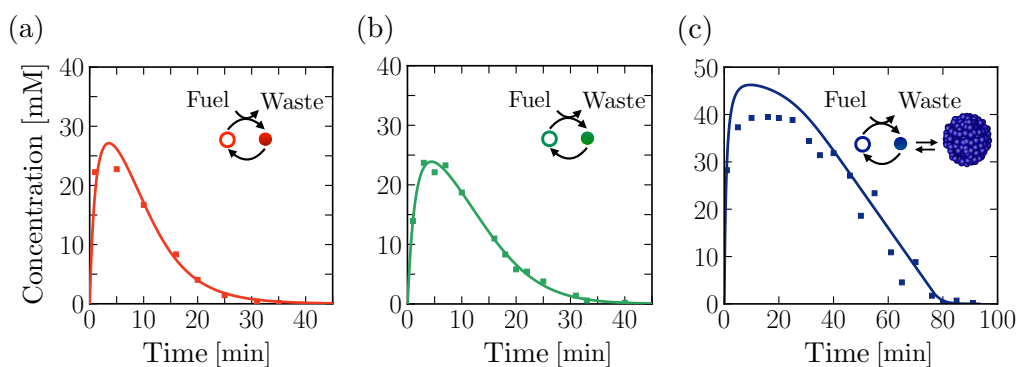


Fig. 4.2: Individual reaction properties. The anhydride product concentration profile of 50 mM precursor (a), competitor 1 (b), and competitor 2 (c) fueled with 100 mM EDC. Markers represent HPLC data; solid lines represent data calculated using the theoretical kinetic model.

It was observed that the addition of fuel to competitor 2 made the solution turn turbid due to the presence of oil droplets which was verified via confocal microscopy (Fig. 4.1(c)), and is in line with previous work [82]. However, the emergence of droplets could not be observed for the precursor and competitor 1.

To determine the kinetics of the three reaction cycles, 50 mM of each succinate derivative was fueled with 100 mM EDC and the corresponding anhydride product concentration was quantified by means of high-performance liquid chromatography (HPLC) [84]. On fueling 50 mM precursor with 100 mM EDC, the precursor was immediately converted to roughly 25 mM of the product (yield) and, after the depletion of the fuel, degraded rapidly with a first-order decay within 24 minutes (lifetime)(Fig. 4.2(a)).

Next, fueling 50 mM of competitor 1 with 100 mM EDC, a similar observation was made in terms of the yield and lifetime (Fig. 4.2(b)).

In contrast, under the same conditions, fueling competitor 2 resulted in 45 mM anhydride product yield, which survived for over an hour (Fig. 4.2(c)).

The increased yield and lifetime of the droplet-forming anhydride product of competitor 2 was previously described by a self-protection mechanism, i.e., the phase-separated anhydride product is shielded from water and thus protected from hydrolysis [82]. Consequently, hydrolysis occurs only on the anhydride molecules in the solution, which we refer

to as the dilute phase equilibrium concentration of the anhydride product ($n_{B_i}^{\text{II}}$). The hydrolysis rate can then be calculated by $\propto k_{4,i}n_{B_i}^{\text{II}}$, where $k_{4,i}$ is the hydrolysis rate coefficient. Since both k_{4,C_2} and $n_{B_{C_2}}^{\text{II}}$ are constant, the effective hydrolysis rate is a constant, leading to a linear decay of the average anhydride product of competitor 2 concentration when all fuel is consumed (Fig. 4.2(c)).

4.1.2 Observations from combined reaction cycles

The kinetics of the reaction cycles were tested and observed to be affected when the precursor competed with either competitor 1 or competitor 2 for fuel in terms of the yields and lifetimes as observables. The lifetime was defined as the time period during which the average product concentration exceeded a chosen threshold of 2 mM. The threshold concentration of 2 mM was chosen as it was equal to the dilute phase equilibrium concentration of competitor 2 ($n_{B_{C_2}}^{\text{II}}$), meaning droplets dissolved below this threshold. Moreover, the threshold value was not in the tailing regime of the exponential decay of the anhydrides allowing to capture the effects of phase separation on product lifetime.

Precursor vs Competitor 1

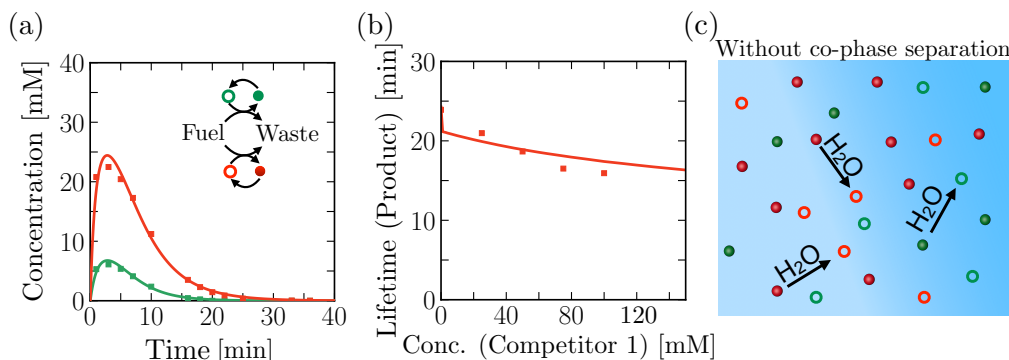


Fig. 4.3: Competition between reaction cycles for a shared fuel - I. (a) The anhydride concentration profiles when 50 mM precursor (red) and 50 mM competitor 1 (green) compete for 100 mM EDC. (b) The lifetime of the product against the concentration of competitor 1. The lifetime decreases with increasing competition. (c) Schematic representation of the hydrolysis of anhydrides in the experiment in (a). Markers represent HPLC data; solid lines represent data calculated using the theoretical kinetic model.

When equal concentrations of the precursor and competitor 1 were mixed and fueled with 100 mM EDC, it was found that it led to lower yields and shorter reaction cycles for each of the anhydrides compared to their respective non-competing reaction cycles (Fig. 4.3(a) versus Fig. 4.2(a-b)). To quantify this effect, the lifetime of the product was measured as a function of competitor 1 concentration, keeping the precursor concentration fixed at 50 mM (Fig. 4.3(b)). It was found that the lifetime decreased with increasing the concentration of competitor 1, given the fact that the precursor and competitor 1 now had less fuel at their disposal compared to their corresponding noncompeting reaction cycles. The anhydrides of both reaction cycles were present side by side and hydrolyzed in the aqueous media (Fig. 4.3(c)). In summary, both reaction cycles suffered from the

competition for fuel.

Precursor vs Competitor 2

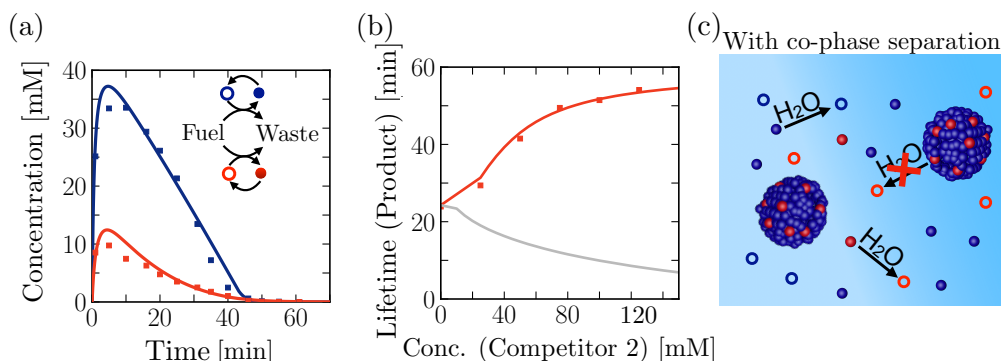


Fig. 4.4: Competition between reaction cycles for a shared fuel - II. (a) The anhydride concentration profiles when 50 mM precursor (red) and 50 mM competitor 2 (blue) compete for 100 mM fuel. (b) The lifetime of the product against the concentration of competitor 2 (red). Using the theoretical kinetic model, we show that for the same system, but in the absence of co-phase separation, the lifetime decreases (gray line). (c) Schematic representation of the hydrolysis of anhydrides in the presence of droplets. Markers represent HPLC data; solid lines represent data calculated using the theoretical kinetic model.

The relation between the lifetime and amount of competitor was very different when the precursor competed with competitor 2, which could phase-separate. Despite the competition for fuel, the lifetime of the product increased with increasing competitor 2 concentration (Fig. 4.4(a)). When 50 mM of competitor 2 was added, the lifetime of the product increased to 43 minutes, and the decay suddenly differed from the previously observed first-order decay (Fig. 4.3(a)).

The increased lifetime was particularly surprising considering that the maximum yield of the product decreased from roughly 25 mM to 10 mM when competitor 2 was added (Fig. 4.2(a) versus Fig. 4.4(a)). In contrast, the lifetime of the product of competitor 2 decreased from 77 minutes when on its own to 43 minutes when competing with the precursor for fuel (Fig. 4.2(c) versus Fig. 4.4(a)). Moreover, it was found that the maximum yield of the product of competitor 2 decreased from roughly 45 mM to 35 mM when competing with the precursor for fuel.

In summary, the product of competitor 2 suffered whilst the product benefitted from the competition for fuel between the reaction cycles. This behavior allows us to identify the product of competitor 2 *host* and the product as *parasite*. Interestingly, both anhydrides had the same lifetime indicating a coupling between the two reaction cycles. When the concentration of competitor 2 was further increased while fixing the precursor concentration, the product's lifetime increased even further (Fig. 4.4(b)).

4.2 Kinetic equations at phase equilibrium

We propose a theoretical model to explain the above observations, which is based on dilute mass-action kinetic equations which are valid when the system is homogeneous (individual reaction cycles of precursor and competitor 1, and combined reaction cycle of precursor with competitor 1). The fuel, succinate derivatives, and intermediate components are water-soluble (their interaction parameters with water and anhydride products can be set to zero, implying constant activity coefficients as discussed in subsec. (1.2.3)). Even though repulsive interaction exists between the anhydride products and water (0), the operating average anhydride concentrations are dilute ($\bar{n}_{B_i} < n_{B_i}^{\text{II}}$), preventing phase separation from occurring ($n_{B_P}^{\text{II}} = 27.8$ mM and $n_{B_{C_1}}^{\text{II}} \approx 3000$ mM) and hence validate the use of dilute limit of mass action kinetic equations. The equations are as follows,

$$\begin{aligned}
 \frac{d}{dt}\bar{n}_F &= - \sum_{i=P,C_1} k_{1,i} \bar{n}_F \bar{n}_{A_i} - k_0 \bar{n}_F, \\
 \frac{d}{dt}\bar{n}_{A_i} &= -k_{1,i} \bar{n}_F \bar{n}_{A_i} + k_{3,i} \bar{n}_{AF_i} + k_{4,i} \bar{n}_{B_i}, \\
 \frac{d}{dt}\bar{n}_{AF_i} &= k_{1,i} \bar{n}_F \bar{n}_{A_i} - (k_{3,i} + k_{2,i}) \bar{n}_{AF_i}, \\
 \frac{d}{dt}\bar{n}_{B_i} &= k_{2,i} \bar{n}_{AF_i} - k_{4,i} \bar{n}_{B_i}.
 \end{aligned} \tag{4.2a}$$

The conserved quantity in this system is $\psi_i = (\bar{n}_{A_i} + \bar{n}_{AF_i} + \bar{n}_{B_i})$, which holds for each i with $i = P, C_1, C_2$. When the system phase separates, each individual phase (oil-like drop phase and dilute aqueous phase) is treated as homogeneous (individual reaction cycle of competitor 2, and combined reaction cycle of precursor with competitor 2).

This is supported by the experimental observation that droplets form very quickly on the experimentally relevant time scales of minutes. The system undergoes fast phase separation, and diffusion kinetics of the anhydrides are instantaneous relative to their chemical reactions. Specifically, this treatment is valid if the inter-droplet distances do not exceed the reaction-diffusion length scale $\sqrt{D_i/k_{4,i}}$ for both anhydrides. Using experimental values, this reaction-diffusion length scale is in the order of a few hundred μm , while inter-droplet distances are about a few tenths of μm , supporting the validity of this approximation. This allows applying the above framework developed earlier in chapter 2 with certain modifications.

Before the onset of phase separation, the system is dictated by Eqs. (4.2a). At the time point in the reaction cycle when the average anhydride concentration reaches $n_{B_{C_2}}^{\text{II}} = 2$ mM (in case of individual reaction cycle of competitor 2) or $(n_{B_{C_2}}^{\text{II}}, n_{B_P}^{\text{II}})$ in the dilute branch in the ternary phase diagram (in case of combined reaction cycle of precursor with competitor 2), the average concentrations in the system evolves with the following equations (numerical implementation discussed in Appendix. B),

$$\begin{aligned}
 \frac{d}{dt} \bar{n}_F &= -\frac{V^{\text{II}}}{V} \left[\sum_{i=P, C_1} k_{1,i}^{\text{II}} n_F^{\text{II}} n_{A_i}^{\text{II}} - k_0^{\text{II}} n_F^{\text{II}} \right], \\
 \frac{d}{dt} \bar{n}_{A_i} &= -\frac{V^{\text{II}}}{V} \left[-k_{1,i}^{\text{II}} n_F^{\text{II}} n_{A_i}^{\text{II}} + k_{3,i}^{\text{II}} n_{AF_i}^{\text{II}} + k_{4,i}^{\text{II}} n_{B_i}^{\text{II}} \right], \\
 \frac{d}{dt} \bar{n}_{AF_i} &= -\frac{V^{\text{II}}}{V} \left[k_{1,i}^{\text{II}} n_F^{\text{II}} n_{A_i}^{\text{II}} - (k_{3,i}^{\text{II}} + k_{2,i}^{\text{II}}) n_{AF_i}^{\text{II}} \right], \\
 \frac{d}{dt} \bar{n}_{B_i} &= -\frac{V^{\text{II}}}{V} \left[k_{2,i}^{\text{II}} n_{AF_i}^{\text{II}} - k_{4,i}^{\text{II}} n_{B_i}^{\text{II}} \right].
 \end{aligned} \tag{4.2b}$$

Given we know that reaction rate coefficients can be phase dependent from chapter 2, in this study, all such coefficients are set to zero identically in the oil droplet phase ($k_{\alpha,i}^{\text{I}} = 0$), suppressing the reactions inside the droplets. This can be justified owing to the dependence of the coefficients on all non-anhydride components (water (0), F , A_i , AF_i , collectively called the solvent), which are strongly excluded in the oil droplet phase. In the dilute phase, due to zero cross interactions among all components except for the anhydrides with the solvent (χ_{0B_P} and $\chi_{0B_{C_2}}$), in the dilute phase we still treat the kinetics as it would be for dilute mass action. Here we also use the assumption that the reaction rate coefficients in the dilute phase remain the same as it was before the onset of phase separation (mixed system).

Under the valid assumption of fast diffusion kinetics compared to the slow chemical reactions outside the droplets, the average concentrations of the two anhydrides, $\bar{n}_{B_i}(t)$ determine their equilibrium concentrations via Maxwell construction using Eqs. (1.17) for an incompressible binary ($L = 1$, for individual reaction cycle of competitor 2) and ternary ($L = 2$, for combined reaction cycle of precursor and competitor 2) mixture. The volume of the dense phase (oil droplets) at each time point t :

$$\text{Maxwell construction: } \bar{n}_{B_i}(t) \rightarrow n_{B_i}^{\text{I}}(t), n_{B_i}^{\text{II}}(t), \tag{4.2c}$$

$$\text{Volume dense phase: } \frac{V^{\text{I}}(t)}{V} = \frac{\bar{n}_{B_i}(t) - n_{B_i}^{\text{II}}(t)}{n_{B_i}^{\text{I}}(t) - n_{B_i}^{\text{II}}(t)}. \tag{4.2d}$$

Obtaining reaction rate coefficients for the kinetic equations

We study the individual reaction cycles of the three succinate derivatives and their corresponding anhydrides. We fit the experimental measurements with the kinetic traces of each of the reaction cycles to determine the rate coefficients (Appendix. F, Figs. F.1, F.2 and F.3). The experimental measurements corresponding to the combined reaction cycles are then studied and fitted to determine the rate coefficients in those composite systems (Appendix. F, Figs. F.4 and F.6).

We summarise the reaction rate constants obtained from fits as mentioned above in Fig. F.8 in Appendix. F. We observed that, in general, there are only little differences in the deactivation rate constants of the single precursor system and the system where two components compete for fuel. However, a noticeable effect is a reduction in the activation pathway rate constant, primarily k_1 of competitor 1 (C_1) in the competition system with precursor

(P) and that of the precursor (P) in the competition system with competitor 2 (C_2). For both singular and competition studies, we keep the solubilities of the product and product of competitor 2 unchanged to values 2.01 mM and 27.8 mM, respectively. We thus assumed that competition for the fuel affects the availability of fuel for specific succinate derivatives. For periodic fueling studies, the lower value k_4 was used for the product. For Fig. F.3, we use the lower value of k_4 and for Fig. 4.2(c) in the main text, we use the higher value of k_4 for the product of competitor 2 as it was obtained from fitting routine.

4.3 Construction of the ternary phase diagram

To estimate the co-phase separation properties of the two anhydrides of precursor and competitor 2 with respect to the solvent, we consider the limit of excess fuel. In this case, the system mostly comprises the two anhydrides, solvent, and fuel. Due to the hydrophilic property of the fuel, we neglect its effects on phase separation. Thus, we can determine a ternary phase diagram for the remaining three molecules (product and product of competitor 2, and solvent (0)). As a model for this phase diagram, we consider a ternary, incompressible Flory-Huggins free energy density as in Eq. (1.6). We also apply the conversion from volume fractions to concentrations following Eq. (1.5) using the molar volume of the solvent as $\nu_0 = 18.02 \text{ cm}^3/\text{mol}$. The other five unknown parameters (r_{BP} , r_{BC_2} , χ_{0BP} , χ_{0BC_2} , χ_{BPBC_2}) are solved for by fitting the theoretical phase diagram to the experimental phase diagram.

The equilibrium concentrations in droplet phase (I), n_{BP}^I and $n_{BC_2}^I$, coexist with the volume fractions in aqueous phase (II), n_{BP}^{II} and $n_{BC_2}^{II}$. The volume fractions fulfill the equilibrium conditions for phase coexistence:

$$\bar{\mu}_{BP}(\{n_{B_i}^I\}) = \bar{\mu}_{BP}(\{n_{B_i}^{II}\}), \quad (4.3a)$$

$$\bar{\mu}_{BC_2}(\{n_{B_i}^I\}) = \bar{\mu}_{BC_2}(\{n_{B_i}^{II}\}), \quad (4.3b)$$

$$\Pi(\{n_{B_i}^I\}) = \Pi(\{n_{B_i}^{II}\}). \quad (4.3c)$$

Obtaining interaction parameters from the experimental phase diagram

Using the observed molar masses (see SI of Ref. [60]), we find for the product (P) and the product of competitor 2 (C_2), $m_P/m_0 = 8.56$ and $m_{C_2}/m_0 = 10.11$, respectively. In the respective binary systems, we used the molar masses relative to water as initial guesses for the fractions of the molar volumes, i.e., $r_i = \nu_i/\nu_0 \simeq m_i/m_0$, where m_i denotes the molar mass of molecule i . Given the experimental equilibrium concentrations of the anhydride molecules i ($\{n_{B_i}^I\}$, $\{n_{B_i}^{II}\}$), in their respective binary system, i.e., product (P) with solvent (0) and product of competitor 2 (C_2) with solvent (0), we solve the binary phase equilibrium conditions separately to obtain $r_P = 6.44$, $\chi_{0BP} = 1.63$ (in units of $k_B T$) and $r_{C_2} = 8.35$, $\chi_{0BC_2} = 1.76$ (in units of $k_B T$), respectively. The fractions of molar volumes we obtain are in good agreement with the mass fractions. Keeping these interaction parameters and the fraction of molar volumes fixed, we have only one

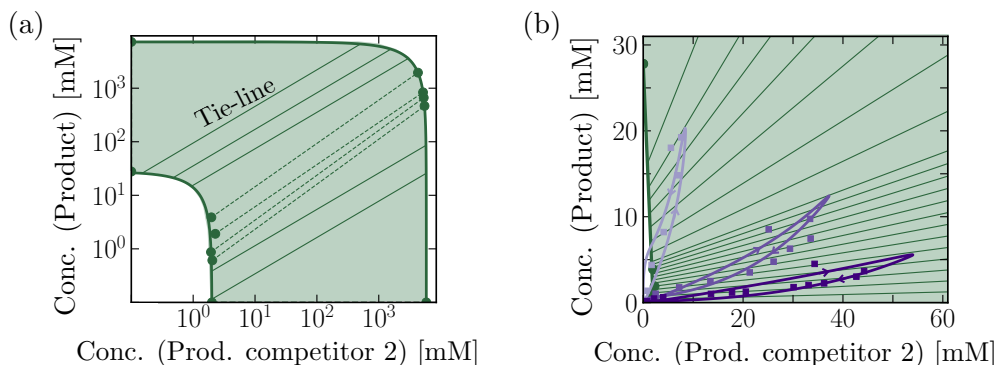


Fig. 4.5: Ternary phase diagram. (a) Ternary phase diagram (log-log representation) depicting the equilibrium concentrations of the product and the product of competitor 2. The circles correspond to the experimental data, and the solid lines represent the theoretical binodal and tie lines. The dashed lines represent the experimental tie lines. (b) The trace of average concentrations of product and product of competitor 2 in the ternary phase diagram (lin-lin representation) during the reaction cycle when 50 mM precursor and 10 mM (light hue), 50 mM (mid hue), and 125 mM (dark hue) of competitor 2 compete for 100 mM EDC. The arrows depict the direction in which the average concentrations move with time. The kinetic orbit crosses fewer tie-lines at maximal competitor 2 concentration (125 mM), suggesting the solubility change is not drastic and allows nearly zeroth order decay for both anhydrides. Markers represent HPLC data; solid lines represent data calculated using the theoretical kinetic model.

undetermined parameter left, namely $\chi_{B_P B_{C_2}}$. This parameter is obtained by solving Eqs. (4.3) and finding the best agreement with the binodal lines and tie line slopes. Very good agreement is obtained for the value $\chi_{B_P B_{C_2}} = 0$, see Fig. 4.5. $\chi_{B_P B_{C_2}} = 0$ as a parameter is consistent with the homotypic interactions and heterotypic interactions between the two anhydrides being approximately of the same magnitude; a scenario that is reasonable due to the similarity of the molecular structures of the two anhydrides.

4.4 Mechanism of co-phase separation

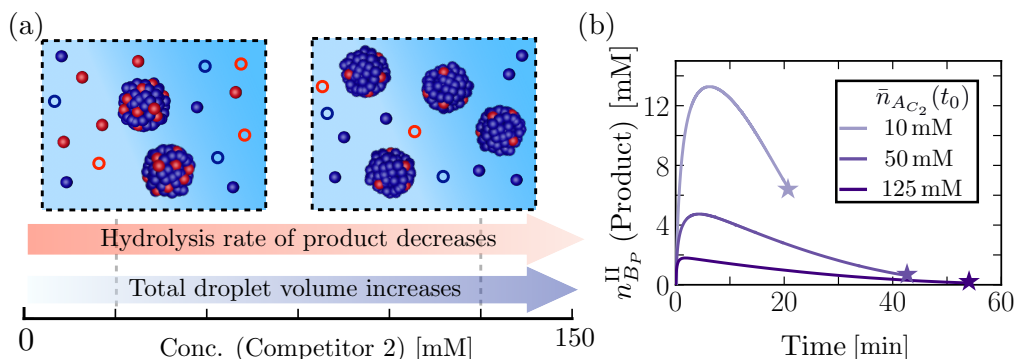


Fig. 4.6: Mechanism of co-phase separation and increased lifetime. (a) Schematic representation of how increasing concentration of competitor 2 affects co-phase separation and, thereby the hydrolysis rate of the product. (b) The dilute phase equilibrium concentration of the product $n_{B_P}^{II}$ over time for 10 mM, 50 mM, and 125 mM of competitor 2. The course of $n_{B_P}^{II}$ is dictated by the shape of the orbital in the phase diagram and the tie lines it crosses (Fig. 4.5(b)). The stars denote the point of dissolution of the droplets.

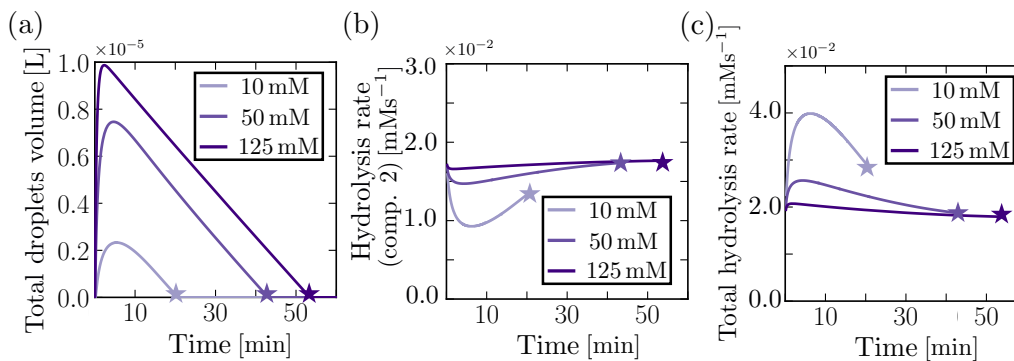


Fig. 4.7: Total droplet volume increases and total hydrolysis rate decreases in the dilute phase allowing longer survival of the parasite. (a) The total droplet volume increases with increasing the competitor 2 concentration, and the product of competitor 2 starts acting like a host to protect the parasite inside the droplets from hydrolysis. (b) The hydrolysis rate of the product of competitor 2 in the aqueous phase sets the offset of the total hydrolysis rate, and it increases with increasing competitor 2 concentration. (c) The total hydrolysis rate of both anhydrides outside the droplets. The stars denote the point of dissolution of the droplets.

We hypothesized that the counterintuitive behavior of increasing lifetime of the product with increasing the concentration of competitor 2, is related to the ability of the product to co-phase separate with the product of competitor 2. Thus, the product benefitted from the self-protection mechanism of the droplets formed by the product of competitor 2 (Fig. 4.4(c) and Fig. 4.6(a)). In other words, co-phase separation decreased the concentration of the product in the aqueous (dilute) phase (Fig. 4.6(b)) and, thereby, its hydrolysis rate. The composition of the oil phase was investigated during the reaction cycle by centrifugation and HPLC. It was found that the product was indeed part of the oil phase (Fig. 4.8).

Moreover, when the concentration of competitor 2 was increased, it was found that the composition of the oil phase changed, which suggested that the composition of the oil phase was dictated by the two reaction cycles (Fig. 4.8). The composition of the dilute phase was also measured after 16 minutes in the reaction for various competitor 2 concentrations (Fig. F.9). Assuming that the system is close to local phase separation equilibrium, the concentrations of the anhydrides in the dilute phase are approximately equal to their dilute equilibrium concentration $n_{B_i}^{\text{II}}$. It was found an almost constant $n_{B_{C_2}}^{\text{II}}$ of roughly 2 mM for the anhydride product of competitor 2 in the presence or absence of the precursor (Fig. F.9(a)).

In other words, the $n_{B_{C_2}}^{\text{II}}$ was hardly affected by the presence of the product. In contrast, we found that $n_{B_P}^{\text{II}}$ decreased drastically, ranging from roughly 28 mM without competition to 0.6 mM with 125 mM concentration of competitor 2 (Fig. F.9(b)).

We assumed that competition affects the co-phase separation as it results in an increased total droplet volume and a decreased hydrolysis rate of the product (Fig. 4.7).

The phase diagram also corroborates this where we see that if the average concentration of product of competitor 2 increases (average concentration of product remaining constant at 1 mM), the system shifts to another tie-line, and the concentration, $n_{B_P}^{\text{II}}$ of the product

decreases further (Fig. 4.5(b)). Each data point on such a kinetic orbit can be decomposed into concentrations of the anhydrides in the aqueous and in the oil phase. If an orbit lies parallel to a tie line, the anhydride concentrations in the aqueous phase remain almost constant over time. This implies that both anhydrides hydrolyze via kinetics close to zeroth-order as long as droplets are present. However, if the orbit evolves through several tie lines, the product concentration in the aqueous phase changes with time. In other words, the concentration, $n_{B_{C_2}}^{\text{II}}$ of the product of competitor 2 in the aqueous phase barely changes and is independent of the shape of the orbit, i.e., hydrolysis occurs via zeroth-order kinetics with or without the product. In contrast, the concentration, $n_{B_P}^{\text{II}}$ of the product changed drastically with the amount of competitor 2, and its time-dependent evolution depends on the shape of the orbit through the phase diagram.

The theoretical kinetic model allowed us to calculate the outside equilibrium concentration of the product, $n_{B_P}^{\text{II}}$ as a function of time for different competitor 2 concentrations (Fig. 4.6(b)). For low concentration of competitor 2, the concentration $n_{B_P}^{\text{II}}$ varied drastically from roughly 5 mM to 0.7 mM over the course of the reaction cycle. In contrast, for high concentration of competitor 2, the concentration $n_{B_P}^{\text{II}}$ varied only from roughly 2 mM to 0.5 mM (mid hue and dark hue in Fig. 4.6(b)).

In summary, we show that the orbit shape is influenced by the amount of competitor 2, i.e., the more competitor is present, the more parallel the orbits are oriented with respect to the tie-lines. However, due to adding fuel only at the beginning of the kinetics, all systems show a single orbit that enters and leaves the domain of co-phase separation in the phase diagram.

4.4.1 Composition of droplets

We quantified the percentage of the droplet material composed of the product for three different conditions with increasing competitor 2 concentration.

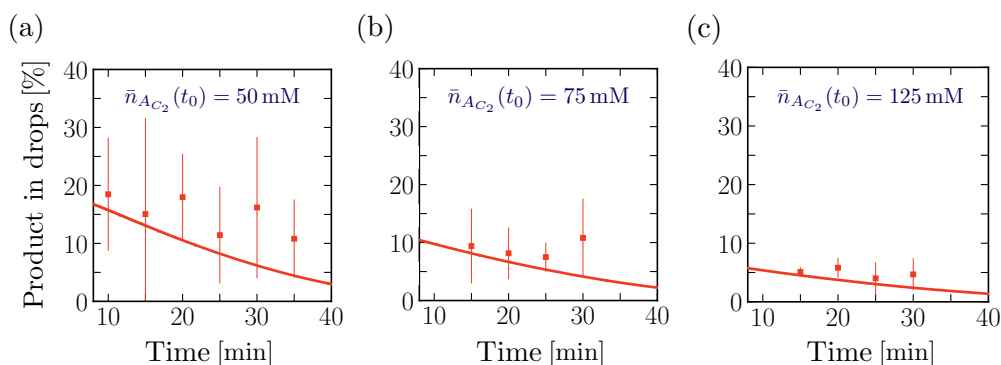


Fig. 4.8: Reduction in the composition of the product (parasite) in the droplets with increasing product of competitor 2 (host) concentration. (a) 50 mM, (b) 75 mM, (c) 125 mM, respectively. Increasing the concentration of the host reduces the maximum concentration of the parasite in the droplets. Also, the maximum value of the product monotonically decreases with time as the total volume of droplets keeps decreasing. Markers represent ratio calculated using HPLC data; solid lines represent data calculated using the theoretical kinetic model.

4.5 Co-phase separation with periodic fueling

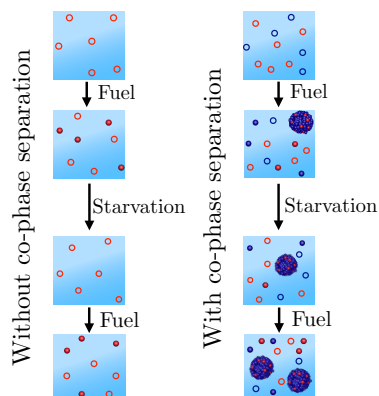


Fig. 4.9: Schematic representation of co-phase separation facilitating the survival of the product in repetitive fueling starvation experiments. The precursor in periodic fueling and starvation periods without (a) and with (b) competitor 2.

We tested how co-phase separation is affected when the system is subject to periodic fueling and starvation periods. We chose the amount of fuel and fueling frequency such that the product is depleted during each starvation period (Fig. 4.9). We hypothesize that competition with competitor 2 under the exact same conditions lets the product survive starvation (Figs. 4.9 and 4.10). Indeed, when we periodically fueled 50 mM precursor every 30 minutes with 60 mM of fuel, we found that the corresponding product completely hydrolyzed after each starvation period (Fig. 4.10(a)). In contrast, when we periodically fueled 50 mM precursor and 100 mM competitor 2 with the same amplitude and frequency, we observed that co-phase separation protected the product from hydrolysis and thereby helped it to survive starvation (Fig. 4.10(b)).

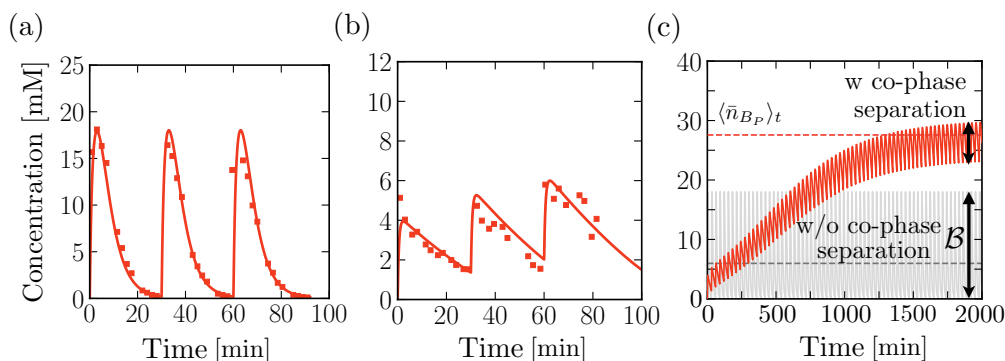


Fig. 4.10: Co-phase separation allows survival of parasite during periodic fueling. (a) Product when 50 mM precursor fueled with an amplitude of 60 mM EDC every 30 minutes. (b) 50 mM precursor and 100 mM competitor 2 fueled with an amplitude of 60 mM EDC every 30 minutes. Markers represent HPLC data; solid lines represent data calculated using the theoretical kinetic model. (c) Calculation using the theoretical kinetic model of long-time kinetics of the reaction cycle of the experiments in (a) and (b). The gray and red dashed lines represent the mean concentrations achieved at pseudo steady state without and with co-phase separation, respectively. Note that the oscillations around the pseudo steady state concentration are severely damped with co-phase separation.

Despite the competition and lower anhydride yield, the product's survival during the starvation period resulted in a drastically increased yield over fueling and starvation periods compared to a system without competitor 2 which did not show an increased yield. We used our theoretical kinetic model to calculate the system's response to hundreds of cycles (Fig. 4.10(c) and 4.11(a-b)).

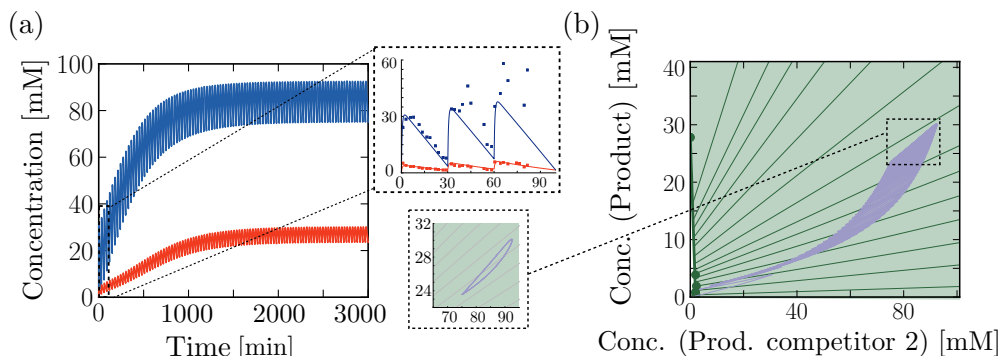


Fig. 4.11: Theoretical long-time behavior at periodic fueling. (a) Products when 50 mM precursor (red) and 100 mM competitor 2 (blue) fueled with an amplitude of 60 mM EDC every 30 minutes using the theoretical kinetic model of long-time kinetics of the reaction cycle of the experiments. Inset shows the first three refueling steps. Markers represent HPLC data; solid lines represent data calculated using the theoretical kinetic model. (b) The representation of the kinetic traces of (a) in the ternary phase diagram. At the pseudo steady state, the trace is a closed orbit (inset).

It is necessary to mention that this is a purely theoretical extension, given these long-time studies are not experimentally feasible as it can lead to fuel build-up (in case the products reach full turnover) or, in any case, the waste builds up, which is not ideal. We found that co-phase separation of the product with the anhydride product of competitor 2 resulted in a pseudo steady state of the product in which the concentration oscillated around a mean concentration ($\langle \bar{n}_{B_P} \rangle_t$) roughly 27 mM (red dashed line in Fig. 4.10(c)). In contrast, in the absence of competitor 2, the product oscillated around a mean concentration of roughly 6 mM. It did not show any increase in concentration over time (gray solid line in Fig. 4.10(c)).

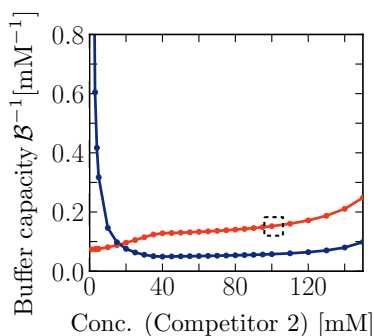


Fig. 4.12: The buffer capacity against fuel oscillations increases for the parasite with increasing host concentration. The highlighted value of buffer capacity corresponds to the case in Fig. 4.10(c) for 100 mM of competitor 2. Red (B_P) and blue (B_{C_2}).

These observations support the idea that the product of competitor 2 acts as a host, and the product of the precursor thus survives longer, benefitting like a parasite. Besides the anticipated result of survival in the presence of a host, we found a surprising new behavior, i.e., we observed that the oscillation in the concentrations in pseudo steady state due to fueling and starvation was dependent on the amount of competitor in the system (Fig. 4.10). Specifically, in the first experiment, the concentration oscillated between a maximum of 18 mM and a minimum of 0 mM, i.e., the concentration variation is 18 mM (Fig. 4.10(a) and gray solid line in Fig. 4.10(c)). In the experiment with competitor 2, this measure \mathcal{B} (max-min) had drastically decreased to just 3 mM when pseudo steady state was reached (red solid line in Fig. 4.10(c)). The concentration variation, \mathcal{B} was quantified by the theoretical kinetic model for in-

creasing competitor 2 concentrations and tended to decrease (Fig. 4.12). In other words, co-phase separation protects the products from hydrolysis and buffers against fuel-driven oscillations. A reminiscent observation was recently reported in a population of Hela cells where phase separation was shown [85].

Buffer capacity

The buffer capacity is defined as the inverse of the deviation in concentration, i.e., (\mathcal{B}^{-1}) increases for the parasite with the increasing competitor 2 (host) concentration. The propensity to co-phase separate increases in the system with increasing the host concentration, which allows for more protection of the parasite and, thus, less degradation. It leads to smaller deviations around the mean pseudo steady state concentration. The host's buffer capacity decreases, making it more susceptible to fluctuations. The blue and red solid lines in Fig. 4.12, represent the buffer capacity of the host and parasite, respectively. Initially, the buffer capacity of the host is high due to the lower mean concentration of the host and hence less deviation. As the mean concentration increases, the deviation around it also increases, thus reducing its buffer capacity. The opposite trend occurs for the parasite, up to 40 mM, following which the mean concentration of the product also increases due to the protection from the host droplets.

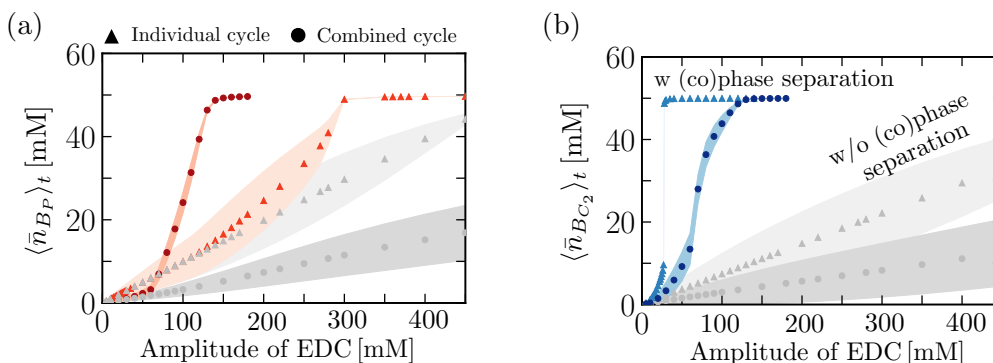


Fig. 4.13: (Co) Phase separation allows buffering of concentration. The triangle markers (colored) represent how, in their respective individual cycles at long time, the products' mean and deviation \mathcal{B} (shaded domain) changes with varying the amplitude of the fuel, EDC, keeping the periodicity of supply fixed to 30 mins. Given the lower solubility of the product of competitor two ((b) blue) compared to the product ((a) red), it reaches full turnover earlier with the least deviations. Co-phase separation in the combined cycle (circle markers) allows the product of competitor 2 to suffer and the product to benefit compared to the individual cycles (triangle markers). However, on theoretically suppressing (co) phase separation in both the individual and combined reaction cycles, we see the opposite effect, that neither manages to reach full turnover in the studied range of EDC amplitudes, and individual cycles benefit both because the competition for the fuel source is reduced.

4.6 Effects of activation rate constants on host-parasite identity

We have shown that the kinetic orbit of the average product concentrations in the phase diagram determines the lifetimes of the products and the composition inside droplets. The shape of the orbit is also affected by the rate constants. To illustrate this aspect, we

considered, precursor concentration of 50 mM and competitor 2 concentration of 100 mM fuelled with 100 mM EDC, as the experimental reference and swapped the rate constants related to the activation reaction pathway, i.e., $k_{1/2/3,i}$ (Fig. 4.14) to see if the host-parasite identity can be affected. This is purely a theoretical extension of the study, given that the reaction rate coefficients are chemical characteristics of the individual component and cannot be swapped.

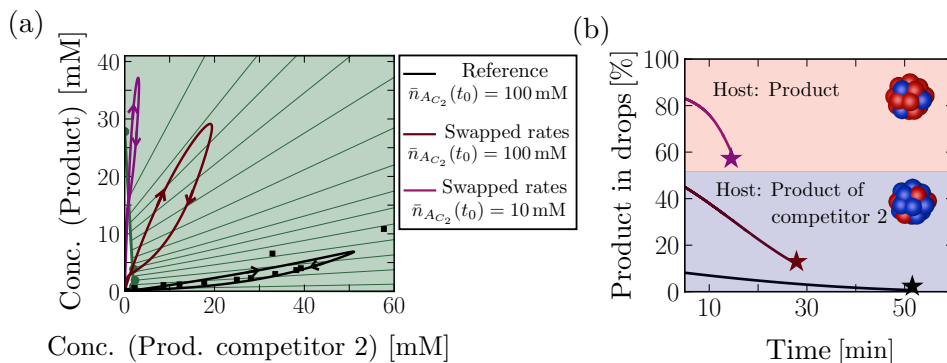


Fig. 4.14: Host and parasite identity depend on the solubilities of the components and initial precursor concentrations. (a) Kinetic orbits in the phase diagram correspond to three different parameter sets in which we swapped the rate coefficients of the fuel-driven activation pathway (i.e., all rate coefficients except for the deactivation rate coefficients) and considered different concentrations of competitor 2 at a fixed EDC concentration of 100 mM and precursor concentration of 50 mM. Markers represent HPLC data; solid lines represent data calculated using the theoretical kinetic model. (b) The ratio of the product of precursor in droplets over time shows that the identity of the host and parasite can change with swapped rates. Due to the higher solubility, the product is typically the parasite, except when it is in excess. In this case, the product starts as a host and transits to a parasite as long as droplets do not dissolve beforehand. The star markers denote the time point of droplet dissolution.

4.7 Summary

In this chapter, we first recorded the key observations from the experimental studies. Then we used the theoretical kinetic model developed to validate the observations and also extended it to predict certain novel behaviors. The key property of the system is the observation of exciting emergent trends that could be obviously predicted from merely the individual reaction cycles. Phase separation in the individual reaction cycles itself affected the observables in the study, i.e., the yield, lifetime, and buffering capacity. Additionally, co-phase separation in the combined cycle also affected these observables, usually benefitting the parasite component in all aspects while the host suffered.

Application of supramolecular systems chemistry here leads to observation of a few life-like traits, like, the consumption of chemical fuel to produce waste to sustain itself while demonstrating a host-parasite-like behavior. This leads to an incremental step in the bottom-up design of synthetic life using the systems chemistry pathway.

Chapter 5

Study of enzymatic kinetics in compartmentalized systems

"It doesn't matter how beautiful your theory is, it doesn't matter how smart you are. If it doesn't agree with experiment, it's wrong."

– Richard Feynmann

The motivation of this chapter lies in obtaining a minimalist description to understand biochemical reactions connected via intra and intercellular communication that lead to complex behaviors. The reactions are compartmentalized within cells and subjected to external signals due to communication with neighboring cells in the population, for example, by molecular diffusion [86]. To begin to reverse engineer the underlying architecture of network-based population behaviors, it is crucial to determine how compartmentalization will affect biochemical reaction rates in order to rationally design and build compartmentalized chemical reaction networks (CRNs).

The objective of this chapter is to apply the theoretical framework developed in chapter 3, with suitable modifications to take into account that the proteinosomes which form the compartments are not formed via phase separation but instead, by covalently linked protein-polymer conjugates thus serving as semi-permeable membrane-bound compartments that allow selective partitioning of components. Following this, we theoretically try to validate experimental observations and predict further trends in the chosen CRN's observables for this study in the presence and absence of compartmentalization.

The choice to study the PEN DNA reaction specifically is because utilizing the polymerase (P), exonuclease (E), and nickase (N) enzymes, it is ideally suited for building out-of-equilibrium information processing networks with different characteristics. Depending on the sequence of the DNA template strand, autocatalytic, linear, and inhibitory reactions can be programmed [87, 88, 89, 90]. For the purpose of this study, we focus on an autocatalytic characteristic. We proceed to characterize the reaction in buffer solution (in the presence and absence of exonuclease) for changing substrate DNA template concentrations corresponding to fixed primer DNA concentrations. We proceed to study the same in proteinosome populations of different number densities that attribute to different average substrate DNA template concentrations. We then try to address the question of how compartmentalization affects the observable, which is the rate of reaction as a function of template concentration. In this chapter, due to multiple species in the CRN, we represent the concentration of the i -th component, n_i as $[i]$ instead.

5.1 Autocatalytic reactions and their properties

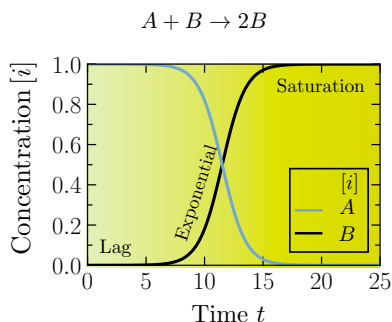


Fig. 5.1: Kinetic autocatalytic profiles. The kinetic profiles highlight the lag, exponential and saturation phases. The profile of the autocatalyst is sigmoidal. Parameters are listed in the L.O.F section.

Autocatalysis is a fascinating natural phenomenon in chemistry. From the most general definition of autocatalysis, that is, a process in which a chemical compound called autocatalyst can catalyze its own formation, several different systems can be described. There exist different categories of autocatalysis, and they can be compared based on their mechanistic, kinetic, and dynamic properties. Different systems of chemical reactions can generate autocatalytic patterns. With the notion of autocatalysis covering a large variety of mechanistic realizations with very similar behaviors, it is proposed that the key signature of autocatalysis is its kinetic pattern expressed in a mathematical form. The general definition of autocatalysis as a chemical process in which one of the products catalyzes its own formation

can be mathematically generalized as [91],

$$\frac{d}{dt}[i] = k(\{[j]\}) [i]^a + f(\{[j]\}), \text{ with } |k| \gg |f|, a > 0 \text{ and } k > 0, \quad (5.1)$$

where $\{[j]\}$ implies the set of concentrations of other components, except the autocatalyst, in the system, and k is the reaction rate coefficient.

We can use a straightforward example to demonstrate it, which is $A + B \rightarrow 2B$, for which the conserved quantity is, $\psi_1 = ([A]_0 + [B]_0)$. The mass-action kinetic equations are as follows,

$$\begin{aligned} \frac{d}{dt}[B] &= k[A][B] \\ &= k[B](\psi_1 - [B]) \\ &= k\psi_1[B] - k[B]^2, \end{aligned} \quad (5.2)$$

$$\implies [B](t) = \frac{\psi_1}{1 + \frac{(\psi_1 - [B]_0)}{[B]_0} \exp(-k\psi_1 t)}.$$

The appearance of sigmoidal characteristics, however, depends just on the parametric conditions (initial concentrations, rate coefficients) applied. It thus provides a simple means to decide whether the experimental system or the theoretical model has an autocatalytic feature or not: if the accumulation of a product speeds up its own formation, then the corresponding model or experimental system is indeed autocatalytic. If not, then the term autocatalysis may not be appropriately used by any means.

The regions in an autocatalytic profile are not sharply characterized. The lag phase can tentatively be the region where only a small fraction of the initial component is converted to the product; the exponential phase is the region starting from the lag phase to the bend-

ing point of the sigmoidal curve where the acceleration of the reaction rate is obvious. The saturation phase is the region from the bending point to the completion of the reaction. Since many experimental autocatalytic systems are exponential and substrates are always in limited supply in experiments, sigmoidal kinetics is usually expected from autocatalytic reactions and is the first experimental signature of autocatalysis. Nevertheless, other processes, like the accumulation of an intermediate, can cause a lag phase. Thus, to prove the autocatalytic nature of a reaction, we need to verify that its rate increases with the addition of products. This is usually done by measuring the initial reaction rate with increasing initial concentrations of products.

5.2 PEN DNA mass action kinetics

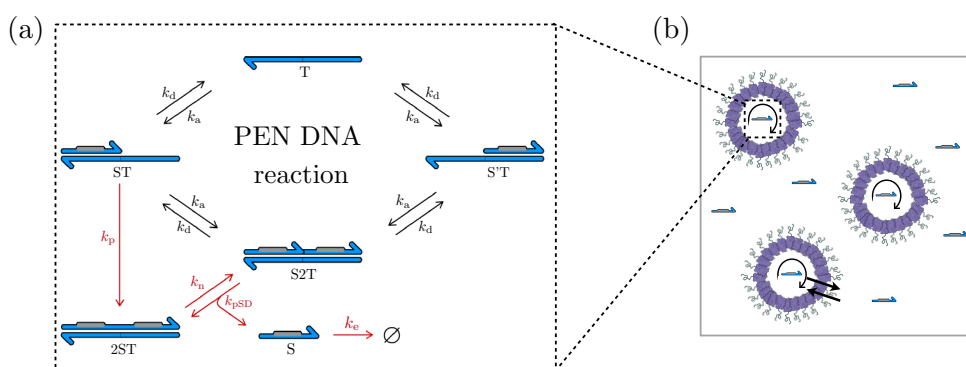


Fig. 5.2: Schematic representation of the autocatalytic PEN DNA reaction and encapsulation in proteinosomes. (a) General description of PEN DNA reaction, (1) primer S binds to its complementary template T; (2) polymerization by the polymerase (P) of S along T or via strand displacement S binds in the wrong position, followed by nicking with nickase (N) to produce 2S, (3) dissociation of 2S from the template T. (4) Degradation of S by exonuclease (E) inside and outside the proteinosome maintains an out-of-equilibrium state for the system. (b) Schematic of compartmentalized PEN DNA reactions. Template DNA (T) is encapsulated within the water-in-water proteinosomes. Substrate/primer DNA (S); dNTPs; polymerase, exonuclease, and nickase enzymes are loaded outside of the proteinosome and diffuse into the proteinosomes to initiate the reaction. For T and S sequence details, please refer to Ref. [90].

In buffer solution

First, the reactions are studied and characterized in the buffer solution (composition in detail in Appendix. G), which is also considered the reference system in this case. The fuel, i.e., the limiting reactant in the system, are the dNTPs, which are provided in excess since they are the basic monomers for the polymerization process. Running out of dNTPs will prevent any polymerization process, leading to a gradual degradation of all the dynamic DNA species by the exonuclease and, ultimately, to a flat fluorescence curve. The main purpose of the reaction buffer is to provide suitable working conditions for the three enzymes and therefore contains a consensual amount of mono- and bivalent ions. It is worth noting that this reaction is susceptible to the formation of so-called "parasites" which typically contain long AT repeats, interspaced by sequences that serve as a target for the restriction enzyme (nickase) present in the buffer. It has been studied that Netropsin

(added in the buffer) at a concentration of a few μM tends to delay the development of such species in a contaminated experiment while having, at most, a marginal effect on the DNA reaction network. It is possible that Netropsin locally stabilizes such AT-rich parasites and inhibits their polymerase-dependent growth. However, this phenomenon is not investigated in depth.

The kinetic equations describing the scheme are as follows,

$$\begin{aligned}
 [\dot{S}] &= -k_a(2[S][T] + [S][ST] + [S][S'T]) - k_e[S] + k_d([ST] + [S'T] + 2[S2T]) + k_{pSD}[S2T] \\
 [\dot{T}] &= -2k_a[S][T] + k_d([ST] + [S'T]) \\
 [\dot{ST}] &= -k_a[S][ST] - k_d[ST] - k_p[ST] + k_a[S][T] + k_d[S2T] \\
 [\dot{S'T}] &= -k_a[S][S'T] - k_d[S'T] + k_a[S][T] + k_d[S2T] \\
 [\dot{2ST}] &= -k_n[2ST] + k_p[ST] + k_{pSD}[S2T] \\
 [\dot{S2T}] &= -2k_d[S2T] - k_{pSD}[S2T] + k_a([S][ST] + [S][S'T]) + k_n[2ST].
 \end{aligned} \tag{5.3}$$

The conserved quantity in this reaction scheme is the net template concentration, i.e., $\psi_1 = ([T] + [ST] + [S'T] + [2ST] + [S2T])$.

We observe that indirectly through the interwoven pathways, the reaction has signatures of an autocatalysis process, falling under the classification of template autocatalysis with an intermediate [91].

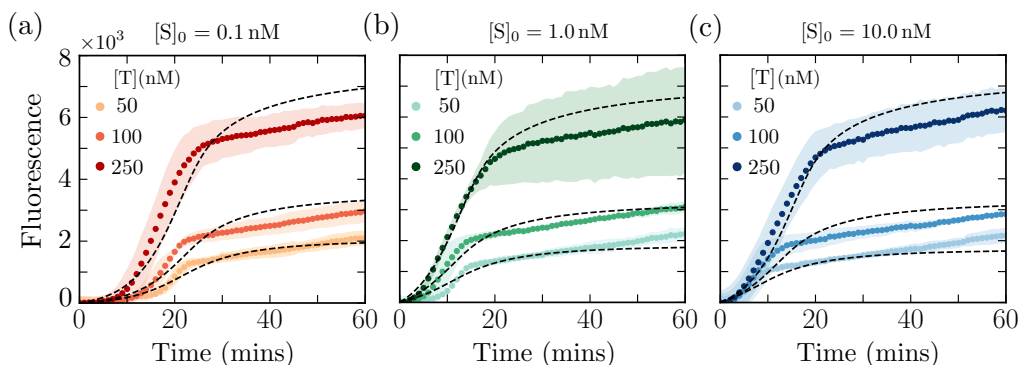


Fig. 5.3: Readout of total primer kinetic profile in the absence of degradation. $[S]_{\text{tot}}$ readout in the form of fluorescence at different average template concentrations for initial primer concentrations (a) 0.1 nM, (b) 1.0 nM, and (c) 10 nM, in the absence of the exonuclease enzyme. The fluorescence does not saturate and has a low, increasing slope as a result. It is evident that for higher template concentrations, the maximum value reached is highest and set by the template concentration since it does not appear to vary with the initial primer concentration. Markers represent experimental data, and dashed black lines represent data from the theoretical model.

We now proceed to solve the set of six coupled ordinary differential equations to obtain the concentrations of the different species. The calibration curve to convert the total concentration of the primers ($[S]_{\text{tot}} = ([S] + [ST] + [S'T] + 2 \times ([2ST] + [S2T]))$), to the fluorescence of Eva-green is given in Appendix. H. The autocatalytic profiles are studied both in the absence and presence of exonuclease enzyme (Figs. 5.3 and 5.4, respectively).

Inside proteinosomes

The reactions proceed only in the proteinosomes, given the template DNA (T) is encapsulated within them. The only reaction that can proceed outside proteinosomes is the degradation mediated by the exonuclease enzyme. The semi-permeable membrane of the compartments allows the free diffusion of all the enzymes and the primer DNA (S). The primer partitions equally in the system, implying its partition coefficient is unity. The diffusion of the components is fast compared to the time scales of the reactions, and therefore the evolution of the reaction kinetics occurs homogeneously inside the compartment. The calibration of the concentrations inside proteinosomes varies from the buffer solution (details in Appendix. H).

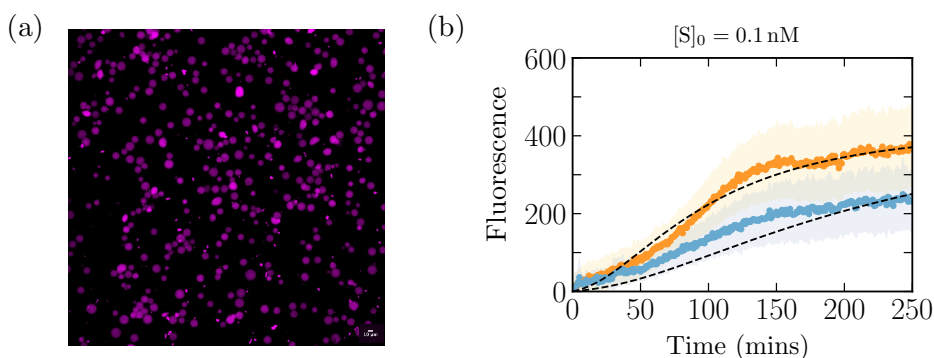


Fig. 5.4: Characterisation of PEN DNA reaction in proteinosome. (a) The field of view in the template DNA channel, where the AF594 signal was used to localize proteinosome. The proteinosome population here corresponds to 78 proteinosomes, each of average radius $7.03 \mu\text{m}$ and the total proteinosome volume in the system is $NV^I = 7.08 \times 10^{-4} \mu\text{L}$. (b) The autocatalytic profiles as a readout of total primer concentration in the proteinosome system without exonuclease. The template concentration is fixed inside each psome. The effective average template concentrations are $[\bar{T}] = 0.163 \text{ nM}$ (orange markers), $= 0.074 \text{ nM}$ (blue markers), by varying N . Markers represent experimental data, and dashed black lines represent data from the theoretical model.

The template concentration inside each proteinosome is constant ($[T]^I = 924 \text{ nM}$), and therefore to vary the average template concentration ($[\bar{T}]$) in the system, we change the number density of proteinosomes in a fixed volume $[\bar{T}] = (NV^I/V)[T]^I$, where N is the number of proteinosomes in the system. Given there is a narrow distribution of the proteinosome's radii due to bulk preparation, [30], here we use the average proteinosome radius as $7.03 \mu\text{m}$ and $8.49 \mu\text{m}$ (corresponding to orange and red data in Fig. 5.4(b) representing two different proteinosome populations, with different average radii). The total volume in the system is $4 \mu\text{L}$. In this study, we ensure that when we evaluate the total primer concentration for applying the calibration coefficients to obtain the fluorescence, we use the volume-weighted average concentrations of each species.

The kinetic mass action equations describing the evolution of the average primer concen-

tration and all other species inside the proteinosome are as follows,

$$\begin{aligned}
 \dot{[S]} &= \frac{NV^I}{V} \left(-k_a^I(2[S]^I[T]^I + [S]^I[ST]^I + [S]^I[S'T]^I) - k_e^I[S]^I + k_d^I([ST]^I + [S'T]^I + 2[S2T]^I) \right. \\
 &\quad \left. + k_{\text{pSD}}^I[S2T]^I \right) - \frac{(V - NV^I)}{V} (k_e^{II}[S]^{II}) \\
 \dot{[T]}^I &= -2k_a^I[S]^I[T]^I + k_d^I([ST]^I + [S'T]^I) \\
 \dot{[S'T]}^I &= -k_a^I[S]^I[ST]^I - k_d^I[ST]^I - k_p^I[ST]^I + k_a^I[S]^I[T]^I + k_d^I[S2T]^I \\
 \dot{[S'T]}^I &= -k_a^I[S]^I[S'T]^I - k_d^I[S'T]^I + k_a^I[S]^I[T]^I + k_d^I[S2T]^I \\
 \dot{[2S'T]}^I &= -k_n^I[2S'T]^I + k_p^I[ST]^I + k_{\text{pSD}}^I[S2T]^I \\
 \dot{[S2T]}^I &= -2k_d^I[S2T]^I - k_{\text{pSD}}^I[S2T]^I + k_a^I([S]^I[ST]^I + [S]^I[S'T]^I) + k_n^I[2S'T]^I.
 \end{aligned} \tag{5.4}$$

5.3 Proteinosomes affect the PEN DNA reactions

On globally fitting the data, we already observe (Appendix. H) that the reaction rate coefficients are significantly high in the compartments. It is important to note that we have simplified here the Michaelis-Menten enzymatic kinetics of each enzyme and used an effective reaction rate coefficient for each enzymatic step. It is a plausible explanation that the physicochemical environment within the proteinosome is different compared to the buffer, leading to alterations in the reaction rate coefficients k_α .

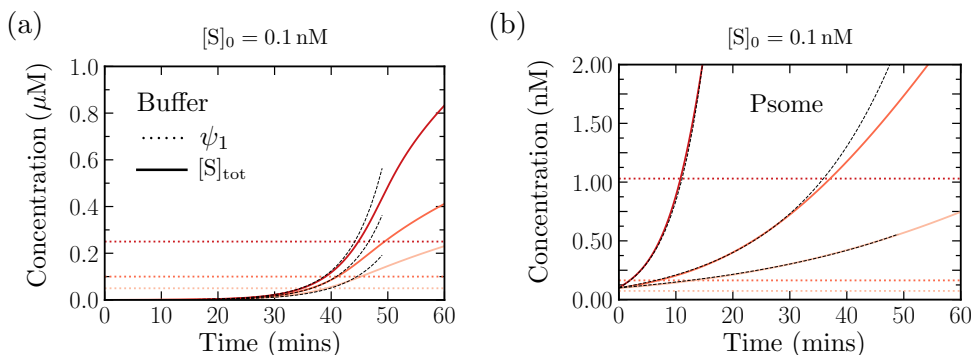


Fig. 5.5: Compartmentalization affects the rate of autocatalysis. For fixed initial primer concentration, (a) in the buffer, we fit the initial rate of autocatalysis for different template concentrations, and we do the same (b) in the proteinosome system to characterize how compartmentalization affects the rate of formation of the primers in the total system. The highest average template concentration is theoretically chosen as 1.03 nM, given experimental data was only available for the lower two sets as in Fig. 5.4. The black dashed lines denote the fits. Please note that the systems studied here are without exonuclease.

We use the function $f(t) = a(-1 + \exp(rt))$ to fit the initial rate in the exponential regime of the autocatalytic profile and then record the fitted values in Appendix. H. The observable that we define to compare between the buffer system and psome system is how the rate r varies with template concentration, $dr/d[\bar{T}]$. Using 3 data points to calculate the observable is not optimal. We proceed with it nevertheless to get a quantitative predic-

tion, and we find that the observable is $\times 600$ higher in the proteinosome system, implying compartmentalization leading to localization of the reactions, allowing higher rates of autocatalysis for changing template concentration. This increase is over an order of magnitude higher and qualitatively agrees with observations made in Ref. [90]. The reason behind this is two-fold, an increase of the reaction rate coefficients inside the proteinosomes, and the templates are localized in small compartments and hence are not diluted as it happens in the buffer.

A major difference between compartments formed via phase separation and proteinosomes is that the constraints due to phase equilibrium are not imposed on the reactants here, given there exists a semi-permeable membrane. That leads to high reaction rates inside the proteinosome, not only due to increased reaction rate coefficients (discussed in chapter. 2) but also due to the increased local concentration of template and other species inside.

5.4 Summary

Taken together, our results show that similar reaction rates are obtainable in buffer and proteinosomes with an order of magnitude difference in the total template concentrations in the proteinosomes (nM) compared to the buffer (μM). One explanation for this observation could be that the local template concentration in the porous proteinosome is high, and the DNA produced from the reaction can diffuse away from the reaction center. The rate of reaction as a function of template concentration is increased by more than an order of magnitude compared to buffer as the local build-up of primer is prevented, thus relieving product inhibition. Our results show that spatial compartmentalization with free diffusion of substrates and products offers several kinetic advantages compared to reacting in the buffer. This includes increased and tuneable reaction rates based on varying the template and enzyme concentrations. Overall, the results show that compartmentalization plays a strong role in altering reaction landscapes, indicating that reaction networks based on PEN DNA will have different behaviors in the buffer. There is further scope in this work, where one can explore how the degradation is controlled in the two systems and possibly observe how easily tuneable it is in proteinosomes instead of buffer solution. This control in designing the reactions in compartments to tune communication among proteinosomes which occurs via diffusion of the primer and enzyme components allows using synthetic biology tools to design synthetic life, which possesses the properties of consuming fuel (dNTPs in this case), replicating and communication in the proteinosome populations, via diffusion.

Chapter 6

Conclusion and Outlook

In this work, we had proposed to tackle the question of how chemical reactions could be controlled by compartmentalization. Compartmentalization, in this context, meant not only membrane-less compartments formed via phase separation but also semi-permeable compartments like proteinosomes. We started by laying the groundwork by introducing the thermodynamic framework to understand the phenomena of phase separation and chemical reactions separately. With respect to the theory of phase separation, we used the Flory-Huggins theory, which is widely used still and has been successful, largely, in describing the thermodynamics of polymer solutions.

It has some limitations, namely, one being its applicability only to solutions that are sufficiently concentrated that they have uniform segment density. The other assumptions and limitations of the theory are discussed in Ref. [5], and the applicability of Flory-Huggins, mainly for biochemical applications, is discussed in Ref. [92]. We also discussed how beyond mean-field theories can be used viz., random phase approximation [49, 50], to account for sequence dependence of interactions leading to phase separation. This avenue is interesting to explore, given biological examples of intrinsically disordered proteins that undergo phase separation *in vivo*, besides having a disordered region, which is already challenging to model, has additional modular binding domains, and these binding motifs that also give rise to specific multivalent, solvent-mediated interactions. The proteins' amino acid sequences entail the properties of the interactions. There has been promising work in this direction in the group of Prof. Hue Sun Chan, affiliated with the University of Toronto.

After discussing phase separation and, in its context, construction, and interpretation of phase diagrams and then chemical reactions as two orthogonal phenomena, we then combined the two processes to discuss what thermodynamic equilibrium conditions dictate in a system undergoing the two processes simultaneously (chapter 1). Following discussions on equilibria, we discussed the dynamical equations that govern the system's relaxation to the thermodynamic equilibrium.

In chapter 2, we introduced dynamical equations for the volume fractions of components and phase volumes in phase-separated systems with chemical reactions. These phase-separated compartments are formed due to the fast diffusion of components, allowing us to consider the equilibrated phases to be homogeneous. In this framework, diffusion is interpreted as an exchange flux between compartments that can grow and shrink in size. Thus, ordinary differential equations are sufficient for describing these systems. We

apply this framework in chapter 4, where the reactions are not diffusion-limited. These equations also reveal why merely up-concentrating components in the solvent-poor compartment does not necessarily lead to an increased reaction rate, as expected from classical mass-action laws in dilute systems. In other words, an increase in the local volume fraction of a reactive component due to phase separation does not necessarily lead to an increase in the rates of reactions in which it participates. Here, the reaction rate coefficients play a key role in solely determining the speed-up or slow-down of reactions in each phase. These insights might be applicable to explain recent observations of increased/decreased enzymatic reaction rates in coacervate [64, 66, 65].

We introduce here how chemical reactions can be driven out of equilibrium and show how non-equilibrium steady states can exist in these systems when chemical reactions are driven differently between the phases. To illustrate these non-equilibrium states in the phase diagram, we introduce the tie line selecting curve, which establishes a connection between the conserved quantities in the system and the chosen phase equilibrium. An extension to this study could involve investigating the role of interfacial resistance in these systems where chemical reactions occur. The interface in our study always equilibrates instantaneously, but that need not necessarily be the case always.

In chapter 3, we specifically look into systems where the reactive client components are dilute and do not affect the phase separation properties in the system, which is then usually set by the non-dilute non-reactive components, the scaffold, and the solvent. This demarcation among components based on their abundance and role in the system offers some simplicities in tackling the problem. We first establish the dilute limit of the reactive components and how all thermodynamic parameters are affected by this limit. We provide a theoretical bound below which the dilute approximation holds as a function of the free energy parameters. We provide here the dynamic equations for the scaffold and clients in the continuum model, the thin interface limit, and in the limit of infinite diffusion. For the continuum model, it is effectively a diffusion in a potential for the clients, which is set by the scaffold volume fraction spatial profile. For the thin interface model, it is a coupled reaction-diffusion problem in the two phases, which are coupled by the boundary conditions at the phase boundary. Finally, for the infinite diffusion limit, the ordinary differential equations mimic the dilute mass action kinetic equations.

After settling on the framework, we proceed to answer questions about optimizing observables of certain chemical reactions, like the relative yield at steady state for a unimolecular and bimolecular process. We explain the possible reference systems to which we can compare, and we choose one in which the compartment doesn't exist, allowing better investigation of how phase-separated compartments affect chemical reactions. For the nucleation process, the observable is the relative initial rate of the reaction. We conclude from this study that these observables can be optimized as a function of the compartment volume. Additionally, thermodynamic parameters like partition coefficients and kinetic parameters like reaction rate coefficients or external energy in the phases can tune this. The necessary

ingredient required for the observation of optimality is non-linearity in the reaction rates. This study can possibly help in engineering reactions in phase-separated compartments to optimize certain observables as an experimentalist would choose to define in their system. In chapter 4, we use the theoretical tools developed in earlier chapters to understand a systems chemistry experimental study. This study not only highlights emergent properties of chemical reactions and phase separation but also shows how phase separation (we use the term co-phase separation in this chapter to imply the same) controls observables of the reaction cycles like yield, the lifetime of building blocks, and buffering capacity of building blocks against fluctuations in fuel concentrations. We see that phase separation allows a parasite-like building block to survive longer than it would when it existed by itself due to the protection mechanism offered in the system by a host-like building block while competing for fuel resources. This property could be crucial for the control of downstream chemical reactions of the competitors. We unravel the mechanisms allowing this by using the theoretical model developed, which also allows us to make further predictions on what leads to identification as a host or parasite entity and explore the buffering capacity of the building blocks against periodic and Poissonian fueling of the system. Our results demonstrate that parasitic behavior can already emerge in a simple non-equilibrium system that can phase separate and is controlled by fuel-driven chemical reaction cycles. Our understanding of the underlying mechanism can be a step toward the design of more complex, synthetic life-like systems. In the future, one can explore how co-phase separation affects the selection of many chemically active molecules.

In the final chapter, we take up another experimental study, now using synthetic biology components, with the broad goal of designing synthetic cell-like behavior by allowing communication between compartments that are no longer formed via phase separation but are still micro-droplets, based on bovine serum albumin and glucose oxidase conjugated to PNIPAAm chains (details in Appendix. G), called proteinosomes. However, within the broad goal, it still involves the control of a chemical reaction network when compartmentalized in such proteinosomes. Similar to before, we characterize the reaction network in a buffer solution (reference system, without compartments) and then proceed to investigate its properties in the encapsulated proteinosomes, which only allow partitioning of the enzymes and the primer DNA (which is the substrate and product; given it is an autocatalytic process). The reaction then wholly proceeds inside the compartment. We observe that the kinetic coefficients are different compared to the reference due to the physico-chemical environment inside being a bit crowded. In this study, besides the reaction rate coefficients, the up concentration of most species just being localized inside leads to an increased readout of the observable, which is the rate of change of rate of autocatalysis (obtained by fitting the exponential regime) with respect to varying template concentrations.

Our study shows that we can use localized chemical reactions based on PEN DNA reactions within proteinosomes, where the proteinosomes encapsulate the template DNA code for specific reactions (in this case, it was autocatalysis, but could be an inhibitor,

oscillator, etc). The addition of enzymes greatly facilitates the ability to drive the systems into an out-of-equilibrium state. Compartmentalization also offers the ability to spatially localize, alter reaction kinetics and reduce the total amount of DNA templates required for the reaction. Coupled with the coding ability of DNA, this medium allows access to a large combinatorial space. The PEN DNA toolkit opens many possibilities for spatial multiplexing using a flexible and modular system, thus providing a general route for building synthetic compartmentalized reaction networks based on reaction-diffusion mechanisms and a minimal number of components.

Whilst it is still a challenge to investigate the effect of compartmentalization in biological cellular systems, the ability to build micron-sized compartments encapsulating enzyme reactions has offered a unique possibility to address this challenge without biological complexity. This work depicts an important step in bottom-up synthetic biology approaches by combining them with quantitative approaches. Our results show that it is crucial that biological behaviours based on networks of chemical reactions have to be considered within the context of compartmentalization. Simplified physical models of compartments are ideal for exploring these fundamental questions. Moreover, these minimal models could be effective as physical models of biological compartmentalization where membrane-bound compartments which contain reactions allow the passive diffusion of molecules such as in mitochondria.

In this work, we hope to have provided in the first part the essential theoretical framework which can be used and built upon to tackle chemical reactions in compartments and to have convinced the reader with the second part, the various applications of compartmentalized chemical reactions in designing synthetic life.

Appendix A

Free energy calculations for block charged polymers using RPA

RPA formalism

Bare Correlations

RPA theory neglects all but the trivial zeroth-order and two-body correlation of density fluctuation. The state of the system is completely parametrized by the spatially varying densities $\rho^{(i)}(\mathbf{r})$ where i labels different monomer types ($i = m, c, s$ represents monomers in the charged polyampholyte of length N , counterions, and salt, respectively), the following form of the partition function [49, 50],

$$\mathcal{Z} = \int \mathcal{D}|\rho_k\rangle \exp\left(-\frac{1}{2V} \sum_{k \neq 0} \langle \rho_{-k} | \hat{\mathcal{A}}_k | \rho_k \rangle\right), \quad (\text{A.1})$$

as a path integral over all density profiles in terms of their Fourier-transformed fluctuations. Here k is the wave number (for all three dimensions of reciprocal space of volume V). In the representation $|\rho_k\rangle_i \equiv \rho_k^{(i)}$, and the matrix $\hat{\mathcal{A}}_k$ accounts for two-body interactions between Fourier-transformed densities $\rho_k^{(i)}$ and $\rho_k^{(j)}$. The path integral is over all monomer types and over all wave numbers except $k = 0$, because it is a constant representing the total number of type- i monomers that does not affect density fluctuation,

$$\mathcal{D}|\rho_k\rangle = \prod_{i=1}^m \prod_{k \neq 0} d\rho_k^{(i)} \quad (\text{A.2})$$

In the case of purely geometric interactions like chain connectivity, we have $\hat{\mathcal{A}}_k = G_k^{-1}$ where G_k is the bare two-body correlation matrix, itself defined as,

$$V \left(\hat{G}_k \right)_{ij} = \langle \rho_k^{(i)} \rho_{-k}^{(j)} \rangle, \quad (\text{A.3})$$

where multiplication with V is due to translational invariance. The form of \hat{G}_k used in main text (Eq. (1.8f)) is motivated by assuming there exist no monomer-ion correlations setting all matrix elements of \hat{G}_{MI} and \hat{G}_{IM} to zero. Only the monomer-monomer correlation matrix calculated using the structure factor of Gaussian chain [48] and the ion-ion self-

correlation matrix $\hat{\rho}_I$ which is effectively a (2×2) diagonal matrix,

$$\hat{\rho}_I = \begin{pmatrix} \rho_+ & 0 \\ 0 & \rho_- \end{pmatrix} \quad (\text{A.4})$$

where ρ_{\pm} are the densities of positive and negative ions, $(\rho_+, \rho_-) = (\rho_s + \rho_c, \rho_s)$ or $(\rho_s, \rho_s + \rho_c)$, when the net charge on the charged sequence is respectively, negative or positive, to establish electroneutrality.

Electrostatic interaction as a perturbation

In the RPA theory of electrostatic interactions, it is assumed that the Gaussian chain geometry remains a good approximation. The inter-monomer interactions beyond the geometric ones are treated as a perturbation. The perturbative effect on the partition function of an interaction matrix \hat{U}_k can be calculated as the average of $\exp(-\hat{U}_k)$ over all Gaussian chain configurations,

$$\mathcal{Z}_u = \frac{\int \mathcal{D}|\rho_k\rangle \exp\left(-\frac{1}{2V} \sum_{k \neq 0} \langle \rho_{-k} | (\hat{G}_k^{-1} + \hat{U}_k) | \rho_k \rangle\right)}{\int \mathcal{D}|\rho_k\rangle \exp\left(-\frac{1}{2V} \sum_{k \neq 0} \langle \rho_{-k} | \hat{G}_k^{-1} | \rho_k \rangle\right)} \times \exp\left(-\frac{1}{2V} \langle \rho_{k=0} | \hat{U}_{k=0} | \rho_{k=0} \rangle\right) \equiv \mathcal{Z}_u^1 \mathcal{Z}_u^2 \quad (\text{A.5})$$

The neutrality of the system forces $\mathcal{Z}_u^2 = 1$ and Gaussian integrations on the path integrals in Eq. (A.5) yield,

$$\frac{1}{\mathcal{Z}_u^1} = \frac{\prod_{k \neq 0} \sqrt{\det(\hat{G}_k^{-1} + \hat{U}_k)}}{\prod_{k \neq 0} \sqrt{\det(\hat{G}_k^{-1})}} = \prod_{k \neq 0} \sqrt{\det(1 + \hat{G}_k \hat{U}_k)}. \quad (\text{A.6})$$

Recalling $f_{int} = f_{el} = -(\nu_0)^3/V \ln \mathcal{Z}_u^1$ for Coulombic interactions, calculated as the logarithm of $\mathcal{Z}_u = \mathcal{Z}_u^1$ per lattice site, we obtain,

$$f_{el} = \frac{(\nu_0)^3}{2V} \sum_{k \neq 0} \ln [\det(1 + \hat{G}_k \hat{U}_k)]. \quad (\text{A.7})$$

This summation is translated to an integral to obtain Eq. (1.8e). In the expression for the Coulomb interaction in k -space, the column vector $|q\rangle$ of monomeric and ionic charges contains $q_i = \sigma_i$, $1 \leq i \leq N$ and $q_{N+1} = 1$, $q_{N+2} = -1$ as components. Using Sylvester's identity: $\det(\hat{I}_a + \hat{X}\hat{Y}) = \det(\hat{I}_b + \hat{Y}\hat{X})$, where \hat{X} and \hat{Y} are respectively $a \times b$ and $b \times a$ matrices, provides the simplification from Eq. (A.7) to the form,

$$\det(1 + \hat{G}_k \hat{U}_k) = 1 + \lambda(k) \langle q | \hat{G}_k | q \rangle = 1 + \lambda(k) \left(2\rho_s + \rho_c + \frac{\rho_m}{N} \langle \sigma | \hat{G}_M(k) | \sigma \rangle \right) \quad (\text{A.8})$$

An investigation into the details of the replacement of the trace term remains, otherwise in conclusion, we obtain,

$$f_{el} = \int \frac{d\tilde{k} \tilde{k}^2}{4\pi^2} \left[\frac{1}{\eta} \ln[1 + \eta \mathcal{G}(\tilde{k})] - \mathcal{G}(\tilde{k}) \right] \quad (\text{A.9})$$

where $\eta = (b/\nu_0)^3$, T^* is the reduced temperature defined in the main text (Eq. (1.9)) and,

$$\mathcal{G}(\tilde{k}) = \frac{4\pi}{\tilde{k}^2[1 + \tilde{k}^2]T^*} \left(2\phi_s + \phi_c + \frac{\phi_m}{N} \langle \sigma | \hat{G}_M(\tilde{k}) | \sigma \rangle \right). \quad (\text{A.10})$$

For highly regular sequences studied in Subsection. 1.2.2, the RPA contribution from \hat{G}_M can be calculated by summing all block elements with alternating \pm weight factors, leading to,

$$\begin{aligned} \langle \sigma | \hat{G}_M(k) | \sigma \rangle &= n \hat{G}_M^{\text{block}}(k)_{\alpha\alpha} + 2 \sum_{\beta=1}^n \sum_{\alpha=\beta+1}^n (-1)^{\alpha-\beta} \hat{G}_M^{\text{block}}(k)_{\alpha\beta} \\ &= N \left[\sigma \frac{1+\theta}{1-\theta} - \frac{1}{L} \frac{4\theta}{(1-\theta)^2} \left(\frac{1-\theta^{L\sigma}}{1+\theta^{L\sigma}} \right) \right] \\ &\quad + \frac{2\theta}{(1-\theta)^2} \left(\frac{1-\theta^{L\sigma}}{1+\theta^{L\sigma}} \right)^2 (1 - (-1)^n \theta^{N\sigma}), \end{aligned} \quad (\text{A.11})$$

where $\theta = \exp(-(kb)^2|i-j|/6\sigma)$. Using the formula above, we calculate total free energy for globally neutral charged polymers in a salt, counterion-free solution (effective binary solution) as defined in the main text (Eq. (1.8)) and then numerically compute the derivatives to satisfy conditions as in Eq. (1.17) to obtain the binodal in the phase diagrams for varying sequence parameters in Fig. 1.7.

Appendix B

Numerical Methods

Chapter 1: Spectral method for modified Cahn-Hilliard dynamics

The transient snapshots used in Fig. 1.8 are obtained by solving the dynamic equation (Eq. (1.21)) in a 2D box (256×256) geometry subject to periodic boundary conditions for binary ($L = 2$) system with dissimilar molecular volumes ($\nu_0 = 1$ and $r_1 = 2$). The spatial part is dealt with using the spectral method with a snippet shown below for dealing with the non-linear terms, and the time stepping is done using exponential time differencing-RK4 (ETDRK4) [93]

```
1: procedure SPECTRAL
2:   def nonlinear term( $\hat{c}$ ) :
3:      $c = \text{irfft2}(\hat{c})$ 
4:      $\epsilon = 0.0000001$ 
5:      $c[c > 1] = 1.0 - \epsilon$ 
6:      $c[c < 0] = \epsilon$ 
7:      $\chi_{01} = 2.5$ 
8:      $\kappa = 3.0$ 
9:      $\hat{\mu} = \text{rfft2}(-1 + \text{np.log}(c) - 2 * \text{np.log}(1.0 - c) + 2 * \chi_{01} * (1.0 - 2.0 * c))$ 
10:     $m = 1.0 * c * (1.0 - c)$ 
11:     $k = k_x^2 + k_y^2$ 
12:     $\vec{x} = \text{rfft2}(\text{irfft2}(1j * k_x * (\hat{\mu} + \kappa * k * \hat{c})) * m)$ 
13:     $\vec{y} = \text{rfft2}(\text{irfft2}(1j * k_y * (\hat{\mu} + \kappa * k * \hat{c})) * m)$ 
14:    return  $1j * k_x * \vec{x} + 1j * k_y * \vec{y}$ 
```

Chapters 2 and 4: Finite difference to solve reaction kinetics at phase equilibrium

We obtain the evolution equation of the average volume fraction $\bar{\phi}_i$ using Eqs. (2.3a) and (2.3b)

$$\begin{aligned}
\frac{d}{dt}\bar{\phi}_i &= \frac{1}{V} \left[(\phi_i^I - \phi_i^{II}) \frac{d}{dt} V^I + V^I \frac{d}{dt} \phi_i^I + V^{II} \frac{d}{dt} \phi_i^{II} \right] \\
&= \frac{1}{V} \left[(\phi_i^I - \phi_i^{II}) \frac{d}{dt} V^I + V^I \left(s_i^I - j_i^I - \frac{\phi_i^I}{V^I} \frac{d}{dt} V^I \right) \right. \\
&\quad \left. + V^{II} \left(s_i^{II} - j_i^{II} - \frac{\phi_i^{II}}{V^{II}} \frac{d}{dt} V^{II} \right) \right] \\
&= \frac{V^I}{V} (s_i^I - j_i^I) + \frac{V^{II}}{V} (s_i^{II} - j_i^{II})
\end{aligned} \tag{B.1}$$

We use the relation, $j_i^I V^I = -j_i^{II} V^{II}$ in the last expression to obtain,

$$\frac{d\bar{\phi}_i}{dt} = \frac{V^I}{V} s_i^I + \frac{V^{II}}{V} s_i^{II} \tag{B.2}$$

Chemical kinetics via determining the diffusive rates $j_i^{I/II}$ between coexisting phases

For a system with two coexisting phases with $(L + 1)$ components, the time evolution is described by $(2L + 2)$ equations of form Eq. (2.3a), for the $(L + 1)$ concentrations in each phase, and the kinetics of the phase volumes Eq. (2.3b). Therefore, we must solve in total $(2L + 4)$ equations. Expanding Eq. (2.5) and using Eq. (2.3a) and Eq. (2.3b) in it, we obtain for the L.H.S,

$$\frac{d}{dt}(\gamma_i^I \phi_i^I) = \gamma_i^I (s_i^I - j_i^I - \phi_i^I \sum_{k=0}^L (s_k^I - j_k^I)) + \phi_i^I \sum_{k=0}^L \frac{\partial \gamma_i^I}{\partial \phi_k^I} \left(s_k^I - j_k^I - \phi_k^I \sum_{l=0}^L (s_l^I - j_l^I) \right). \tag{B.3}$$

For volume-conserving reactions, we can promptly use the condition $\sum_i s_i^{I/II} = 0$ in the above expression. The expression obtained above is linear in j_i^I and we can therefore proceed to collect the coefficients of j_i^I and j_l^I with $l \neq i$ as follows,

$$\begin{aligned}
\frac{d}{dt}(\gamma_i^I \phi_i^I) &= j_i^I \left[\gamma_i^I (\phi_i^I - 1) + \phi_i^I \left(\Xi_i^I - \frac{\partial \gamma_i^I}{\partial n_i^I} \right) \right] + \sum_{\substack{l=0 \\ l \neq i}}^L j_l^I \left[\gamma_i^I \phi_i^I + \phi_i^I \left(\Xi_i^I - \frac{\partial \gamma_i^I}{\partial \phi_l^I} \right) \right] \\
&\quad + \left[\gamma_i^I s_i^I + \phi_i^I \sum_{k=0}^L \frac{\partial \gamma_i^I}{\partial \phi_k^I} s_k^I \right],
\end{aligned} \tag{B.4}$$

where we abbreviated $\Xi_i^{I/II} = \sum_{k=0}^L (\partial \gamma_i^{I/II} / \partial \phi_k^{I/II}) \phi_k^{I/II}$. We can similarly proceed for the R.H.S of Eq. (2.5) and collect coefficients of j_i^{II} and j_l^{II} with $l \neq i$. Using the conservation law for particle number Eq. (2.4), we can recast the dynamic constraint Eq. (2.5) as a system of linear equations with a matrix of coefficients to solve for j_i^I for all components

(and in turn j_i^Π using the previous relation):

$$\begin{bmatrix} C_{00} & C_{01} & \dots & C_{0L} \\ \cdot & \cdot & \cdot & \cdot \\ \cdot & \cdot & \cdot & \cdot \\ \cdot & \cdot & \cdot & \cdot \\ C_{L0} & C_{L1} & \dots & C_{LL} \end{bmatrix} \begin{bmatrix} j_0^I \\ \cdot \\ \cdot \\ \cdot \\ j_L^I \end{bmatrix} = \begin{bmatrix} C_0 \\ \cdot \\ \cdot \\ \cdot \\ C_L \end{bmatrix}, \quad (\text{B.5})$$

$$C_{ii} = \left[\gamma_i^I (\phi_i^I - 1) + \phi_i^I \left(\Xi_i^I - \frac{\partial \gamma_i^I}{\partial \phi_i^I} \right) \right] + \frac{V^I}{V - V^I} \left[\gamma_i^\Pi (\phi_i^\Pi - 1) + \phi_i^\Pi \left(\Xi_i^\Pi - \frac{\partial \gamma_i^\Pi}{\partial \phi_i^\Pi} \right) \right], \quad (\text{B.6a})$$

$$C_{ij} = \left[\gamma_i^I \phi_i^I + \phi_i^I \left(\Xi_i^I - \frac{\partial \gamma_i^I}{\partial \phi_i^I} \right) \right] + \frac{V^I}{V - V^I} \left[\gamma_i^\Pi \phi_i^\Pi + \phi_i^\Pi \left(\Xi_i^\Pi - \frac{\partial \gamma_i^\Pi}{\partial \phi_i^\Pi} \right) \right], \quad (\text{B.6b})$$

$$C_i = \frac{V^I}{V - V^I} \left[\gamma_i^\Pi s_i^\Pi + \phi_i^\Pi \sum_{k=0}^L \frac{\partial \gamma_i^\Pi}{\partial \phi_k^\Pi} s_k^\Pi \right] - \left[\gamma_i^I s_i^I + \phi_i^I \sum_{k=0}^L \frac{\partial \gamma_i^I}{\partial \phi_k^I} s_k^I \right]. \quad (\text{B.6c})$$

Using the above procedure to obtain expressions for j_i^I and in turn j_i^Π , we can substitute them in Eq. (2.3a) and Eq. (2.3b) and solve for the unknown variables using a forward Euler method, having specified $\phi_i^I(t=0)$, $\phi_i^\Pi(t=0)$ (for $i=0, \dots, L$) and $V^I(t=0)$ as the initial conditions.

Chemical kinetics via determination of the average volume fractions

Using the kinetic equations for the average volume fractions, Eq. (B.2), we can solve for the volume fractions of all components in each phase $\{\phi_i^{I/\Pi}\}$ and the phase volumes $V^{I/\Pi}$ at each time point via an iterative method. In particular, after initializing the system with $\phi_i^I(t=0)$, $\phi_i^\Pi(t=0)$ (for $i=0, \dots, L$) and $V^I(t=0)$, Eqs. (1.17) can be used to obtain the average volume fractions in each phase forward in time. Those forward average volume fractions can be used to obtain the forward equilibrium volume fractions and phase volumes of each phase via solving Eqs. (1.17) and using $V^I = V(\bar{\phi}_i - \phi_i^\Pi)/(\phi_i^I - \phi_i^\Pi)$ sequentially. This is computationally efficient as the above method for a system with fewer components (ternary $L=2$) but becomes numerically expensive with increasing components. However, it is straightforward to implement, and we use it in chapter 4.

Chapter 3: Numerical recipes for modified Cahn-Hilliard dynamics in spherical geometry

We use the finite element method to study the evolution of a binary system ($L=2$) to study the stationary state profile of the scaffold volume fraction Fig. 3.4. The spherical mesh is generated in Gmsh and implemented using an open-source and free software FEniCS [94]. The modified Cahn-Hilliard equation is a fourth-order equation, so casting it in a weak form would result in the presence of second-order spatial derivatives, and the problem could not be solved using a standard Lagrange finite element basis. A solution is

to rephrase the problem as two coupled second-order equations,

$$\begin{aligned} \partial_t \phi_1 - \nabla \cdot (m_{01} \nabla \bar{\mu}_1) &= 0 & \text{in } \Omega \\ \bar{\mu}_1 - \frac{df}{d\phi_1} + \kappa_1 \nabla^2 \phi_1 &= 0 & \text{in } \Omega \end{aligned} \quad (\text{B.7})$$

subject to boundary conditions,

$$\begin{aligned} m_{01} \left(\nabla \cdot \left(\frac{df}{d\phi_1} - \kappa_1 \nabla^2 \phi_1 \right) \right) \cdot \mathbf{n} &= 0 & \text{in } \partial\Omega \\ m_{01} \kappa_1 \nabla \phi_1 \cdot \mathbf{n} &= 0 & \text{in } \partial\Omega \end{aligned} \quad (\text{B.8})$$

where $df/d\phi_1 = \log \phi_1 / \log(1 - \phi_1) + \chi_{01}(1 - 2\phi_1)$ and Ω and $\partial\Omega$ represents the system volume and boundary respectively.

Chapter 3: Finite difference methods for reaction-diffusion equations

To solve the coupled reaction-diffusion equations, we use finite difference methods in the bulk spatial points of phases I/II. The stencil used for the finite difference method, in a spherically symmetric geometry, is the same as in [95]. One has to be aware of the von-Neumann stability condition, which can be a bottleneck given it constrains the choice for time step according to the choice of diffusion coefficients given by the *mesh Fourier number* to satisfy the inequality,

$$\frac{D_i^{\text{I/II}} dt}{(dx)^2} \leq 0.5. \quad (\text{B.9})$$

As for the boundary conditions at the interface of the drop, we incorporate the conditions explicitly by using floating spatial grid points, which then are coupled to the bulk spatial grid points through the Laplacian discretization stencil. The time step is also incorporated in an explicit forward Euler method. It looks as follows to obtain the volume fraction at space point x_i at time point t_n ,

$$\frac{\phi_i^n - \phi_i^{n-1}}{dt} = \tilde{D} \frac{\phi_{i+1}^{n-1} - 2\phi_i^{n-1} + \phi_{i-1}^{n-1}}{(dx)^2} + f_i^{n-1} \quad (\text{B.10})$$

Appendix C

Linear first order corrections to scaffold equilibrium volume fractions

The total number of components is $(L + 2)$, which includes L dilute clients, the non-dilute scaffold (1), and the non-dilute solvent (0). Given the incompressibility constraint, one degree of freedom of the solvent volume fraction can be removed. Therefore, to investigate the thermodynamical properties of the entire system, one has to study an $(L + 1)$ -dimensional phase diagram.

We start with a perturbation of the true equilibrium volume fractions in the $(L + 1)$ dimensional phase diagram,

$$\phi_1^{I/II}|_{L+1} = \phi_1^{\text{eq},I/II}|_{L+1} + \delta\phi_1^{I/II} \quad (\text{C.1a})$$

$$\phi_i^{I/II}|_{L+1} = \phi_i^{\text{eq},I/II}|_{L+1} + \delta\phi_i^{I/II} \quad (\text{C.1b})$$

The aim is to derive the linear corrections a_i to binary scaffold equilibrium concentrations due to presence of L dilute client components, where $\{\phi_i^{\text{eq},I/II}\}$ represent the small variable around which we wish to expand,

$$\phi_1^{\text{eq},I/II}|_{L+1} \simeq \phi_1^{\text{eq},I/II}|_1 + \sum_{i=1}^L a_i^{I/II} \phi_i^{\text{eq},I/II}|_{L+1} + \dots \quad (\text{C.2})$$

The slopes in each phase due to the correction can be related to the perturbations as,

$$a_i^{I/II} = \frac{\phi_1^{\text{eq},I/II}|_{L+1} - \phi_1^{\text{eq},I/II}|_1}{\phi_i^{\text{eq},I/II}|_{L+1} - 0} = \frac{\delta\phi_1^{I/II}}{\delta\phi_i^{I/II}} \quad (\text{C.3})$$

To obtain the expressions for the linear corrections, we use the osmotic pressure equivalence condition,

$$f(\{\phi_j^{\text{eq},I}\}) - f(\{\phi_j^{\text{eq},II}\}) = \sum_{i=1}^{L+1} \frac{\bar{\mu}_i(\{\phi_k^{\text{eq},I/II}\})}{\nu_i} (\phi_i^{\text{eq},I} - \phi_i^{\text{eq},II}), \quad (\text{C.4})$$

and expand it around the $(L + 1)$ -dim equilibrium volume fractions,

$$\begin{aligned}
& \left[f(\{\phi_j^{\text{eq,I}}\}) - f(\{\phi_j^{\text{eq,II}}\}) \right] + \left[\sum_{k=1}^{L+1} \frac{\partial f(\{\phi_j^{\text{eq,I}}\})}{\partial \phi_k} \delta \phi_k^{\text{I}} - \sum_{k=1}^{L+1} \frac{\partial f(\{\phi_j^{\text{eq,II}}\})}{\partial \phi_k} \delta \phi_k^{\text{II}} \right] \\
&= \left[\sum_{k=1}^{L+1} \frac{\bar{\mu}_k(\{\phi_j^{\text{eq,I/II}}\})}{\nu_k} (\phi_k^{\text{eq,I}} - \phi_k^{\text{eq,II}}) \right] + \sum_{k,l=1}^{L+1} \frac{1}{\nu_k} \frac{\partial \bar{\mu}_k(\{\phi_j^{\text{eq,I/II}}\})}{\partial \phi_l} \delta \phi_l^{\text{I/II}} (\phi_k^{\text{eq,I}} - \phi_k^{\text{eq,II}}) \\
&+ \sum_{k=1}^{L+1} \frac{1}{\nu_k} \left[\bar{\mu}_k(\{\phi_j^{\text{eq,I}}\}) \delta \phi_k^{\text{I}} - \bar{\mu}_k(\{\phi_j^{\text{eq,II}}\}) \delta \phi_k^{\text{II}} \right]
\end{aligned} \tag{C.5}$$

The first terms on the R.H.S and the L.H.S cancel due to the equality of osmotic pressure being satisfied at $\{\phi_j^{\text{eq,I/II}}\}$. The second term from L.H.S in square brackets and the third term from R.H.S in square brackets cancel too, being equal by definition of exchange chemical potentials. The only surviving term is the second term from R.H.S which we can re-arrange to obtain the slopes as Eq. (C.3)

The re-arranged formula is,

$$\frac{1}{\nu_1} \sum_{k=1}^{L+1} \frac{\partial \bar{\mu}_1(\{\phi_j^{\text{eq,I/II}}\})}{\partial \phi_k} \delta \phi_k^{\text{I/II}} (\phi_1^{\text{eq,I}} - \phi_1^{\text{eq,II}}) = \sum_{\substack{l=2 \\ k=1}}^{L+1} \frac{1}{\nu_l} \frac{\partial \bar{\mu}_l(\{\phi_j^{\text{eq,I/II}}\})}{\partial \phi_k} \delta \phi_k^{\text{I/II}} (\phi_l^{\text{eq,II}} - \phi_l^{\text{eq,I}}) \tag{C.6}$$

Collecting coefficients of $\delta \phi_1^{\text{I/II}}$:

$$\begin{aligned}
& \delta \phi_1^{\text{I/II}} \left[\frac{1}{\nu_1} \frac{\partial \bar{\mu}_1^{\text{I/II}}}{\partial \phi_1} (\phi_1^{\text{eq,I}} - \phi_1^{\text{eq,II}}) + \sum_{k=2}^{L+1} \frac{1}{\nu_k} \frac{\partial \bar{\mu}_k^{\text{I/II}}}{\partial \phi_1} (\phi_k^{\text{eq,I}} - \phi_k^{\text{eq,II}}) \right] \\
&= \sum_{i=2}^{L+1} \delta \phi_i^{\text{I/II}} \left[\frac{1}{\nu_1} \frac{\partial \bar{\mu}_1^{\text{I/II}}}{\partial \phi_i} (\phi_1^{\text{eq,II}} - \phi_1^{\text{eq,I}}) + \sum_{k=2}^{L+1} \frac{1}{\nu_k} \frac{\partial \bar{\mu}_k^{\text{I/II}}}{\partial \phi_i} (\phi_k^{\text{eq,II}} - \phi_k^{\text{eq,I}}) \right]
\end{aligned} \tag{C.7}$$

The slopes are therefore,

$$a_i^{\text{I/II}} = \frac{\delta \phi_1^{\text{I/II}}}{\delta \phi_i^{\text{I/II}}} = \frac{\frac{1}{\nu_1} \frac{\partial \bar{\mu}_1^{\text{I/II}}}{\partial \phi_i} (\phi_1^{\text{eq,II}} - \phi_1^{\text{eq,I}}) + \sum_{k=2}^{L+1} \frac{1}{\nu_k} \frac{\partial \bar{\mu}_k^{\text{I/II}}}{\partial \phi_i} (\phi_k^{\text{eq,II}} - \phi_k^{\text{eq,I}})}{\frac{1}{\nu_1} \frac{\partial \bar{\mu}_1^{\text{I/II}}}{\partial \phi_1} (\phi_1^{\text{eq,I}} - \phi_1^{\text{eq,II}}) + \sum_{k=2}^{L+1} \frac{1}{\nu_k} \frac{\partial \bar{\mu}_k^{\text{I/II}}}{\partial \phi_1} (\phi_k^{\text{eq,I}} - \phi_k^{\text{eq,II}})} \tag{C.8}$$

Of all the derivatives of exchange chemical potential, $\frac{\partial \bar{\mu}_i}{\partial \phi_i}$ diverges as $\phi_i \rightarrow 0$. We divide throughout by $(\phi_1^{\text{eq,I}} - \phi_1^{\text{eq,II}})$ to obtain, that lead to the expression of the slopes, $a_i^{\text{I/II}}$ as,

$$a_i^{\text{I/II}} = \frac{\delta \phi_1^{\text{I/II}}}{\delta \phi_i^{\text{I/II}}} = \lim_{\substack{\phi_{i,k}^{\text{eq,I/II}}|_{L+1} \rightarrow 0 \\ i,k \neq 1 \\ \phi_1^{\text{eq,I/II}}|_{L+1} \rightarrow \phi_1^{\text{eq,I/II}}|_1}} - \frac{\frac{1}{\nu_k} \sum_{k=1}^L \frac{\partial \bar{\mu}_k}{\partial \phi_i} \frac{(\phi_k^{\text{eq,I}} - \phi_k^{\text{eq,II}})}{(\phi_1^{\text{eq,I}} - \phi_1^{\text{eq,II}})} + \frac{1}{\nu_1} \frac{\partial \bar{\mu}_1}{\partial \phi_i}}{\frac{1}{\nu_k} \sum_{k=1}^L \frac{\partial \bar{\mu}_k}{\partial \phi_1} \frac{(\phi_k^{\text{eq,I}} - \phi_k^{\text{eq,II}})}{(\phi_1^{\text{eq,I}} - \phi_1^{\text{eq,II}})} + \frac{1}{\nu_1} \frac{\partial \bar{\mu}_1}{\partial \phi_1}} \tag{C.9}$$

The expressions of derivatives of the exchange chemical potential of the scaffold with

respect to all volume fractions are,

$$\frac{\partial \bar{\mu}_1}{\partial \phi_1} = k_B T \left[\frac{1}{\phi_1} + \frac{r_1}{r_0} \frac{1}{(1 - \phi_1 - \sum_k \phi_k)} - 2r_1 \chi_{01} \right] \quad (\text{C.10a})$$

$$\frac{\partial \bar{\mu}_1}{\partial \phi_i} = k_B T \left[\frac{r_1}{r_0} \frac{1}{(1 - \phi_1 - \sum_k \phi_k)} + r_1 (\chi_{1i} - \chi_{0i} - \chi_{01}) \right] \quad (\text{C.10b})$$

The expressions of the derivatives of the exchange chemical potential of the clients with respect to all other volume fractions are as follows,

$$\frac{\partial \bar{\mu}_i}{\partial \phi_1} = k_B T \left[\frac{r_i}{r_0} \frac{1}{(1 - \phi_1 - \sum_k \phi_k)} + r_i (\chi_{1i} - \chi_{0i} - \chi_{01}) \right] \quad (\text{C.10c})$$

$$\frac{\partial \bar{\mu}_i}{\partial \phi_i} = k_B T \left[\frac{1}{\phi_i} + \frac{r_i}{r_0} \frac{1}{(1 - \phi_1 - \sum_k \phi_k)} - 2r_i \chi_{0i} \right] \quad (\text{C.10d})$$

$$\frac{\partial \bar{\mu}_i}{\partial \phi_j} = k_B T \left[\frac{r_i}{r_0} \frac{1}{(1 - \phi_1 - \sum_k \phi_k)} + r_i (\chi_{ij} - \chi_{0i} - \chi_{0j}) \right] \quad (\text{C.10e})$$

Using the expressions of the derivatives in Eq. (C.10) and the expression for constant partition coefficient in Eq. (3.5) we obtain

$$a_i^I = -\phi_1^{\text{eq},I}|_1 \frac{r_0^{-1} + \left(\chi_{1i} - \chi_{01} - \chi_{0i} + \frac{1-1/P_i}{r_i(\phi_1^{\text{eq},I}|_1 - \phi_1^{\text{eq},II}|_1)} \right) (1 - \phi_1^{\text{eq},I}|_1)}{\frac{1-\phi_1^{\text{eq},I}|_1}{r_1} + \frac{\phi_1^{\text{eq},I}|_1}{r_0} - 2\chi_{01}\phi_1^{\text{eq},I}|_1(1 - \phi_1^{\text{eq},I}|_1)} \quad (\text{C.11a})$$

$$a_i^{II} = -\phi_1^{\text{eq},II}|_1 \frac{r_0^{-1} + \left(\chi_{1i} - \chi_{01} - \chi_{0i} + \frac{P_i-1}{r_i(\phi_1^{\text{eq},I}|_1 - \phi_1^{\text{eq},II}|_1)} \right) (1 - \phi_1^{\text{eq},II}|_1)}{\frac{1-\phi_1^{\text{eq},II}|_1}{r_1} + \frac{\phi_1^{\text{eq},II}|_1}{r_0} - 2\chi_{01}\phi_1^{\text{eq},II}|_1(1 - \phi_1^{\text{eq},II}|_1)} \quad (\text{C.11b})$$

We can use this derivation to estimate the client's critical average volume fraction, beyond which the dilute approximation fails. We have to choose a threshold (here 1%) such that the deviation due to the dilute approximation is less than the threshold,

$$\frac{\text{Abs}(\phi_1^{\text{eq},I/II}|_1 - \phi_1^{\text{eq},I/II}|_{L+1})}{\phi_1^{\text{eq},I/II}|_1} < 0.01 \quad (\text{C.12})$$

which translates to

$$\frac{a_i^{I/II}}{\phi_1^{\text{eq},I/II}|_1} \phi_i^{I/II}|_1 < 0.01 \quad (\text{C.13})$$

Given we have closed-form expressions for $a_i^{I/II}$ and we know the binary scaffold eq. volume fraction, we can obtain the client volume fraction in which the approximation holds.

In chapter 3, we use the above result, substituting $r_0 = 1$ and $\phi_1^{\text{eq},I/II}|_1$ is substituted as $\phi_1^{0,I/II}$ in the main text as binary equilibrium volume fractions.

Appendix D

Dynamic equations in dilute limit

Using the definition of the dilute limit subject to which the exchange activity coefficient and, therefore, the exchange chemical potential of the scaffold is independent of the clients. With the end goal of computing the diffusive flux of the scaffold in the dilute limit, we start by calculating the gradients of its exchange chemical potential $\nabla\bar{\mu}_1$ (diffusive force in analogy to reaction force $H_{I/II}$ in Eq. (2.7)), followed by multiplying with the diffusion rate coefficients (mobility matrix).

For scaffold:

$$\nabla\bar{\mu}_1 = \frac{\partial\bar{\mu}_1}{\partial\phi_1}\nabla\phi_1 - \kappa_{11}\nabla\nabla^2\phi_1 + \sum_{k=2}^{L+1} \frac{\partial\bar{\mu}_1}{\partial\phi_k}\nabla\phi_k = \left[\frac{1}{\phi_1} + \frac{1}{\bar{\gamma}_1} \frac{\partial\bar{\gamma}_1}{\partial\phi_1} \right] \nabla\phi_1 - \kappa_{11}\nabla\nabla^2\phi_1 \quad (\text{D.1})$$

$$\mathbf{j}_1 = - \left[m_{01}\phi_1(1 - \phi_1 - \sum_{i=2}^{L+1} \phi_i) + \sum_{\substack{k \neq 1 \\ k=2}}^{L+1} m_{1k}\phi_1\phi_k \right] \nabla\bar{\mu}_1 + \sum_{\substack{k \neq 1 \\ k=2}}^{L+1} m_{1k}\phi_1\phi_k \nabla\bar{\mu}_k \quad (\text{D.2})$$

$$\begin{aligned} \mathbf{j}_1 &= -m_{01}\phi_1(1 - \phi_1) \left[\left(\frac{1}{\phi_1} + \frac{1}{\bar{\gamma}_1} \frac{\partial\bar{\gamma}_1}{\partial\phi_1} \right) \nabla\phi_1 - \kappa_{11}\nabla\nabla^2\phi_1 \right] \\ &= -m_{01} \left[\left(1 + \phi_1 \left(\frac{r_1}{r_0} - 1 \right) - 2r_1\chi_{01}\phi_1(1 - \phi_1) \right) \nabla\phi_1 - \kappa_{11}\nabla\nabla^2\phi_1 \right] \end{aligned} \quad (\text{D.3})$$

For clients:

$$\nabla\bar{\mu}_i = \frac{\partial\bar{\mu}_i}{\partial\phi_1}\nabla\phi_1 + \sum_{k=2}^{L+1} \frac{\partial\bar{\mu}_i}{\partial\phi_k}\nabla\phi_k = \frac{1}{\bar{\gamma}_i} \frac{\partial\bar{\gamma}_i}{\partial\phi_1}\nabla\phi_1 + \frac{1}{\phi_i}\nabla\phi_i \quad (\text{D.4})$$

$$\mathbf{j}_i = - \left[m_{0i}\phi_i(1 - \phi_1 - \sum_{k=2}^{L+1} \phi_k) + \sum_{\substack{k \neq i \\ k=1}}^{L+1} m_{ik}\phi_i\phi_k \right] \nabla\bar{\mu}_i + \sum_{\substack{k \neq i \\ k=1}}^{L+1} m_{ik}\phi_i\phi_k \nabla\bar{\mu}_k \quad (\text{D.5})$$

$$\begin{aligned} \mathbf{j}_i &= - (m_{0i}\phi_i(1 - \phi_1) + m_{1i}\phi_i\phi_1) \left[\frac{1}{\bar{\gamma}_i} \frac{\partial\bar{\gamma}_i}{\partial\phi_1}\nabla\phi_1 + \frac{1}{\phi_i}\nabla\phi_i \right] + m_{1i}\phi_i\phi_1 \left[\left(\frac{1}{\phi_1} + \frac{1}{\bar{\gamma}_1} \frac{\partial\bar{\gamma}_1}{\partial\phi_1} \right) \nabla\phi_1 \right. \\ &\quad \left. - \kappa_{11}\nabla\nabla^2\phi_1 \right] \end{aligned} \quad (\text{D.6})$$

We collect the coefficients in the flux of $\nabla\phi_1$ and re-arrange the equation as follows,

$$\begin{aligned} \mathbf{j}_i = & \left[-m_{0i} \left(r_i(\chi_{1i} - \chi_{0i} - \chi_{01}) + \frac{r_i}{r_0} \right) + m_{1i} \left(1 + \frac{(r_1 - r_i)}{r_0} \frac{\phi_1}{1 - \phi_1} - 2r_1\chi_{01}\phi_1 \right) \right] \phi_i \nabla\phi_1 \\ & - \left[m_{0i}(1 - \phi_1) + m_{1i}\phi_1 \right] \nabla\phi_i - m_{1i}\phi_i\phi_1\kappa_1 \nabla\nabla^2\phi_1 \end{aligned} \tag{D.7}$$

Further simplifying the fluxes by maintaining $\mathcal{O}(\bar{\phi}_i)^0$ in the mobility scaling, maintaining the dilute approximation for the scaffold leads to,

We have neglected here the terms $\kappa_i|\nabla\phi_i|^2$ for the dilute clients because they are negligible compared to relevant length scales in the problem, and diluteness leads to these terms not contributing to drop formation or affecting the drop interface.

Similarly, for the clients, we can proceed as above by neglecting orders $\mathcal{O}(\bar{\phi}_i)^1$ and beyond by neglecting terms of the type $\phi_i\nabla\phi_k$.

Appendix E

Spatial solutions

We obtain the analytical steady state solutions for the clients A_1 and B , given their dynamical equation governed by Eq. (3.18) is linear. The reaction rates are stated in the main text. The system is spherically symmetric, and the Laplacian operator in spherically symmetric coordinates can be mapped to the Laplacian in cartesian coordinates by variable transformation.

$$\begin{aligned}
 u(r) &= r\phi(r) \quad \text{variable transformation} \\
 &\left[\frac{1}{r^2} \frac{d}{dr} \left(r^2 \frac{d}{dr} \right) \right] \phi(r) \quad \text{Laplacian operator in spherical symmetric coordinates} \\
 \implies &\left[\frac{2}{r} \frac{d}{dr} + \frac{d^2}{dr^2} \right] \frac{u(r)}{r} \\
 \implies &\frac{2}{r^2} \frac{du(r)}{dr} - \frac{2u(r)}{r^3} + \frac{1}{r} \frac{d^2u(r)}{dr^2} - \frac{1}{r^2} \frac{du(r)}{dr} + \frac{2u(r)}{r^3} - \frac{1}{r^2} \frac{du}{dr} \\
 \implies &\frac{1}{r} \frac{d^2u(r)}{dr^2} \quad \text{Laplacian operator in cartesian coordinates} \\
 &\text{Solve for } u(r) \text{ and divide by } r \text{ to revert to } \phi(r)
 \end{aligned}$$

The emergent reaction-diffusion length scales of the coupled PDEs are given by,

$$\lambda_{\text{rd}}^{\text{I/II}} = \sqrt{\frac{D_{A_1}^{\text{I/II}} D_B^{\text{I/II}}}{k^{\text{I/II}} \left[D_{A_1}^{\text{I/II}} \exp\left(\frac{\bar{\mu}_B^0}{k_B T}\right) \tilde{\gamma}_B^{\text{I/II}} + D_B^{\text{I/II}} \exp\left(\frac{\bar{\mu}_{A_1}^0 + \bar{\mu}_F^{\text{I/II}}}{k_B T}\right) \tilde{\gamma}_{A_1}^{\text{I/II}} \right]}}. \quad (\text{E.1})$$

The full solutions for the spatially dependent steady state volume fractions for A_1 and B are given below. The non-dimensional length is r (rescaled by system size radius R) and time is \tilde{t} (time scale is $(k^{\text{I}})^{-1}$). The volume fraction scale is conserved quantity ψ_1 and the diffusion scale is $R^2(k^{\text{I}})^{-1}$. In terms of the non-dimensionalized parameters, the solutions are as follows for the uni-molecular reaction scheme (assuming only $\tilde{\mu}_F^{\text{I}} \neq 0$),

$$\phi_{A_1}^{\text{I}}(r, \infty) = \frac{\beta(D_{A_1}^{\text{I}} \mathbf{C}_1 + D_B^{\text{I}} \mathbf{C}_2)}{(\alpha D_B^{\text{I}} \exp(\tilde{\mu}_F^{\text{I}}/k_B T) + \beta D_{A_1}^{\text{I}})} + \frac{D_B^{\text{I}}(\alpha \mathbf{C}_1 \exp(\tilde{\mu}_F^{\text{I}}/k_B T) - \beta \mathbf{C}_2)}{(\alpha D_B^{\text{I}} \exp(\tilde{\mu}_F^{\text{I}}/k_B T) + \beta D_{A_1}^{\text{I}})} \frac{\sinh(r/\lambda_{\text{rd}}^{\text{I}})}{r/\lambda_{\text{rd}}^{\text{I}}} \quad (\text{E.2a})$$

$$\phi_{A_1}^I(r, \infty) = \frac{\alpha \exp(\tilde{\mu}_F^I/k_B T) (D_{A_1}^I \mathbf{C}_1 + D_B^I \mathbf{C}_2)}{(\alpha D_B^I \exp(\tilde{\mu}_F^I/k_B T) + \beta D_{A_1}^I)} - \frac{D_{A_1}^I (\alpha \mathbf{C}_1 \exp(\tilde{\mu}_F^I/k_B T) - \beta \mathbf{C}_2)}{(\alpha D_B^I \exp(\tilde{\mu}_F^I/k_B T) + \beta D_{A_1}^I)} \frac{\sinh(r/\lambda_{rd}^I)}{r/\lambda_{rd}^I} \quad (\text{E.2b})$$

$$\begin{aligned} \phi_{A_1}^{II}(r, \infty) &= \frac{P_B \beta (D_{A_1}^{II} (\mathbf{C}_3 + r \mathbf{C}_4) + D_B^{II} (\mathbf{C}_5 + r \mathbf{C}_6))}{r (P_{A_1} \alpha D_B^{II} + P_B \beta D_{A_1}^{II})} + \frac{D_B^{II} (P_{A_1} \alpha \mathbf{C}_3 - P_B \beta \mathbf{C}_5) \cosh(r/\lambda_{rd}^{II})}{(P_{A_1} \alpha D_B^{II} + P_B \beta D_{A_1}^{II}) r} \\ &+ \frac{D_B^{II} (P_{A_1} \alpha \mathbf{C}_4 - P_B \beta \mathbf{C}_6) \sinh(r/\lambda_{rd}^{II})}{(P_{A_1} \alpha D_B^{II} + P_B \beta D_{A_1}^{II}) r/\lambda_{rd}^{II}} \end{aligned} \quad (\text{E.2c})$$

$$\begin{aligned} \phi_B^{II}(r, \infty) &= \frac{P_{A_1} \alpha (D_{A_1}^{II} (\mathbf{C}_3 + r \mathbf{C}_4) + D_B^{II} (\mathbf{C}_5 + r \mathbf{C}_6))}{r (P_{A_1} \alpha D_B^{II} + P_B \beta D_{A_1}^{II})} - \frac{D_B^{II} (P_{A_1} \alpha \mathbf{C}_3 - P_B \beta \mathbf{C}_5) \cosh(r/\lambda_{rd}^{II})}{(P_{A_1} \alpha D_B^{II} + P_B \beta D_{A_1}^{II}) r} \\ &- \frac{D_B^{II} (P_{A_1} \alpha \mathbf{C}_4 - P_B \beta \mathbf{C}_6) \sinh(r/\lambda_{rd}^{II})}{(P_{A_1} \alpha D_B^{II} + P_B \beta D_{A_1}^{II}) r/\lambda_{rd}^{II}} \end{aligned} \quad (\text{E.2d})$$

where $\alpha = \exp(\bar{\mu}_{A_1}^0/k_B T) \bar{\gamma}_{A_1}^I$ and $\beta = \exp(\bar{\mu}_B^0/k_B T) \bar{\gamma}_B^I$. The six undetermined constants \mathbf{C}_i are evaluated by solving six boundary value conditions (having used $r = 0$ boundary conditions already to obtain Eqs. (E.2)). The average volume fractions of A_1 and B are determined using,

$$\bar{\phi}_j(\infty) = \frac{1}{V} \left(\int_0^{R_d/R} d\mathbf{r} \phi_j^I(r, \infty) + \int_{R/L}^1 d\mathbf{r} \phi_j^{II}(r, \infty) \right), \quad (\text{E.3})$$

Appendix F

Fitting routine and extracted rate coefficients

We study three succinate derivatives, labeled as P , C_1 , and C_2 and their corresponding anhydrides. We fit the experimental measurements with the kinetic traces of each of the reaction cycles to determine the rate coefficients (Figs.F.1, F.2 and F.3). The fitting is obtained by minimizing the sum of squared residuals of l data points,

$$S = \sum_{i=1}^l (y_i - f(t_i))^2 \quad (\text{F.1})$$

where y_i are the experimental concentration values and $f(t_i)$ are the theoretical predictions from the kinetic model as described in Eqs. (4.2a) and (4.2b). The minimization is numerically done using optimize module of SciPy library and the method is truncated Newton conjugate gradient (TNC).

Individual reaction cycles

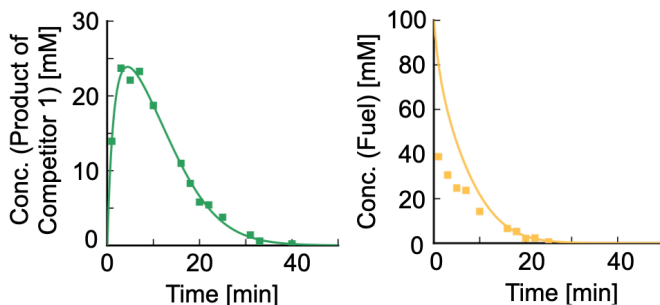


Fig. F.1: First order deactivation and short lifetime of the product of competitor 1. 50 mM competitor 1 fuelled with 100 mM EDC. The two curves, corresponding to the time trace of the product of competitor 1 and fuel concentration, respectively, are globally fitted to obtain the reaction rate coefficients. The concentration profile of the product of competitor 1 shows an exponential decay as it is not able to phase separate due to its high solubility of roughly 3000 mM. Markers represent HPLC data; solid lines represent data calculated using the theoretical kinetic model.

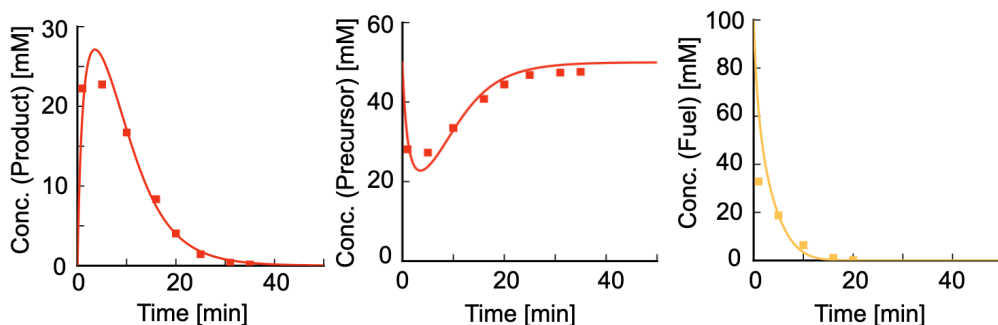


Fig. F.2: First order deactivation and short lifetime of the product. 50 mM precursor fuelled with 100 mM EDC. The three curves, corresponding to the time trace of the product, precursor, and fuel concentration, respectively, are globally fitted to obtain the reaction rate coefficients. The product concentration profile shows an exponential decay as it is not able to phase separate due to its high solubility of roughly 27 mM. Markers represent HPLC data; solid lines represent data calculated using the theoretical kinetic model.

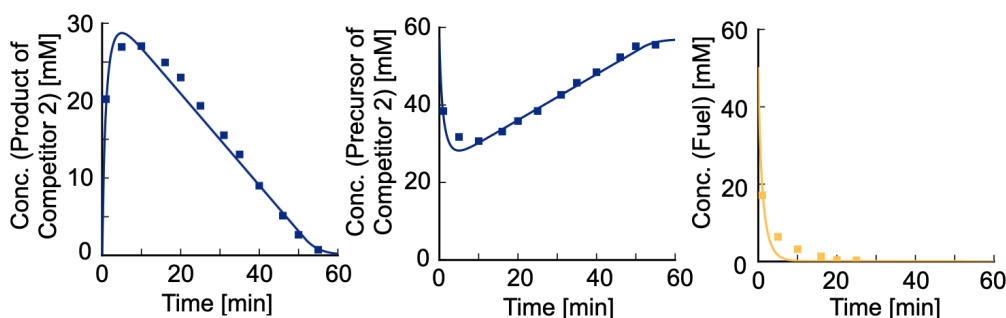


Fig. F.3: Zeroth order deactivation and long lifetime of the product of competitor 2. 50 mM competitor 2 fuelled with 50 mM EDC. The three curves, corresponding to the time trace of the product of competitor 2, competitor 2, and fuel concentration, respectively, are globally fitted to obtain the reaction rate coefficients. The concentration profile of the product of competitor 2 shows a linear decay as it is able to phase separate due to its low solubility of roughly 2 mM. Markers represent HPLC data; solid lines represent data calculated using the theoretical kinetic model. The concentration of competitor 2 had to be re-adjusted to 57 mM in the theoretical kinetic model for the fitting procedure due to inaccuracies in the stock solution.

Combined reaction cycle: Precursor Vs Competitor 1

Having obtained the reaction rate coefficients from the above fits in Fig. F.4, we proceed to see how the traces change with changing competitor 1 (C_1) concentration and using fixed precursor (P) and EDC concentrations (Fig.F.5).

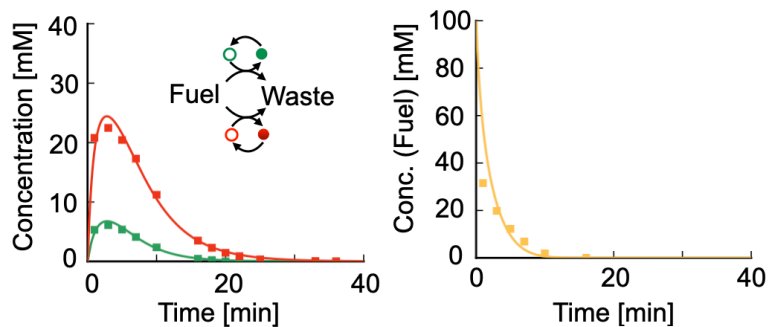


Fig. F.4: First order deactivation for the product and product of competitor 1. 50 mM precursor and 50 mM competitor 1 fuelled with 100 mM EDC. The three curves, corresponding to the time trace of two anhydrides and fuel concentration, respectively, are globally fitted to obtain the reaction rate coefficients. The concentration profiles of the product and product of competitor 1 both show exponential decay as neither is able to phase separate and competition for fuel results in reduced yields for both anhydrides. Markers represent HPLC data; solid lines represent data calculated using the theoretical kinetic model.

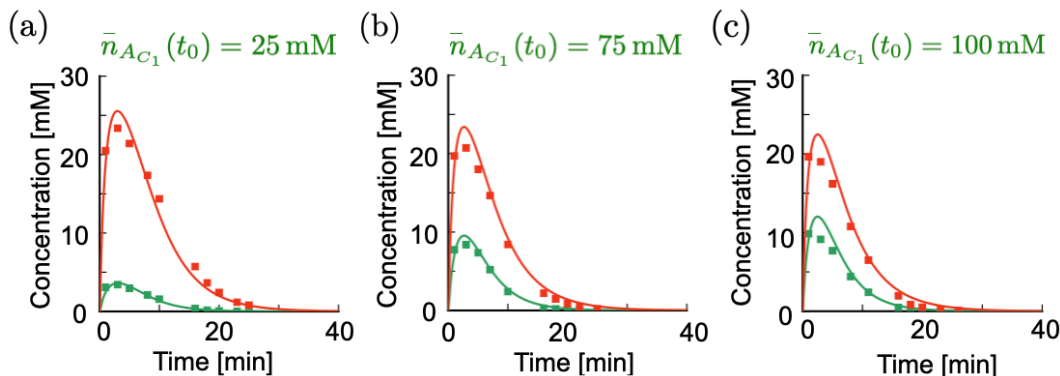


Fig. F.5: Competitor 1 reduces the yield and lifetime of the product. Competitor 1 concentration of (a) 25 mM, (b) 75 mM, (c) 100 mM, and 50 mM precursor fuelled with 100 mM EDC. Increasing the competitor 1 concentration reduces the maximum yield of the product and also its lifetime. Markers represent HPLC data; solid lines represent data calculated using the theoretical kinetic model.

Combined reaction cycle: Precursor Vs Competitor 2

Having obtained the reaction rate coefficients from the above fits in Fig. F.6, we proceed to see how the traces change with changing competitor 2 (C_2) concentration and using fixed precursor (P) and EDC concentrations (Fig.F.7).

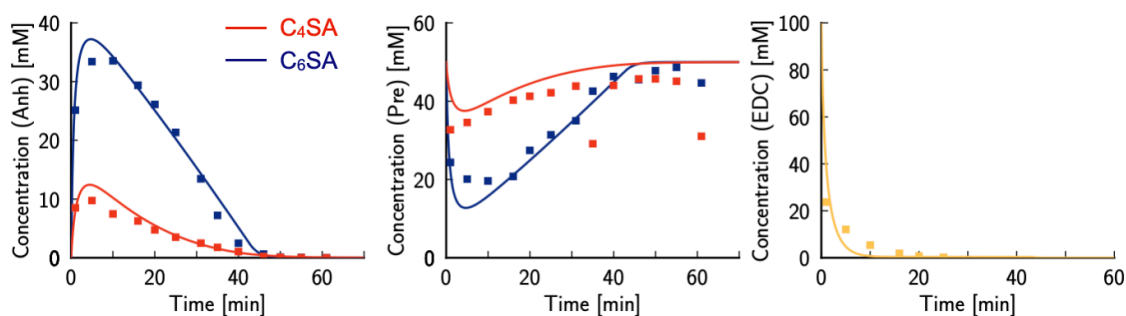


Fig. F.6: Non-linear and linear deactivation for the product and product of competitor 2 respectively. 50 mM precursor and 50 mM competitor 2 fueled with 100 mM EDC. We globally fit five curves corresponding to the time trace of two anhydrides, two succinate derivatives, and fuel concentration, respectively, to obtain the reaction rate coefficients. The two outlier points in the precursor concentration trace are omitted, however. The linear decay of the product of competitor 2 shows that it phase separates, and the non-linear decay of the product implies that it partitions in the droplets, which we refer to as co-phase separation. Markers represent HPLC data; solid lines represent data calculated using the theoretical kinetic model.

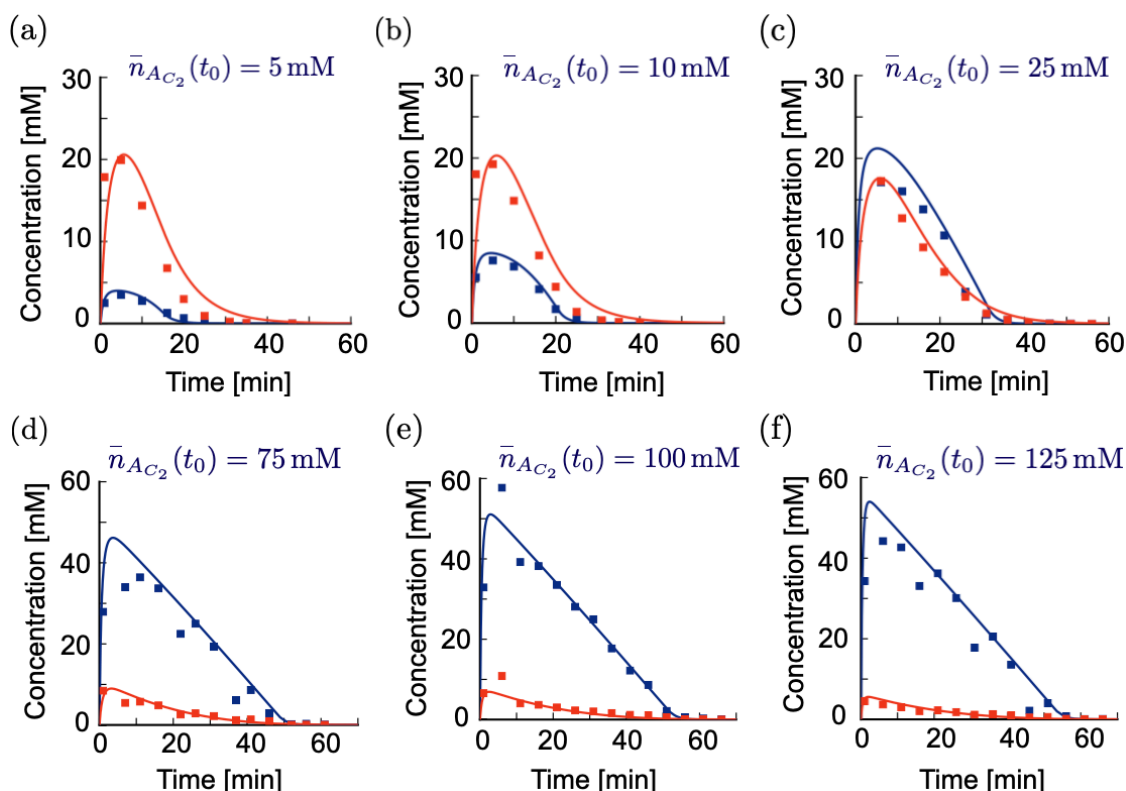


Fig. F.7: Competitor 2 reduces the yield but increases the lifetime of the product. Competitor 2 concentration of (a) 5 mM, (b) 10 mM, (c) 25 mM, (d) 75 mM, (e) 100 mM, (f) 125 mM and 50 mM precursor fueled with 100 mM EDC. Increasing competitor 2 concentration reduces the maximum yield of the product but prolongs its lifetime, allowing us to label competitor 2 as *host* and precursor as *parasite*. Markers represent HPLC data; solid lines represent data calculated using the theoretical kinetic model.

Name	Condition	k_0 [s ⁻¹]	k_1 [M ⁻¹ s ⁻¹]	k_2 [s ⁻¹]	k_3 [s ⁻¹]	k_4 [s ⁻¹]
Competitor 1	Single	1.35e-5	0.085	0.52	0.11	3.7e-3
	w/ Precursor		0.037	0.58	0.23	4.2e-3
Precursor	Single	1.35e-5	0.20	0.63	0.52	2.7e-3
	w/ Competitor 1		0.21	0.37	0.28	3.2e-3
	w/ Competitor 2		0.10	0.30	0.32	1.0 - 2.3e-3
Competitor 2	Single	1.35e-5	0.35	0.50	0.26	4.9 - 6.8e-3
	w/ Precursor		0.35	0.50	0.26	8.8e-3

Fig. F.8: Reaction rate coefficients. Readout for the reaction rate coefficients used in the kinetic model as obtained from the global fits.

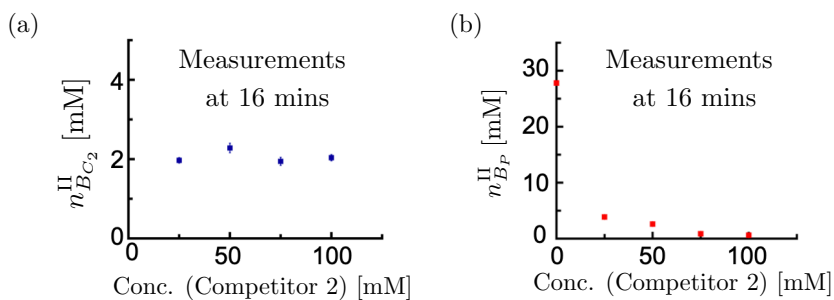


Fig. F.9: Dilute phase concentrations. (a) The concentration of the product of competitor 2 in the aqueous phase as a function of competitor 2 concentration. The value remains nearly constant around 2 mM, (b) The concentration of the product in the aqueous phase as a function of competitor 2 concentration. In the absence of competitor 2, the value is 27.8mM (solubility), decreasing with increasing competitor 2 concentration. The measurements are performed 16 mins into the reaction cycle.

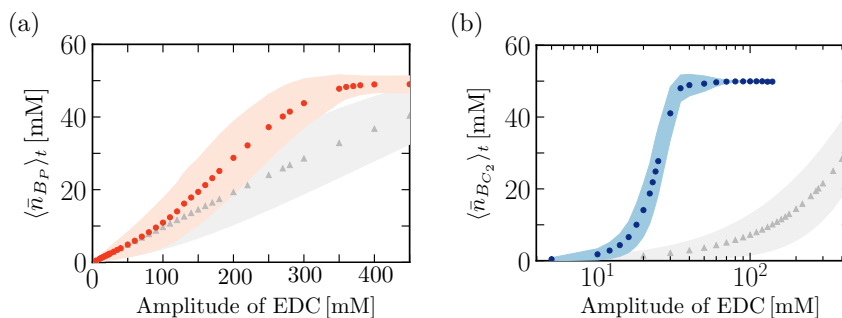


Fig. F.10: Poissonian fuelling in individual reaction cycles. Varying amplitude of EDC added in time points chosen from a Poisson distribution with fuelling rate $(1/30) \text{ min}^{-1}$ to (a) 50 mM precursor (b) 50 mM competitor 2. The colored data represents when the respective cycles can phase separate on reaching their solubilities at 27 mM and 2 mM. In contrast, the gray data is when theoretically, we suppress phase separation in the cycle. For the product, it doesn't make much difference when full turnover occurs. However, for the product of competitor 2, the turnover occurs earlier, and the concentration is buffered since it has low solubility.

Appendix G

Experimental methods

Chapter 4

The following experimental details are provided by our collaborator Patrick Schwarz affiliated with Prof. Boekhoven's Lab in Dept. of Chemistry in TUM.

HPLC

A ThermoFisher Dionex Ultimate 3000 analytical HPLC with a Hypersil Gold 250 \times 4.6 mm C18 column (5 mm pore size) was used to monitor the concentration profiles of each reactant of the chemical reaction network. 1.0 mL samples was prepared according to the sample preparation protocol described above into a screw cap HPLC vial. Samples were injected directly from the HPLC vial without any further dilution. 25 μ L was injected for the detection of the succinates and anhydrides and 1 μ L for the detection of EDC. A UV/Vis detector was used at 220 nm for the detection. A linear gradient of MQ water : ACN with 0.1 % TFA was used to separate the compounds. A linear gradient was used from 98 : 2 to 2 : 98 in 10 minutes followed by 2 minutes at 2 : 98 for the separation. The column was equilibrated for 2 minutes after each gradient. Calibration curves of the compounds were performed in triplicates. Calibration values and retention times are given in the supplementary information of Ref. [60].

Confocal fluorescence microscopy

The droplets were imaged using a Leica SP8 confocal microscope with a 63 \times oil immersion objective. Samples were prepared as described above but with 0.1 mM Nile Red added before EDC addition. 5 μ L sample was added to a silicon grease reservoir on a PEG-coated glass slide covered with a 12 mm diameter coverslip. The samples were excited with a 543 nm laser and imaged at 580–700 nm.

Chapter 5

The following experimental details are provided by our collaborator Mengfei Gao affiliated with Prof. Tang's Lab in MPICBG.

Preparation of BSA-PNIPAAm conjugate and Streptavidin-biotin-DNA conjugate

PNIPAAm with a mercaptothiazoline terminal group was synthesized via RAFT polymerization and structurally characterized with GPC and NMR as previously described in Ref. [90]. The as-synthesized PNIPAAm chain had a M_n of 14000 g/mol and M_w of 17000 g/mol. BSA-nat-pni was prepared by directly mixing the native protein solution to 1 mg/mL with PNIPAAm in 0.2 M NaHCO_3 solution at a molar ratio of 1:5. The mixture was incubated with shaking at 4° C for 16 hours, then filtered with 0.22 μm PVDF filter into a 25 kDa dialysis bag. The sample was then dialyzed against 0.2 \times PBS, with the buffer refreshed every hour for 3 hours in the cold room. After the dialysis, the conjugate was then concentrated to 1/10 of the original volume, aliquoted, and snap-freezing with liquid nitrogen.

Streptavidin-biotin-DNA was prepared as described before in Ref. [90]. In brief, biotinTEG-ssDNA was prepared in MillQ water to 100 μM and added 4 aliquots into streptavidin in buffer (10 mM Tris, 1 mM EDTA, pH8) to a final concentration of 10 μM ssDNA and 5 μM streptavidin. The mixture was vigorously shaken at 1000 rpm for 10 min at 25° C in between each aliquots.

Proteinosome preparation

To generate proteinosome, BSA-PNIPAAm, and streptavidin-biotin-DNA were mixed on ice in 0.1 M NaHCO_3 solution to a final concentration of 74 μM BSA-PNIPAAm and 1 or 2 μM ssDNA. BS(PEG)₉ was dissolved in anhydrous DMSO and mixed to 0.25 mM in 2-ethyl-1-hexanol at room temperature by vortexing. 1 mL mixture was transferred to the aqueous solution with a long-tip 1 mL pipette tip and pipetted to generate emulsion. After emulsification, another 1 mL of 2-ethyl-1-hexanol mixture was added to the top, and the mixture was stored at 8° C overnight.

To wash the proteinosome from 2-ethyl-1-hexanol, the emulsion was centrifuged first with a table centrifuge for 5 seconds, and the supernatant was removed. 1 mL of -20° C cold 75 % ethanol was added and pipetted cautiously until the pellet was fully resuspended. The sample was transferred to a clean Eppendorf tube and left in the fridge for 2-3 hours. After that, a series of centrifugation was applied with 3000 rpm, 3 minutes each at room temperature for BSA. At the end of each centrifugation, the supernatant was removed and replaced by 1 mL ice-cold 50%, 25% ethanol, and twice ultra pure water with cautious pipetting mixing. The proteinosome was taken for quality control imaging and left in the fridge until use.

PEN DNA assay

PEN DNA autocatalytic reaction was performed in buffer (20 mM Tris-HCl, 10 mM $(\text{NH}_4)_2\text{SO}_4$, 10 mM KCl, 2 mM MgSO_4 , 50 mM NaCl, 6 mM MgSO_4 , 1 g/L Synperonic F108, 1 μM Netropsin, 3 mM Dithiothreitol, 0.5 mg/mL native BSA, 3 μM EvaGreen dye, 0.1 mM dNTPs) containing (0.1, 1 or 10 nM) primer DNA, (0 to 1000 nM) template DNA, 400 units/mL Nb.BsmI nickase, 12.8 units/mL Bst DNA polymerase long fragments, and

0 or 1 nM ttRecJ exonuclease. Calibration samples were prepared in the same method but replacing nickase, polymerase, and exonuclease with an equivalent buffer containing an equivalent amount of glycerol. The exonuclease activity mixture was prepared in the same buffer without template DNA, polymerase, and nickase.

The samples were prepared into a 384-well plate (Flat black, Greiner) on ice and imaged with a SPARK 20 M well plate spectrophotometer (TECAN AG) at 42°C using 485/20 nm and 535/25 nm filter settings to illuminate the EvaGreen signal. Time-lapses were prepared at 1 or 2 minutes intervals.

PEN DNA inside proteinosome assay

Template DNA contained proteinosome was mixed in the buffer mentioned above at different dilutions. The mixture was loaded to a 1536 well plate and centrifuged at 3000 rcf shortly before the imaging. The samples were imaged at 42°C with an Andor IX83 inverted microscope equipped with Yokogawa CSU-W1 spinning disk, an Andor iXon ultra 888 Monochrome EMCCD camera, and Andor iQ3 (3.6.2) for imaging acquisition. UPLFLN20x/0.5 NA objective (Olympus) was used for the time-lapse imaging together with a Z-drift compensation system. Kinetics were performed at 2 minutes intervals. Calibration of the DNA inside the proteinosome was performed in the same manner with either diluted template DNA alone or fixed amount of template DNA, primer DNA, and EvaGreen. The calibration curve was extracted from the confocal images and used to calculate the concentration of template DNA and synthesized primer DNA.

Image analysis

To analyze the time series, the stacks were first drift corrected using StackRecJ with 'Translation' mode. Then the proteinosomes were identified with the template DNA fluorescence at the last frame of the image series. After a series of Gaussian blurry, thresholding, binary, and particle analysis, the size and fluorescence in all channels were extracted. The following analyses were carried out with Matlab.

Appendix H

Calibration constants and reaction rate coefficients of PEN DNA study

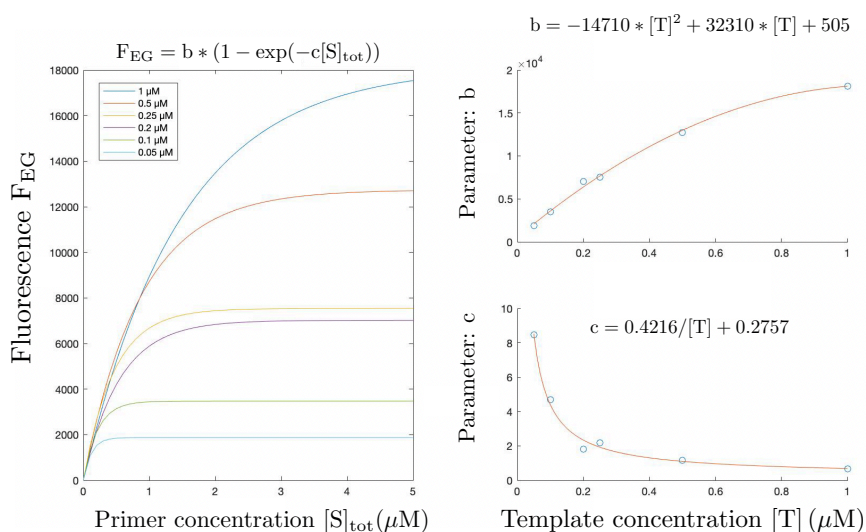


Fig. H.1: Calibration curve for bulk PEN DNA reactions. Obtaining the calibration fitting constants, which are functions of average template concentrations in the bulk system.

Here we show the calibration curve in the buffer solution (bulk) to allow conversion from the numerically obtained concentration units to the arbitrary fluorescence units of Evagreen. For the bulk system, the calibration constants depend on the template concentrations in the system and therefore have to be adjusted accordingly. The functional form of the calibration is valid in the region where $[S]_{tot} < 5[T]$.

Next, we show the calibration curve in the proteinosomes, which is independent of template concentration, given the local template concentration in the proteinosome is fixed to a certain value.

Calibration curves are obtained without the PEN enzymes in the system, which implies that while taking the total primer concentration in these studies, the $[2ST]$ species is missing. However, in the reaction assays, the $[2ST]$ species is present, but the difference in the

calibration due to this effect is negligible.

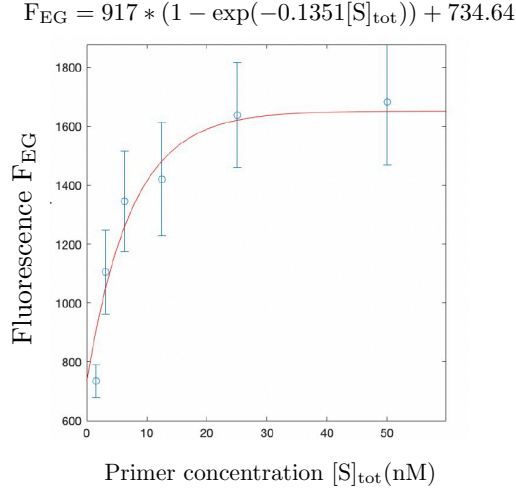


Fig. H.2: Calibration curve for PEN DNA reactions in proteinosomes. Obtaining the calibration fitting constants in the proteinosomes system.

Fitted Parameters

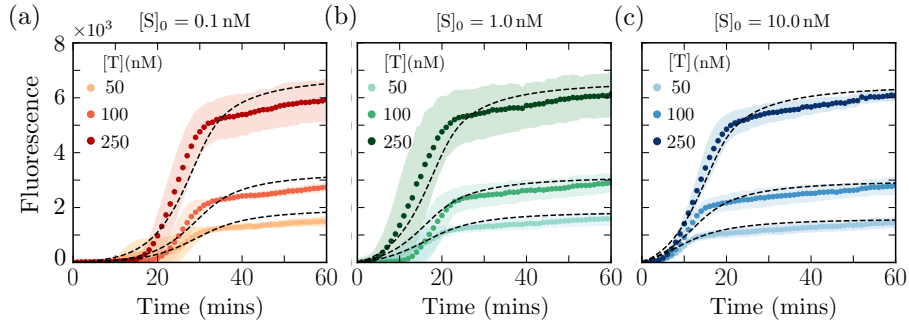


Fig. H.3: Readout of total primer kinetic profile in the presence of degradation. $[S]_{tot}$ readout in the form of fluorescence at different average template concentrations for initial primer concentrations (a) 0.1 nM, (b) 1.0 nM, and (c) 10 nM, in the presence of the exonuclease enzyme. The fluorescence does not saturate because the deactivation rate is not pronounced to induce a flat saturation. It is evident that for higher template concentrations, the maximum value reached is highest and set by the template concentration since it does not appear to vary with the initial primer concentration. Markers represent experimental data, and dashed black lines represent data from the theoretical model.

The reaction rate coefficients in the bulk system (reference), as obtained by global fitting (using the same method as in Appendix. F), are given in the table below. We also had to add a lag time to the theoretical data to account for the initial equilibration time and duration when photo-bleaching occurs in the experiments.

Symbols	Values in buffer	Values in psome
k_a	$0.028 \text{ min}^{-1} \text{ nM}^{-1}$	$0.34 \text{ min}^{-1} \text{ nM}^{-1}$
k_d	0.3 min^{-1}	0.5 min^{-1}
k_p	5.2 min^{-1}	40.2 min^{-1}
k_{pSD}	0.01 min^{-1}	0.1 min^{-1}
k_n	2.0 min^{-1}	30.45 min^{-1}
k_e	0.03 min^{-1}	–

Exonuclease	Initial primer	Lagtime values (in buffer)
No	0.1 nM	16 mins
	1.0 nM	12 mins
	10.0 nM	0 min
Yes	0.1 nM	9 mins
	1.0 nM	7 mins
	10.0 nM	0 min

The rates of autocatalysis obtained from fitting the exponential function are listed below.

System	Avg. template conc.	Rate
Buffer	50 nM	0.146 min^{-1}
	100.0 nM	0.159 min^{-1}
	250.0 nM	0.168 min^{-1}
Proteinosome	1.03 nM	0.178 min^{-1}
	0.1636 nM	0.055 min^{-1}
	0.074 nM	0.0285 min^{-1}

List of Figures

1.1	Illustrative examples of biomolecular condensates in eukaryotic cells.	2
1.2	Schematic representation of the functional repertoire of biomolecular condensates.	3
1.3	Schematic of charged sequence of polymers.	7
1.4	Onset of phase separation in Flory Huggins lattice model.	9
1.5	Phase separation in a binary mixture. Parameters: $k_B T = 1, L = 1, \nu_0 = 1, r_1 = 2, \chi_{01} = 1$ and $2.5, 2\xi/R = 0.75$	10
1.6	Phase diagrams for mean field models. Parameters: $k_B T = 1, \nu_0 = 1$ (a) $L = 1, r_1 = 2, \chi_{01} = 1$ and $2.5, 2\xi/R = 0.75$, (b) $L = 2, r_{1/2} = 1, \chi_{01} = 3, \chi_{02} = -1, \chi_{12} = 0$	12
1.7	Phase diagrams for beyond mean-field models. Parameters: Listed in the figure legends.	12
1.8	Spinodal decomposition and nucleation. Parameters: $k_B T = 1, L = 1$, grid size $N = (256 \times 256)$ $\nu_0 = 1, r_1 = 1, \chi_{01} = 2.5, m_{01} = 1, \kappa_1 = 3, dt = 0.1$, time steps = 7000 (i) $\bar{\phi}_1 = 0.5$ (ii) $\bar{\phi}_1 = 0.8$	13
1.9	Conversion between chemical species allows onset of chemical equilibrium.	14
1.10	Chemical equilibrium and conserved quantities. Parameters: $k_B T = 1, L = 2, \nu_0 = 1, r_{A/B} = 1, \psi_1 = 0.4, \omega_A = 2, \omega_B = 0$, (a) (orange) $\chi_{0A} = -1, \chi_{0B} = 3, \chi_{AB} = 0$, (dark orange) $\chi_{0A} = -1, \chi_{0B} = -3, \chi_{AB} = -2$, (yellow) $\chi_{0A} = \chi_{0B} = \chi_{AB} = 0$, (b) $k = 1$	15
1.11	Thermodynamic equilibrium. Parameters: $k_B T = 1, L = 2, \nu_0 = 1, r_{A/B} = 1, \chi_{0A} = -1, \chi_{0B} = 3, \chi_{AB} = 0, \omega_A = 2, \omega_B = 0$ (b) $\Delta\omega$ listed in figure legend	17
1.12	Phase separation tunes chemical equilibrium. Parameters: $k_B T = 1, L = 2, \nu_0 = 1, r_{A/B} = 1, \chi_{0A} = -1, \chi_{0B} = 3, \chi_{AB} = 0, \omega_A = 2, \omega_B = 0$, (b) $\Delta\omega$ listed in figure legend	18

1.13	Difference in average volume fractions due to mixing. Parameters:	
	$k_B T = 1, L = 2, \nu_0 = 1, r_{A/B} = 1, \chi_{0A} = -1, \chi_{0B} = 3, \chi_{AB} = 0, \omega_A =$	
	$2, \omega_B = 0, \Delta\omega$ listed in figure legend	18
2.1	Mass action kinetics of a unimolecular reaction at phase equilibrium. Parameters: $k_B T = 1, L = 2, \nu_0 = 1, r_{A/B} = 1, \chi_{0A} = -1, \chi_{0B} =$	
	$3, \chi_{AB} = 0, \omega_A = 2, \omega_B = 0, \psi_1 = 0.55, k^{I/II} = 1$, Initial cond. 1 : $(\bar{\phi}_B(0), \bar{\phi}_A(0)) =$	
	$(0.15, 0.4)$, Initial cond. 2 : $(\bar{\phi}_B(0), \bar{\phi}_A(0)) = (0.5, 0.05)$	25
2.2	Effects of dissimilar reaction rate coefficients between phases - I. Parameters: $k_B T = 1, L = 2, \nu_0 = 1, r_{A/B} = 1, \chi_{0A} = -1, \chi_{0B} =$	
	$3, \chi_{AB} = 0, \omega_A = 2, \omega_B = 0, \psi_1 = 0.55$, Initial cond. 1 : $(\bar{\phi}_B(0), \bar{\phi}_A(0)) =$	
	$(0.15, 0.4)$, varying rate coefficient k^I and keeping $k^{II} = 1$ fixed	26
2.3	Effects of dissimilar reaction rate coefficients between phases - II.	
	Parameters: Same as above	26
2.4	Mass action kinetics of a bimolecular reaction at phase equilibrium. Parameters: $k_B T = 1, L = 3, \nu_0 = 1, r_{A/B} = 1, r_C = 2, \chi_{0A} =$	
	$1.25, \chi_{0B} = 0, \chi_{0C} = 3.2, \chi_{AB} = 0, \chi_{AC} = -1.25, \chi_{BC} = 0, \omega_A = 3.5, \omega_B =$	
	$3.5, \omega_C = 0, \psi_1 = 0.42, \psi_2 = 0.05$ (blue), 0.1 (red), $k^{I/II} = 1$	27
2.5	Unimolecular chemical reaction maintained away from chemical equilibrium. Parameters: $k_B T = 1, L = 2, \nu_0 = 1, r_{A/B} = 1, \chi_{0A} =$	
	$-1, \chi_{0B} = 3, \chi_{AB} = 0, \omega_A = 2, \omega_B = 0, \psi_1 = 0.55, k^{I/II} = 1$,	
	external energy in mixed phase $\tilde{\mu}^-(\phi_B) = 0.5 \tilde{\mu}^{-,I} \left(\tanh\left(\frac{\phi_B - 0.3}{0.05}\right) \right)$	29
2.6	Measure of non-equilibrium free energy. Parameters: Same as above .	30
2.7	Selection of tie line for varying conserved quantity. Parameters:	
	Same as above	31
2.8	Measure of non-equilibrium free energy. Parameters: Same as above .	32
3.1	Schematic representation of a system with dilute reactive clients in presence of a drop.	34
3.2	Partition coefficient of clients: Dilute limit. Parameters: $k_B T =$	
	$1, \nu_0 = 1, r_1 = 1, \chi_{01} = 3, \chi_{02} = -1, \chi_{12} = 0, \phi_1^{0,I} = 0.929, \phi_1^{0,II} =$	
	$0.071, \bar{\phi}_1 = 0.4, P_2 = 0.4237$ (light green), $P_2 = 0.00018677$ (mid green), $P_2 =$	
	$5.166e - 38$ (dark green)	35
3.3	Scaffold equilibrium volume fraction: Dilute limit. Parameters:	
	$k_B T = 1, \nu_0 = 1, r_{1/2} = 1, \chi_{01} = 3, \chi_{02} = -1, \chi_{12} = 0, \phi_1^{0,I} = 0.929, \phi_1^{0,II} =$	
	$0.071, \bar{\phi}_1 = 0.4$	37

- 3.4 **Stationary profile for scaffold in spherical geometry.** Parameters: $k_B T = 1, \nu_0 = 1, r_1 = 1, \chi_{01} = 3, \kappa_1 = 1.5 \times 10^{-3}, m_{01} = 1, \bar{\phi}_1 = 0.5$ 38
- 3.5 **Schematic representation of the model geometry.** Parameters: $k_B T = 1, \nu_0 = 1, r_1 = 1, \chi_{01} = 3, \kappa_1 = 1.5 \times 10^{-3}, m_{01} = 1, \bar{\phi}_1 = 0.11$ 40
- 3.6 **Spatio-temporal and steady state profiles of the clients.** Parameters: $k_B T = 1, \nu_0 = 1, r_{1/A/B} = 1, \chi_{01} = 3, V^I/V = 0.008, \psi_1 = 0.0005, \chi_{0A_1} = 2.5, \chi_{0B} = 2, \omega_{A_1} = -4, \omega_B = 0, P_{A_1} = 500, P_B = 2, \bar{\phi}_B(t_0) = 10^{-4}\psi_1, k^I = 1, k^{II} = 0.01, dt = 10^{-6}, dr = 10^{-3}, \tilde{D}_{A_1}^I = 0.003, \tilde{D}_B^I = \tilde{D}_{A_1}^I/3, \tilde{D}_{A_1}^{II} = 10\tilde{D}_{A_1}^I, \tilde{D}_B^{II} = \tilde{D}_{A_1}^{II}/3$ for (a) $\tilde{\mu}^I/k_B T = 5, t_\infty = 100$ 43
- 3.7 **Relative yield is most significant in the presence of fuel and at infinite diffusivity.** Parameters: Common parameters same as above except (a) $\tilde{D}_{A_1}^I = 0.03, \tilde{D}_B^I = \tilde{D}_{A_1}^I/3, \tilde{D}_{A_1}^{II} = 10\tilde{D}_{A_1}^I, \tilde{D}_B^{II} = \tilde{D}_{A_1}^{II}/3$ and (b) $\tilde{D}_{A_1}^I = 0.003$ (light blue) = 0.008 (mid blue) = 0.03 (dark blue) the other diffusivities set as similar factors as in (a), for $\tilde{\mu}^I/k_B T = 5$ 44
- 3.8 **Relative yield optimality for varying parameters.** Parameters: Same as above at infinite diffusivity for $\tilde{\mu}_F^I/k_B T = 5, P_B = 5$ 45
- 3.9 **Relative yield optimality is most significant in the presence of fuel and high diffusivities.** Parameters: $k_B T = 1, \nu_0 = 1, r_{1/A_1/A_2} = 1, r_B = 2, \chi_{01} = 3, \psi_1 = 0.0001, \psi_2 = 0.2\psi_1, \chi_{0A_1} = 2.5, \chi_{0A_2} = 2, \chi_{0B} = 0, \omega_{A_1/A_2} = -3.5, \omega_B = 1, P_{A_1/A_2} = 10, P_B = 200, \bar{\phi}_B(t_0) = 10^{-2}\psi_1, k^I = 1, k^{II} = 0.01, dt = 10^{-6}, dr = 10^{-3}, \tilde{D}_{A_1/A_2/B}^I = 0.01, \tilde{D}_{A_1/A_2/B}^{II} = 10\tilde{D}_{A_1/A_2/B}^I, t_\infty = 100$ for (b) $\tilde{\mu}^I/k_B T = 5$. The reaction and diffusion coefficients are scaled by ψ_1 46
- 3.10 **Relative yield optimality for varying parameters.** Parameters: Same as above for infinite diffusivities for $\tilde{\mu}_F^I/k_B T = 5, P_{A_1/A_2} = 10$ 47
- 3.11 **Temporal traces for monomers with varying nucleation number.** Parameters: $k_B T = 1, \nu_0 = 1, r_{1/A} = 1, r_{A_n} = n, \chi_{01} = 3, V^I/V = 0.008, \psi_1 = 0.0001, \chi_{0A} = 2.5, \chi_{0A_2} = 2, \chi_{0A_3} = 2, \omega_A = 5.5, \omega_{A_2} = -7, \omega_{A_3} = -5, P_{A/A_2/A_3} = 10, \bar{\phi}_{A_2/A_3}(t_0) = 10^{-2}\psi_1, k^I = 1, k^{II} = 0.01$, at infinite diffusivities 48

3.12	Nucleation number, fuel, and diffusivity affect the relative initial rate. Parameters: Same as above (b) for finite diffusivity, $V^I/V = 0.008$, $\tilde{\mu}_F^I/k_B T = 5$, $\tilde{D}_A^I = 0.003$, $\tilde{D}_{A_2}^I = \tilde{D}_A^I/2$, $\tilde{D}_{A_3}^I = \tilde{D}_A^I/3$, $\tilde{D}_{A/A_2/A_3}^{II} = 10\tilde{D}_{A/A_2/A_3}^I$, $dt = 10^{-6}$, $dr = 10^{-3}$,	48
3.13	Relative yield optimality for varying parameters. Parameters: Same as for infinite diffusivities with $P_{A_2} = 10$	49
4.1	The design of chemically fueled reaction cycles.	51
4.2	Individual reaction properties. Parameters: Fig. F.8 in Appendix. F	52
4.3	Competition between reaction cycles for a shared fuel - I. Parameters: Fig. F.8 in Appendix. F	53
4.4	Competition between reaction cycles for a shared fuel - II. Parameters: Fig. F.8 in Appendix. F	54
4.5	Ternary phase diagram.	58
4.6	Mechanism of co-phase separation and increased lifetime. Parameters: Fig. F.8 in Appendix. F	58
4.7	Total droplet volume increases, and total hydrolysis rate decreases in the dilute phase allowing longer survival of the parasite. Parameters: Fig. F.8 in Appendix. F	59
4.8	Reduction in the composition of the product (parasite) in the droplets with increasing product of competitor 2 (host) concentration. Parameters: Fig. F.8 in Appendix. F	60
4.9	Schematic representation of co-phase separation facilitating the survival of the product in repetitive fueling starvation experiments.	61
4.10	Co-phase separation allows survival of parasite during periodic fueling. Parameters: Fig. F.8 in Appendix. F	61
4.11	Theoretical long-time behavior at periodic fueling. Parameters: Fig. F.8 in Appendix. F	62
4.12	The buffer capacity against fuel oscillations increases for the parasite with increasing host concentration. Parameters: Fig. F.8 in Appendix. F	62
4.13	(Co) Phase separation allows buffering of concentration. Parameters: Fig. F.8 in Appendix. F	63

4.14	Host and parasite identity depend on the solubilities of the components and initial precursor concentrations. Parameters: Fig. F.8 in Appendix. F	64
5.1	Kinetic autocatalytic profiles. Parameters: $k = 1, dt = 0.01, B_0 = 10^{-4}, \psi_1 = 1$	66
5.2	Schematic representation of the autocatalytic PEN DNA reaction and encapsulation in proteinosomes.	67
5.3	Readout of total primer kinetic profile in the absence of degradation.	68
5.4	Characterisation of PEN DNA reaction in proteinosome.	69
5.5	Compartmentalization affects the rate of autocatalysis.	70
F.1	First order deactivation and short lifetime of the product of competitor 1.	90
F.2	First order deactivation and short lifetime of the product.	91
F.3	Zeroth order deactivation and long lifetime of the product of competitor 2.	91
F.4	First order deactivation for the product and product of competitor 1.	92
F.5	Competitor 1 reduces the yield and lifetime of the product.	92
F.6	Non-linear and linear deactivation for the product and product of competitor 2 respectively.	93
F.7	Competitor 2 reduces the yield but increases the lifetime of the product.	93
F.8	Reaction rate coefficients.	94
F.9	Dilute phase concentrations.	94
F.10	Poissonian fuelling in individual reaction cycles.	94
H.1	Calibration curve for bulk PEN DNA reactions.	98
H.2	Calibration curve for PEN DNA reactions in proteinosomes.	99
H.3	Readout of total primer kinetic profile in the presence of degradation.	99

References

- [1] W. B. Hardy. On the structure of cell protoplasm: Part i. the structure produced in a cell by fixative and post-mortem change. the structure of colloidal matter and the mechanism of setting and of coagulation. *The Journal of Physiology*, 24(2):158–240.1, 1899.
- [2] Edmund B. Wilson. The structure of protoplasm. *Science*, 10(237):33–45, 1899.
- [3] Stephane Leduc. *The mechanism of life*. Rebman, New York, 1911.
- [4] Maurice L. Huggins. Some properties of solutions of long-chain compounds. *The Journal of Physical Chemistry*, 46(1):151–158, Jan 1942.
- [5] Paul J. Flory. Thermodynamics of high polymer solutions. *The Journal of Chemical Physics*, 10(1):51–61, 1942.
- [6] Paul J. Flory. *Principles of Polymer Chemistry*. Cornell University Press, New York, NY, unabridged, corrected republication edition, 1953.
- [7] Pierre-Gilles de Gennes. Ultradivided matter. *Nature*, 412(6845):385, July 2001.
- [8] H.M. Farrell. Models for casein micelle formation. *Journal of Dairy Science*, 56(9):1195–1206, 1973.
- [9] J A Thomson, P Schurtenberger, G M Thurston, and G B Benedek. Binary liquid phase separation and critical phenomena in a protein/water solution. *Proc Natl Acad Sci U S A*, 84(20):7079–7083, October 1987.
- [10] A. M. Donald, A. H. Windle, and Helmut R. Brand. Liquid Crystalline Polymers. *Physics Today*, 46(11):87, January 1993.
- [11] Stephanie Spannll, Maria Tereshchenko, Giovanni J. Mastromarco, Sean J. Ihn, and Hyun O. Lee. Biomolecular condensates in neurodegeneration and cancer. *Traffic*, 20(12):890–911, 2019.
- [12] Anthony A. Hyman and Kai Simons. Beyond oil and water phase transitions in cells. *Science*, 337(6098):1047–1049, 2012.
- [13] Clifford P. Brangwynne, Christian R. Eckmann, David S. Courson, Agata Rybarska, Carsten Hoege, Jöbin Gharakhani, Frank Jülicher, and Anthony A. Hyman. Germline p granules are liquid droplets that localize by controlled dissolution/condensation. *Science*, 324(5935):1729–1732, 2009.
- [14] Timothy J Nott, Evangelia Petsalaki, Patrick Farber, Dylan Jervis, Eden Fussner, Anne Plochowitz, Timothy D Craggs, David P Bazett-Jones, Tony Pawson, Julie D Forman-Kay, and Andrew J Baldwin. Phase transition of a disordered nuage protein generates environmentally responsive membraneless organelles. *Mol Cell*, 57(5):936–947, March 2015.
- [15] Adam G Larson, Daniel Elnatan, Madeline M Keenen, Michael J Trnka, Jonathan B

- Johnston, Alma L Burlingame, David A Agard, Sy Redding, and Geeta J Narlikar. Liquid droplet formation by HP1 α suggests a role for phase separation in heterochromatin. *Nature*, 547(7662):236–240, June 2017.
- [16] Pulong Li, Sudeep Banjade, Hui-Chun Cheng, Soyeon Kim, Baoyu Chen, Liang Guo, Marc Llaguno, Javoris V Hollingsworth, David S King, Salman F Banani, Paul S Russo, Qiu-Xing Jiang, B Tracy Nixon, and Michael K Rosen. Phase transitions in the assembly of multivalent signalling proteins. *Nature*, 483(7389):336–340, March 2012.
- [17] Marina Feric, Nilesh Vaidya, Tyler S Harmon, Diana M Mitrea, Lian Zhu, Tiffany M Richardson, Richard W Kriwacki, Rohit V Pappu, and Clifford P Brangwynne. Co-existing liquid phases underlie nucleolar subcompartments. *Cell*, 165(7):1686–1697, May 2016.
- [18] Shana Elbaum-Garfinkle, Younghoon Kim, Krzysztof Szczepaniak, Carlos Chih-Hsiung Chen, Christian R Eckmann, Sua Myong, and Clifford P Brangwynne. The disordered P granule protein LAF-1 drives phase separation into droplets with tunable viscosity and dynamics. *Proc Natl Acad Sci U S A*, 112(23):7189–7194, May 2015.
- [19] Salman F Banani, Hyun O Lee, Anthony A Hyman, and Michael K Rosen. Biomolecular condensates: organizers of cellular biochemistry. *Nat Rev Mol Cell Biol*, 18(5):285–298, February 2017.
- [20] Saumya Jain, Joshua R. Wheeler, Robert W. Walters, Anurag Agrawal, Anthony Barsic, and Roy Parker. Atpase-modulated stress granules contain a diverse proteome and substructure. *Cell*, 164(3):487–498, 2016.
- [21] Ji-Young Youn, Wade H. Dunham, Seo Jung Hong, James D.R. Knight, Mikhail Bashkurov, Ginny I. Chen, Halil Bagci, Bhavisha Rathod, Graham MacLeod, Simon W.M. Eng, Stephane Angers, Quaid Morris, Marc Fabian, Jean-Francois Cote, and Anne-Claude Gingras. High-density proximity mapping reveals the subcellular organization of mrna-associated granules and bodies. *Molecular Cell*, 69(3):517–532.e11, 2018.
- [22] Xiaolei Su, Jonathon A. Ditlev, Enfu Hui, Wenmin Xing, Sudeep Banjade, Julia Okrut, David S. King, Jack Taunton, Michael K. Rosen, and Ronald D. Vale. Phase separation of signaling molecules promotes t cell receptor signal transduction. *Science*, 352(6285):595–599, 2016.
- [23] Lindsay B. Case, Xu Zhang, Jonathon A. Ditlev, and Michael K. Rosen. Stoichiometry controls activity of phase-separated clusters of actin signaling proteins. *Science*, 363(6431):1093–1097, 2019.
- [24] Jeffrey B. Woodruff, Beatriz Ferreira Gomes, Per O. Widlund, Julia Mahamid, Alf Honigsmann, and Anthony A. Hyman. The centrosome is a selective condensate that nucleates microtubules by concentrating tubulin. *Cell*, 169(6):1066–1077.e10, 2017.
- [25] Benjamin R. Sabari, Alessandra Dall’Agnese, Ann Boija, Isaac A. Klein, Eliot L. Coffey, Krishna Shrinivas, Brian J. Abraham, Nancy M. Hannett, Alicia V. Zamudio, John C. Manteiga, Charles H. Li, Yang E. Guo, Daniel S. Day, Jurian Schuijers,

- Eliza Vasile, Sohail Malik, Denes Hnisz, Tong Ihn Lee, Ibrahim I. Cisse, Robert G. Roeder, Phillip A. Sharp, Arup K. Chakraborty, and Richard A. Young. Coactivator condensation at super-enhancers links phase separation and gene control. *Science*, 361(6400), 2018.
- [26] Titus M. Franzmann, Marcus Jahnel, Andrei Pozniakovsky, Julia Mahamid, Alex S. Holehouse, Elisabeth Nüske, Doris Richter, Wolfgang Baumeister, Stephan W. Grill, Rohit V. Pappu, Anthony A. Hyman, and Simon Alberti. Phase separation of a yeast prion protein promotes cellular fitness. *Science*, 359(6371), 2018.
- [27] Tae Hun Kim, Brian Tsang, Robert M. Vernon, Nahum Sonenberg, Lewis E. Kay, and Julie D. Forman-Kay. Phospho-dependent phase separation of fmrp and caprin1 recapitulates regulation of translation and deadenylation. *Science*, 365(6455):825–829, 2019.
- [28] Elvan Boke, Martine Ruer, Martin Wühr, Margaret Coughlin, Regis Lemaitre, Steven P. Gygi, Simon Alberti, David Drechsel, Anthony A. Hyman, and Timothy J. Mitchison. Amyloid-like self-assembly of a cellular compartment. *Cell*, 166(3):637–650, 2016.
- [29] Menglong Zeng, Yuan Shang, Yoichi Araki, Tingfeng Guo, Richard L. Haganir, and Mingjie Zhang. Phase transition in postsynaptic densities underlies formation of synaptic complexes and synaptic plasticity. *Cell*, 166(5):1163–1175.e12, 2016.
- [30] Martina Ugrinic, Adrian Zambrano, Simon Berger, Stephen Mann, T.-Y. Dora Tang, and Andrew deMello. Microfluidic formation of proteinosomes. *Chem. Commun.*, 54:287–290, 2018.
- [31] Xiaoliang Wang, Xiaoman Liu, and Xin Huang. Bioinspired protein-based assembling: Toward advanced life-like behaviors. *Advanced Materials*, 32(25):2001436, 2020.
- [32] Junbo Li, Zhijun Xu, Mei Zhu, Chunyu Zhao, Xiaoliang Wang, Haixu Chen, Xiaoman Liu, Lei Wang, and Xin Huang. Programmable spatial organization of liquid-phase condensations. *Chem*, 8(3):784–800, 2022.
- [33] Shogo Koga, David S. Williams, Adam W. Perriman, and Stephen Mann. Peptide–nucleotide microdroplets as a step towards a membrane-free protocell model. *Nature Chemistry*, 3(9):720–724, Sep 2011.
- [34] William M. Aumiller and Christine D. Keating. Phosphorylation-mediated rna/peptide complex coacervation as a model for intracellular liquid organelles. *Nature Chemistry*, 8(2):129–137, Feb 2016.
- [35] Andrea Testa, Mirco Dindo, Aleksander A. Rebane, Babak Nasouri, Robert W. Style, Ramin Golestanian, Eric R. Dufresne, and Paola Laurino. Sustained enzymatic activity and flow in crowded protein droplets. *Nature Communications*, 12(1):6293, Nov 2021.
- [36] Charles D. Crowe and Christine D. Keating. Liquid-liquid phase separation in artificial cells. *Interface Focus*, 8(5):20180032, 2018.
- [37] Samuel A. Safran. *Statistical thermodynamics of surfaces, interfaces, and membranes*. Addison-Wesley Pub., 1994.
- [38] Frederick Reif. *Fundamentals of statistical and thermal physics*. McGraw-Hill, New

- York, 1965.
- [39] Herbert B Callen. *Thermodynamics and an Introduction to Thermostatistics*. John Wiley and Sons, 1991.
- [40] L D Landau and E.M. Lifshitz. *Statistical Physics: Volume 5*. Butterworth-Heinemann, 1980.
- [41] Peter W. Atkins and Julio de Paula. *Physical Chemistry*. W.H.Freeman and Co., 2006.
- [42] John W. Cahn and John E. Hilliard. Free energy of a nonuniform system. i. interfacial free energy. *The Journal of Chemical Physics*, 28(2):258–267, 1958.
- [43] Clifford P. Brangwynne, Peter Tompa, and Rohit V. Pappu. Polymer physics of intracellular phase transitions. *Nature Physics*, 11(11):899–904, Nov 2015.
- [44] Jie Wang, Jeong-Mo Choi, Alex S. Holehouse, Hyun O. Lee, Xiaojie Zhang, Marcus Jahnel, Shovamayee Maharana, Regis Lemaitre, Andrei Pozniakovsky, David Drechsel, Ina Poser, Rohit V. Pappu, Simon Alberti, and Anthony A. Hyman. A molecular grammar governing the driving forces for phase separation of prion-like rna binding proteins. *Cell*, 174:688–699.e16, 2018.
- [45] Chi W. Pak, Martyna Kosno, Alex S. Holehouse, Shae B. Padrick, Anuradha Mittal, Rustam Ali, Ali A. Yunus, David R. Liu, Rohit V. Pappu, and Michael K. Rosen. Sequence determinants of intracellular phase separation by complex coacervation of a disordered protein. *Molecular Cell*, 63:72–85, 2016.
- [46] Omar Adame Arana, Christoph A. Weber, Vasily Zaburdaev, Jacques Prost, and Frank Jülicher. Liquid phase separation controlled by ph. *Biophysical Journal*, 119:1590–1605, 2020.
- [47] Anatol W. Fritsch, Andres F. Diaz-Delgadillo, Omar Adame Arana, Carsten Hoege, Matthäus Mittasch, Moritz Kreysing, Mark Leaver, Anthony A. Hyman, Frank Jülicher, and Christoph A. Weber. Local thermodynamics govern formation and dissolution of *Caenorhabditis elegans* p granule condensates. *Proceedings of the National Academy of Sciences*, 118(37):e2102772118, 2021.
- [48] Masao Doi and S. F. Edwards. *The Theory of Polymer Dynamics*. Clarendon Press, 1988.
- [49] Yi-Hsuan Lin, Julie D. Forman-Kay, and Hue Sun Chan. Sequence-specific polyampholyte phase separation in membraneless organelles. *Phys. Rev. Lett.*, 117:178101, Oct 2016.
- [50] Yi-Hsuan Lin, Jianhui Song, Julie D. Forman-Kay, and Hue Sun Chan. Random-phase-approximation theory for sequence-dependent, biologically functional liquid-liquid phase separation of intrinsically disordered proteins. *Journal of Molecular Liquids*, 228:176–193, 2017. From simple liquids to macromolecular solutions: recent experimental and theoretical developments. In Honor of the 70th birthday of Vojko Vlachy.
- [51] Robert A. Alberty. *Thermodynamics of Biochemical Reactions*. Wiley-Interscience, Hoboken, N.J., 2003.
- [52] Jean-Louis Burgot. *The Notion of Activity in Chemistry*. Springer International

- Publishing, 2017.
- [53] Peter Atkins and Laretta Jones. *Chemical Principles: The Quest for Insight*. W.H. Freeman, 2009.
 - [54] Gerold Adam, Peter Lauger, and Gunther Stark. *Physikalische Chemie und Biophysik*. Springer-Verlag Berlin Heidelberg, 2009.
 - [55] Gilbert Newton Lewis. Outlines of a new system of thermodynamic chemistry. *Proceedings of the American Academy of Arts and Sciences*, 43(7):259–293, 1907.
 - [56] Jonathan Bauermann, Sudarshana Laha, Patrick M. McCall, Frank Julichner, and Christoph A. Weber. Chemical Kinetics and Mass Action in Coexisting Phases. *The Journal of American Chemical Society*, 2021.
 - [57] Christoph A Weber, David Zwicker, Frank Julichner, and Chiu Fan Lee. Physics of active emulsions. *Reports on Progress in Physics*, 82(6):064601, apr 2019.
 - [58] Josiah Willard Gibbs. On the Equilibrium of Heterogeneous Substances. *Transactions of the Connecticut Academy of Arts and Sciences*, 3:300–320, 1879.
 - [59] P. G. de Gennes. Wetting: statics and dynamics. *Rev. Mod. Phys.*, 57:827–863, Jul 1985.
 - [60] Patrick S. Schwarz, Sudarshana Laha, Jacqueline Janssen, Tabea Huss, Job Boekhoven, and Christoph A. Weber. Parasitic behavior in competing chemically fueled reaction cycles. *Chem. Sci.*, 12:7554–7560, 2021.
 - [61] Stefano Bo, Lars Hubatsch, Jonathan Bauermann, Christoph A. Weber, and Frank Julichner. Stochastic dynamics of single molecules across phase boundaries. *Phys. Rev. Research*, 3:043150, Dec 2021.
 - [62] Bernhard Palsson. *Systems Biology: Properties of Reconstructed Networks*. Cambridge University Press, Cambridge ; New York, 2006.
 - [63] Jonathan Bauermann, Christoph A. Weber, and Frank Julichner. Energy and matter supply for active droplets. *Annalen der Physik*, 534(9):2200132, 2022.
 - [64] Christopher A. Strulson, Rosalynn C. Molden, Christine D. Keating, and Philip C. Bevilacqua. Rna catalysis through compartmentalization. *Nature Chemistry*, 4(11):941–946, Nov 2012.
 - [65] Karina K. Nakashima, Jochem F. Baaij, and Evan Spruijt. Reversible generation of coacervate droplets in an enzymatic network. *Soft Matter*, 14:361–367, 2018.
 - [66] Bjorn Drobot, Juan M. Iglesias-Artola, Kristian Le Vay, Viktoria Mayr, Mrityunjy Kar, Moritz Kreysing, Hannes Mutschler, and T-Y Dora Tang. Compartmentalised rna catalysis in membrane-free coacervate protocells. *Nature Communications*, 9(1):3643, Sep 2018.
 - [67] Arren Bar-Even, Elad Noor, Yonatan Savir, Wolfram Liebermeister, Dan Davidi, Dan S. Tawfik, and Ron Milo. The moderately efficient enzyme: Evolutionary and physicochemical trends shaping enzyme parameters. *Biochemistry*, 50(21):4402–4410, May 2011.
 - [68] Ron Milo and Rob Philips. *Cell biology by the numbers*. CRC Press, 2015.
 - [69] K. Denbigh. *The Principles of Chemical Equilibrium*. Cambridge University Press, Cambridge, 1961.

- [70] Terrell L. Hill. *Free Energy Transduction and Biochemical Cycle Kinetics*. Springer-Verlag, New York, 1989.
- [71] Daniel A. Beard, Shou dan Liang, and Hong Qian. Energy balance for analysis of complex metabolic networks. *Biophysical Journal*, 83(1):79–86, 2002.
- [72] Taisuke Kojima and Shuichi Takayama. Membraneless compartmentalization facilitates enzymatic cascade reactions and reduces substrate inhibition. *ACS Applied Materials and Interfaces*, 10(38):32782–32791, Sep 2018.
- [73] Wylie Stroberg and Santiago Schnell. Do cellular condensates accelerate biochemical reactions? lessons from microdroplet chemistry. *Biophysical Journal*, 115(1):3–8, 2018.
- [74] Denis L. J. Lafontaine, Joshua A. Riback, Rümeyza Bascetin, and Clifford P. Brangwynne. The nucleolus as a multiphase liquid condensate. *Nature Reviews Molecular Cell Biology*, 22(3):165–182, Mar 2021.
- [75] Yu Chen and Andrew S Belmont. Genome organization around nuclear speckles. *Current Opinion in Genetics and Development*, 55:91–99, 2019. Genome Architecture and Expression.
- [76] Shuyan Liu, Taishu Wang, Yulin Shi, Lu Bai, Shanshan Wang, Dong Guo, Yang Zhang, Yangfan Qi, Chaoqun Chen, Jinrui Zhang, Yingqiu Zhang, Quentin Liu, Qingkai Yang, Yang Wang, and Han Liu. Usp42 drives nuclear speckle mrna splicing via directing dynamic phase separation to promote tumorigenesis. *Cell Death and Differentiation*, 28(8):2482–2498, Aug 2021.
- [77] William Peeples and Michael K. Rosen. Mechanistic dissection of increased enzymatic rate in a phase-separated compartment. *Nature Chemical Biology*, 17(6):693–702, Jun 2021.
- [78] Marta Tena-Solsona, Benedikt Rieß, Raphael K. Grötsch, Franziska C. Löhner, Caren Wanzke, Benjamin Käsdorf, Andreas R. Bausch, Peter Müller-Buschbaum, Oliver Lieleg, and Job Boekhoven. Non-equilibrium dissipative supramolecular materials with a tunable lifetime. *Nature Communications*, 8(1):15895, Jul 2017.
- [79] Brigitte A. K. Kriebisch, Alexander Jussupow, Alexander M. Bergmann, Fabian Kohler, Hendrik Dietz, Ville R. I. Kaila, and Job Boekhoven. Reciprocal coupling in chemically fueled assembly: A reaction cycle regulates self-assembly and vice versa. *Journal of the American Chemical Society*, 142(49):20837–20844, Dec 2020.
- [80] Krishnendu Jalani, Anjali Devi Das, Ranjan Sasmal, Sarit S. Agasti, and Subi J. George. Transient dormant monomer states for supramolecular polymers with low dispersity. *Nature Communications*, 11(1):3967, Aug 2020.
- [81] Esra te Brinke, Joost Groen, Andreas Herrmann, Hans A. Heus, Germán Rivas, Evan Spruijt, and Wilhelm T. S. Huck. Dissipative adaptation in driven self-assembly leading to self-dividing fibrils. *Nature Nanotechnology*, 13(9):849–855, Sep 2018.
- [82] Caren Wanzke, Alexander Jussupow, Fabian Kohler, Hendrik Dietz, Ville R. I. Kaila, and Job Boekhoven. Dynamic vesicles formed by dissipative self-assembly. *ChemSystemsChem*, 2(1):e1900044, 2020.
- [83] David Zwicker, Rabea Seyboldt, Christoph A. Weber, Anthony A. Hyman, and Frank

- Jülicher. Growth and division of active droplets provides a model for protocells. *Nature Physics*, 13(4):408–413, Apr 2017.
- [84] Marvin C McMaster. *HPLC: A Practical User's Guide*. John Wiley and Sons, Inc., 2006.
- [85] A. Klosin, F. Oltsch, T. Harmon, A. Honigmann, F. Jülicher, A. A. Hyman, and C. Zechner. Phase separation provides a mechanism to reduce noise in cells. *Science*, 367(6476):464–468, 2020.
- [86] Victoria E. Deneke and Stefano Di Talia. Chemical waves in cell and developmental biology. *Journal of Cell Biology*, 217(4):1193–1204, Jan 2018.
- [87] Kevin Montagne, Raphael Plasson, Yasuyuki Sakai, Teruo Fujii, and Yannick Rondelez. Programming an in vitro dna oscillator using a molecular networking strategy. *Molecular Systems Biology*, 7(1):466, 2011.
- [88] Adrien Padirac, Teruo Fujii, and Yannick Rondelez. Bottom-up construction of in vitro switchable memories. *Proceedings of the National Academy of Sciences*, 109(47):E3212–E3220, 2012.
- [89] Alexandre Baccouche, Kevin Montagne, Adrien Padirac, Teruo Fujii, and Yannick Rondelez. Dynamic dna-toolbox reaction circuits: A walkthrough. *Methods*, 67(2):234–249, 2014. Nucleic Acids Nanotechnology.
- [90] Adrian Zambrano, Giorgio Fracasso, Mengfei Gao, Martina Ugrinic, Dishu Wang, Dietmar Appelhans, Andrew deMello, and T-Y. Dora Tang. Programmable synthetic cell networks regulated by tuneable reaction rates. *Nature Communications*, 13(1):3885, Jul 2022.
- [91] Raphaël Plasson, Axel Brandenburg, Ludovic Jullien, and Hugues Bersini. Autocatalyses. *The Journal of Physical Chemistry A*, 115(28):8073–8085, Jul 2011.
- [92] Hue Sun Chan and Ken A. Dill. Solvation: How to obtain microscopic energies from partitioning and solvation experiments. *Annual Review of Biophysics and Biomolecular Structure*, 26(1):425–459, 1997. PMID: 9241426.
- [93] S.M. Cox and P.C. Matthews. Exponential time differencing for stiff systems. *Journal of Computational Physics*, 176(2):430–455, 2002.
- [94] Anders Logg, Kent-Andre Mardal, and Garth Wells. *Automated Solution of Differential Equations by the Finite Element Method*. Springer Berlin, Heidelberg, 2012.
- [95] Ashlee N. Ford Versypt and Richard D. Braatz. Analysis of finite difference discretization schemes for diffusion in spheres with variable diffusivity. *Computers and Chemical Engineering*, 71:241–252, 2014.

Versicherung

Hiermit versichere ich, Sudarshana Laha, dass ich die vorliegende Arbeit ohne unzulässige Hilfe Dritter und ohne Benutzung anderer als der angegebenen Hilfsmittel angefertigt habe. Die aus fremden Quellen direkt oder indirekt übernommenen Gedanken sind als solche kenntlich gemacht. Die Arbeit wurde bisher weder im Inland noch im Ausland in gleicher oder ähnlicher Form einer anderen Prüfungsbehörde vorgelegt. Die Arbeit wurde in Dresden am Max-Planck-Institut für Physik komplexer Systeme unter der Betreuung von Prof. Dr. Christoph A. Weber und Prof. Dr. Frank Jülicher angefertigt.

Sudarshana Laha

Dresden, April 2023